Central Washington University

ScholarWorks@CWU

Spring 2012

Documenting the Origin of Compositional Diversity of Subduction Zone Magmatism, Alicudi, Aeolian Arc (Southern Tyrrhenian Sea, Italy) Using in situ Plagioclase Data

Rachel Hunt
Central Washington University

Follow this and additional works at: https://digitalcommons.cwu.edu/etd

Part of the Geology Commons, Geomorphology Commons, Mineral Physics Commons, and the Volcanology Commons

DOCUMENTING THE ORIGIN OF COMPOSITIONAL DIVERSITY OF

SUBDUCTION ZONE MAGMATISM, ALICUDI, AEOLIAN

ARC (SOUTHERN TYRRHENIAN SEA, ITALY)

USING IN SITU PLAGIOCLASE DATA

_____

A Thesis

Presented to

The Graduate Faculty

Central Washington University

_____

In Partial Fulfillment

of the Requirements for the Degree

Master of Science

Geology

_____

by

Rachel Hunt

May 2012

CENTRAL WASHINGTON UNIVERSITY

Graduate Studies

We hereby approve the thesis of

Rachel Hunt

Candidate for the degree of Master of Science

APPROVED FOR THE GRADUATE FACULTY

_____   _____
                            Dr. Wendy Bohrson, Committee Chair

_____   _____
                            Dr. Chris Mattinson

_____   _____
                            Dr. John Wolff

_____   _____
                            Dean of Graduate Studies

ABSTRACT

DOCUMENTING THE ORIGIN OF COMPOSITIONAL DIVERSITY OF

SUBDUCTION ZONE MAGMATISM, ALICUDI, AEOLIAN

ARC (SOUTHERN TYRRHENIAN SEA, ITALY)

USING IN SITU PLAGIOCLASE DATA

by

Rachel Hunt

May 2012

Processes that generate magma compositional diversity are important to document because composition affects degree of explosivity, which impacts hazard mitigation. Magnesium to silicon rich magmas are produced by processes such as magma recharge, assimilation, and fractional crystallization (RAFC) that occur in subvolcanic magma chamber(s). This study evaluates how magma chamber processes contribute to compositional diversity at Alicudi Volcano, Italy. Analytical and petrographic data from ten samples that span the subaerial history include whole rock major and trace elements and strontium/neodymium isotopes, and plagioclase textural types, major and trace elements, and strontium isotopes; numerical modeling was also conducted. Integration of these data suggests that recharge, assimilation, storage at different levels below the volcano, and homogenization occur in Alicudi's magmatic system. Magma bodies shoaled and coalesced as the volcanic system matured.

Understanding the physical and geochemical constraints of magma formation in plumbing systems enhances eruption prediction and hazard mitigation.

TABLE OF CONTENTS

TABLE OF CONTENTS (continued)

LIST OF TABLES

LIST OF FIGURES

LIST OF FIGURES (continued)

CHAPTER I

INTRODUCTION

Documenting key magmatic processes that lead to compositional diversity can provide a framework for evaluating volcanic hazards. For example, magma composition affects degree of explosivity, which impacts hazard mitigation. Volcanoes in subduction zone settings, such as those in the Aeolian arc, Southern Tyrrhenian Sea, Italy (Figure 1), are known to be compositionally diverse and explosive, creating potentially dangerous conditions to surrounding populations (Clynne, 1999). Magmatic differentiation is dominated by three processes that occur in magma chambers: magma recharge, crustal assimilation, and fractional crystallization (RAFC) (Spera and Bohrson, 2004). Recharge of more mafic magmas into a host magma reservoir is evident in arc settings as documented by crystal growth histories (e.g., Ginibre et al. 2002; Tepley et al., 1999). Geochemical characteristics of arc magmas, such as $^{87}Sr/^{86}Sr$, show trends consistent with varying degrees of crustal contamination (Davidson et al., 2005; Peccerillo et al., 2004). Crystal-melt separation, leading to the process of fractional crystallization, likely occurs in most magma chambers. Documenting the relative roles that RAFC have as magma evolves in a magmatic plumbing system helps volcanologists better describe chemical and physical properties of magma. These properties, and the locations and volumes of magma chambers can, in turn, help volcanologists better predict eruption style and size and may also lead to better understanding of precursory signals of eruption that may help with hazard mitigation.

Figure 1. Schematic map of the Aeolian Island Arc with Alicudi at the western most end of the arc. Sicily is located at the southern end of map, with towns Milazzo and Case Longo marked by grey polygons. Inset shows location of Aeolian Arc in relation to Naples, Rome, and Palmero, which is on the island of Sicily (After Einstein, 2005).

The Aeolian arc is particularly interesting because it is a part of a subduction zone, and the volcanoes have produced a variety of volcanic products and compositions. Numerous studies have provided geochemical and petrological data from the arc (e.g., Bonelli et al, 2004; Francalanci et al., 1993; Peccerillo et al., 2004, Peccerillo and Wu, 1992). Aeolian Island rocks are separated into 5 types: calc-alkaline, high-K calc-alkaline, shoshonitic, and potassic, which appear above sea level, and tholeiitic lavas, which are found below sea level (Francalanci et al., 1993). Volcanic compositions

found on the islands range from basalts to rhyolites (50-75 wt. % SiO_2) (Ellam et al., 1988). Lavas found in the Aeolian arc show variable trace element trends and isotopic signatures that likely reflect heterogeneous mantle sources and interaction between crustal wall rock and magmas (Ellam et al., 2008; Francalanci et al., 1992; Peccerillo et al., 2004).

Alicudi, the western-most island in the Aeolians, is of importance to the study of the evolution of Aeolian arc magmas because it has the most primitive major and trace element signatures in the arc (Peccerillo et al., 2004). Alicudi's composition ranges from basalts to andesites (50-60 SiO_2 wt. %), and the andesites have the lowest documented Sr isotopic signatures (0.7035-0.7040) in the Aeolians (Bonelli et al., 2004; Ellam et al., 2008; Peccerillo et al., 2004). According to Peccerillo et al. (2004), low Sr isotope and primitive MgO signatures found on Alicudi represent the best candidate for parental melts for the entire Aeolian arc. Additionally, high-pressure ultramafic xenoliths have been found in Alicudi's primitive lavas, allowing an opportunity to investigate mantle composition. Variations in Alicudi's whole rock major and trace element and isotope trends suggest source heterogeneity and interactions between magmas and wall rocks (Peccerillo et al., 2004). Although Alicudi is no longer considered active, the processes that have occurred there may be compared to those at potentially active volcanoes, including those found in the Aeolian Island Arc (Vulcano and Stromboli) and those in the Cascades, Japan, Mexico, and Italy.

Thus far, assimilation and source heterogeneity have been identified on Alicudi through whole rock major and trace element and isotopic data (Peccerillo et al., 2004,

Francalanci and Manetti, 1994). This work provides the foundation for additional

studies that include application of experimental and numerical models and

characterization of plagioclase crystallization history. These techniques can be used to

record RAFC processes. Experimental and numerical models, such as comparison of

observed crystal and magma compositions with results of phase equilibria assimilation-

fractionation simulations (MELTS), can be used to constrain density, temperature,

viscosity etc. as a function of melt composition (Bohrson and Spera, 2001; Ghiorso and

Sack, 1995; Ginibre et al., 2002). Application of these models to natural data sets can be

challenging because parameters such as oxygen fugacity, pressure, water content are not

always well constrained. A complementary approach used to identify RAFC processes

uses zoning in plagioclase. Major element zoning patterns of the Albite-Anorthite (Na-

Ca end members) system are used to study plagioclase in igneous rocks as magma

chamber conditions change during crystal formation (Ginibre et al., 2002). Plagioclase

can also record changes in trace elements and isotopes during crystal growth (Davidson

et al., 2007; Ramos et al., 2004). Coupling major and trace element and isotopic

plagioclase data with plagioclase textures has shown the relative roles that RAFC

processes have in magmatic systems (Ginibre et al., 2002; Ramos et al., 2004; Salisbury

et al., 2008). A complete collection and comparison of numerical modeling, whole rock

major and trace element and isotopic data, and *in situ* plagioclase data is a powerful way

to identify magma chamber processes, such as RAFC, on Alicudi.

The objective of this study is to document the role of magma chamber processes

on Alicudi by evaluating whole rock major, trace, and isotopic data, and *in situ*

plagioclase textural, major and trace element, and radiogenic isotopic data. In addition,

these data are used to constrain numerical models (via MELTS) that yield hypotheses

about open system processes. This study represents the first report of *in situ* plagioclase

data at Alicudi and is also the first, to our knowledge, to integrate whole rock data with

numerical modeling at Alicudi. The new hypothesis that emerges from Alicudi whole

rock and plagioclase data is mixing, assimilation, storage, and homogenization (MASH,

cf. Hildreth and Moorebath, 1988) from stages 1 and 2 basalts/basaltic andesites to

stage 3 andesites.

CHAPTER II

BACKGROUND

Geologic Setting and Volcanic History of Alicudi, Aeolian Island Arc, Italy

Alicudi volcano is the western-most island of the Aeolian Island arc, located in

the Tyrrhenian Sea, north of Sicily (Figure 1). The arc stretches for 200 km and is built

on the Colabro-Peloritan continental margin, a piece of an orogenic belt emplaced

during the opening of the Tyrrhenian Sea (Peccerillo et al., 2004). The crustal thickness

varies around the region: 40-45 km under Calabrian continental margin, 15-20 km

under the Aeolian arc, and 10 km under the Tyrrhenian abyssal plain (Nazzareni, 2004).

Aeolian Island arc volcanism is attributed to complex NW-subduction of the African

Plate beneath the European Plate (Francalanci et al., 1993). A dextral strike-slip fault,

extending from the island of Salina to northeast Sicily, separates the arc into two

sections that are distinctly different geophysically and petrologically (Figure 2)

(Peccerillo et al., 2004; Calanchi et al., 2002). The western volcanoes (Alicudi,

Filicudi, and Salina) are principally calc-alkaline compositions, whereas shoshonitic

and potassic magmas are found in the central and eastern areas (Vulcano, Lipari,

Panarea and Stromboli).

The island of Alicudi represents the summit of a complex stratovolcano that has

its base at 2000 m below sea level and its summit 675 m above sea level (Nazzareni et

al. 2001). Of all the islands, Alicudi has the highest Mg number (Mg # up to 73, Ni up
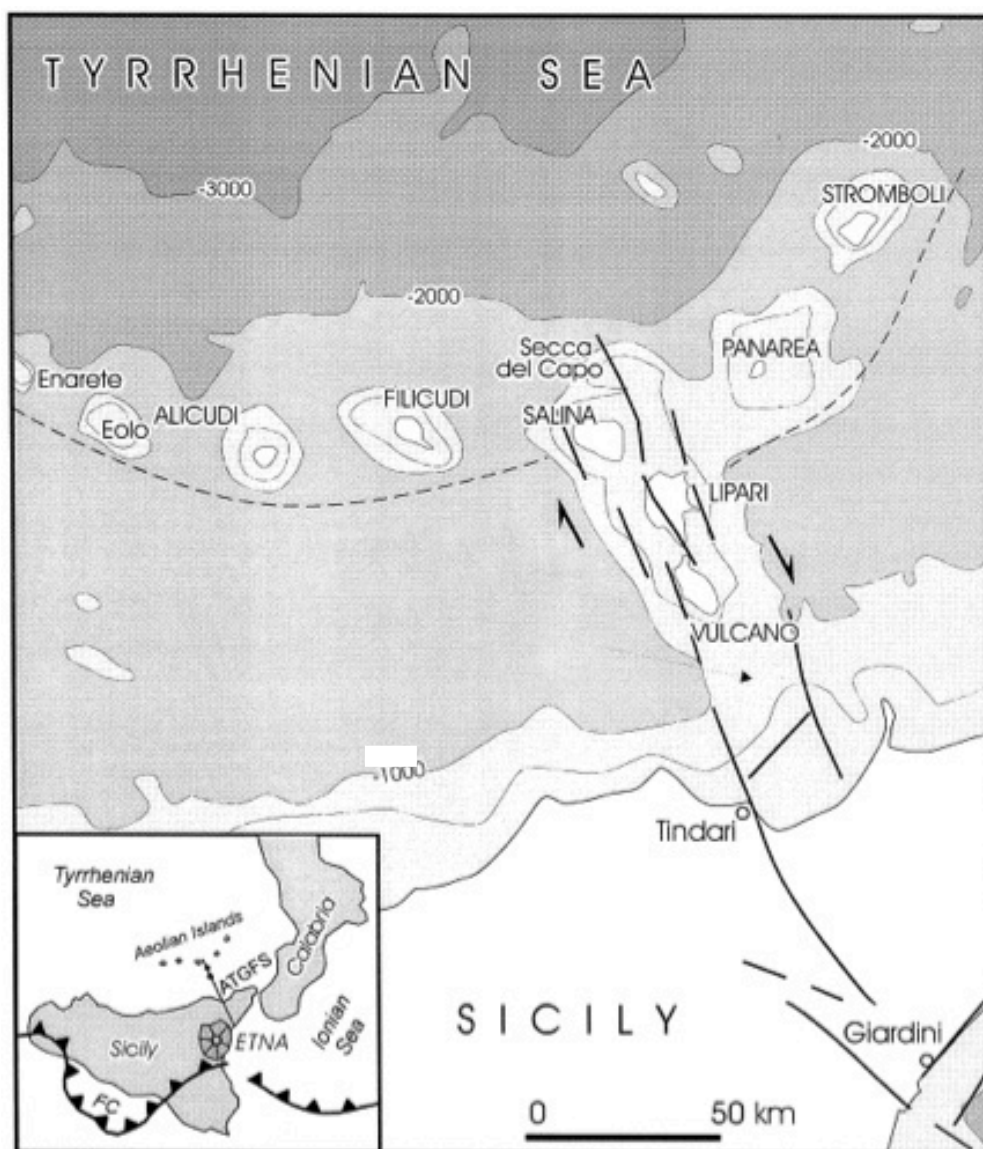
Figure 2. The Aeolian volcanic system in its seismo-tectonic (bold lines) and bathymetric regional framework. The dashed line indicates the southern base of the volcanic edifices (arc front). Inset map: FC- front of Apennine-Maghrebian Chain, southern margin of European plate; ATGFS- Aeolian-Tindari-Giardini fault system (Modified from Falsaperia et al., 1999).

to 150 ppm, and Cr up to 800 ppm) (Peccerillo and Wu, 1992). Alicudi is dominantly

composed of 167-28 ka lava flows and small volumes of pyroclastic flows that range in

composition from calc-alkaline basalt to andesite (Bonelli et al. 2004; Lucchi et al.,

2004). Three eruptive stages separated by caldera collapses have been identified: stage 1 basalts and basaltic andesites (90-167 ka), stage 2 basalts and basaltic andesites (60-55 ka), and stage 3 andesites (28 ka) (Bonelli et al., 2004; Lucchi et al., 2008; Peccerillo et al., 2004). The first two stages are separated by central caldera formation and are characterized by basaltic and basaltic andesitic lavas and pyroclastic products. Andesitic lavas and domes emplaced in the summit crater and on the southern flank of the cone characterize the third phase (Peccerillo et al., 2004; Peccerillo and Wu, 1992).

Twelve stratigraphic units have been identified on Alicudi (Figure 3) (Lucchi et al., 2008). Stage 1 encompasses the oldest units: Scoglio Galera 1 formation (ga), Scoglio Galera 2 formation (gf), Scoglio Galera 3 formation (gr), and Scoglio Galera 4 formation (sg). These are described as alternation of lava flows and scoriaceous beds (fallout eruption units). Lava flows are made of calc-alkaline basalts to basaltic andesites. Stage 2 contains units from the Punta Malopasso formation (pm). Punta Malopasso is separated into two sub units: pm1 is described as alternation of lava flows and scoriaceous beds. Lava flows are made of calc-alkaline basalts and basaltic andesites; pm2 is a calc-alkaline andesitic lava dome. Stage 3 is made of units Punta Fucile formation (pf), Chierica formation (ch), Faro formation (~fa), Pianoconte formation (pi), Piano di Mandra formation (pmn), and Filo dell'Arpa formation (fa). Unit pi is described as lower-intermediate brown tuffs. Unit ~fa contains marine littoral deposits. All other units in stage 3 are described as alternation of lava flows and scoriaceous beds. Lavas are calc- alkaline andesites (Figure 3). Plagioclase is an abundant phase in all volcanic products found on Alicudi. $^{87}Sr/^{86}Sr$, measured
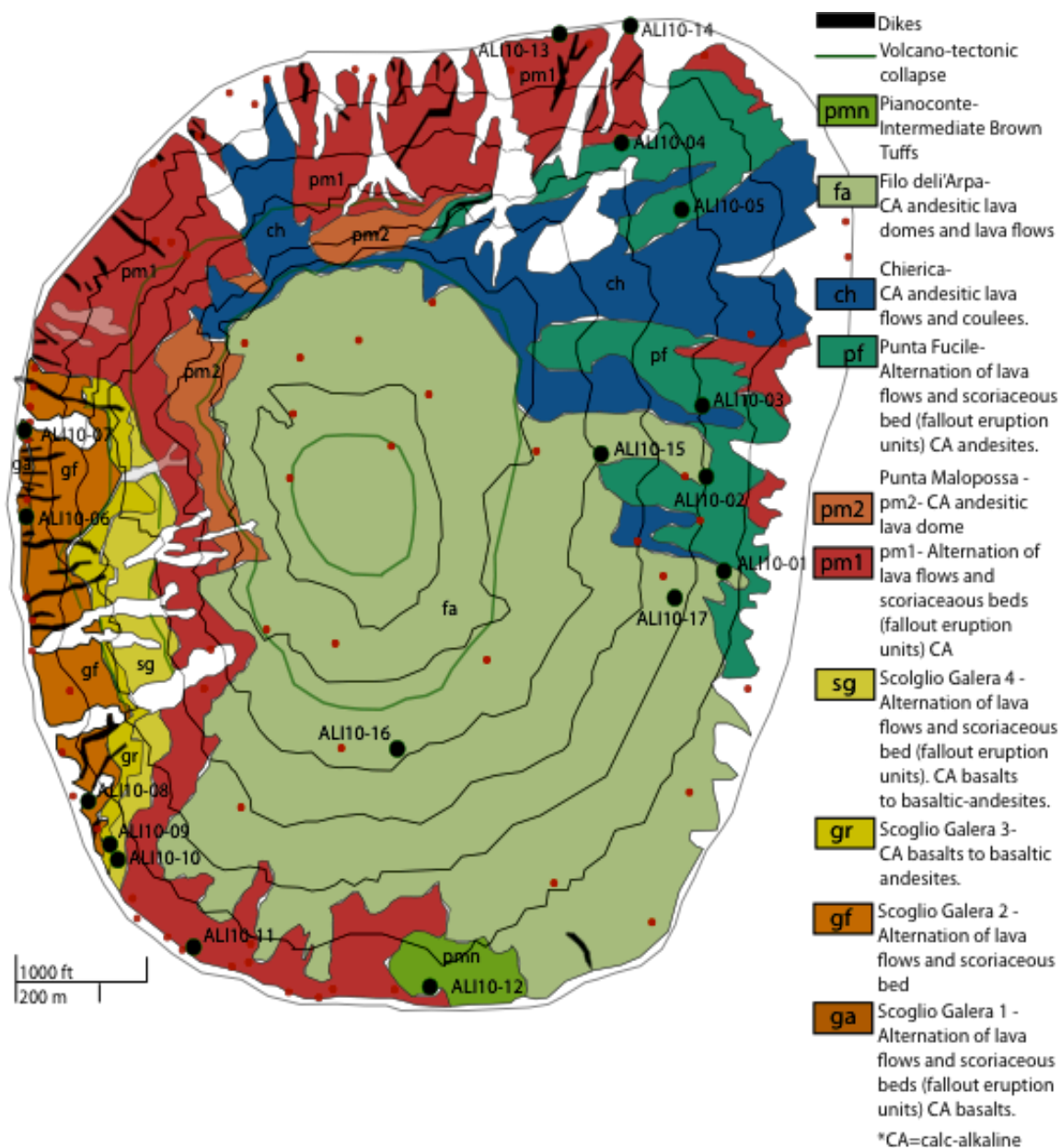
Figure 3. Simplified geologic map and stratigraphy of Alicudi Island (Modified from Lucchi et al., 2008). The youngest units are found in stage 3, which are represented by pmn, fa, ch, and pf. Stage 2 is represented by pm2 and pm1. The oldest units are in stage 1, which are represented by sg, gr, gf, and ga. Red dots are sample locations of Peccerillo et al., 2004. Black dots are locations of samples collected in May 2010.

in whole rock, clinopyroxene, and plagioclase range from 0.7037-0.7040; the highest

whole rock $^{87}Sr/^{86}Sr$ values are seen in the basalts (Peccerillo et al. 2004).

Contrasting Hypotheses on the Origin of Alicudi Magmas

Two end-member hypotheses have been proposed for the origin of magmas on

Alicudi. (1) As suggested by trapping pressures of CO_2 fluid rich fluid inclusions in

quartz xenoliths found in Alicudi samples, stages 1 and 2 formed in a deep magma (24

km) reservoir by assimilation and fractional crystallization, and stalled in a shallow

reservoir (6 km) on their ascent to the surface. Stage 3 formed solely in a shallow

reservoir by fractional crystallization (1 km) (Bonelli et al., 2004). (2) Trace element

and isotope trends suggest all stages formed in a single magma reservoir, were supplied

by a heterogeneous mantle source, and assimilated with conduit crustal wall rock prior

to eruption. Andesites experienced little to no assimilation due to their cooler

temperatures (Peccerillo et al., 2004).

The first hypothesis is supported by a fluid inclusion study by Bonelli et al.

(2004). Two types of CO_2-rich fluid inclusions are present in quartz xenoliths found in

all eruptive stages. Early inclusions (Type I), found in stages 1 and 2, indicate trapping

pressures of 6 kbar (~24 km depth) suggested by isochoric calculations. Late inclusions

(Type II) show lower trapping pressures of 0.2 to 1.7 kbar (~1 km – 6 km depth) and are

found in all stages. The presence of both Type I and Type II inclusions in stages 1 and 2

suggests two depths of formation (24 km and 6 km). Thus, Bonelli et al. (2004) suggest

that stages 1 and 2 underwent assimilation and fractional crystallization (AFC) in a deep reservoir, and spent little time in the shallow reservoir where minimal fractional crystallization occurred. Only Type II inclusions are seen in stage 3, suggesting that stage 3's formation occurred in a shallow chamber (1 km) and evolved solely by fractional crystallization (Bonelli et al. 2004).

In support of this hypothesis, cell and M1 site volume changes in clinopyroxene from Alicudi have been inferred to suggest that clinopyroxene crystallization pressures changed (Nazzareni et al. 2001) and thus, magmas had a polybaric crystallization history.

Alternatively, Peccerillo et al. (2004) focused on systematic major and trace element variations and primitive Sr-Nd-O isotopic signatures, and suggested that all stages evolved from mafic magmas by fractional crystallization. However, a decrease in $^{87}Sr/^{86}Sr$, seen from basalts to andesites, requires that fractional crystallization was not the sole differentiation process. Peccerillo et al. (2004) conclude that Sr-Nd-O isotope signatures suggest fractional crystallization occurred in deep magma chambers, and assimilation occurred just prior to eruption as magmas ascended through conduits. Contamination of basaltic magmas by melts of wall rock was more likely (stages 1, 2), because they are hotter and less viscous compared to andesites (stage 3) (Peccerillo et al. 2004; Peccerillo and Wu, 1992). In addition, Alicudi has the most primitive $^{87}Sr/^{86}Sr$ of all the islands. In plots of $^{206}Pb/^{204}Pb$, $^{87}Sr/^{86}Sr$, and $^{143}Nd/^{144}Nd$ isotopes, most volcanoes in the arc follow a mantle reservoir/ upper crustal trend. In contrast, Alicudi andesites fall along a hybrid mantle reservoir trend. Therefore, it is suggested that

source heterogeneity and fluid addition on Alicudi also contribute to compositional

diversity for all stages (Peccerillo and Wu, 1992).

Processes that Lead to Compositional Diversity

Magma compositional diversity is dominated by a combination of three

processes: (1) recharge, (2) assimilation, and (3) fractional crystallization (RAFC).

Crystal-melt separation, typically modeled by fractional crystallization, occurs in many

volcanic settings (e.g., Bohrson and Spera, 2001). Fractional crystallization is defined as

the crystallization and segregation of a mineral from a melt, and is considered a closed

system process.

Recharge and assimilation are the result of open system processes where an

existing magma interacts with its external environment (Streck, 2008). Magma recharge

occurs when a new melt ±crystals (called recharge magma) intrudes into an existing

mass of melt±crystals (called resident or host magma). Magma mixing or mingling,

which typically accompanies recharge and results in compositional change, most

commonly involves mafic magmas mixing with more silicic magmas to form hybrid or

mingled magmas. The importance that recharge and magma mixing have in developing

compositional diversity was recognized as early as 1851 by Bunsen (Streck, 2008), but

was more widely recognized, particularly in the mid-ocean ridge environment,

beginning with the work of Eichelberger, 1975.

Several well-studied examples of recharge and magma mixing highlight their importance. The 1991 Pinatubo eruption involved a crystal-poor basaltic magma that intruded into crystal-rich dacitic magma, yielding a hybrid andesitic magma. Quenched magmatic inclusions are evidence of quenching of the hotter basaltic magma by the cooler dacitic magma (Pallister et al., 2006). Another example is mixing of high-silica rhyolitic and basaltic andesitic magmas to form dacitic magmas is the Rattlesnake Tuff (Streck, 2008). Basaltic andesitic magmas were quenched by cooler rhyolitic magmas. Although these two examples from different tectonic settings had different host melt compositions, the hybrid magma compositions were similar. In some cases, recharge may involve multiple mixing events with variable magma compositions and temperatures. Self-mixing of a magma body can also occur when there is a temperature difference within the magma body. This closed system process leaves traces in the mineral record as temperature increase may cause resorption of plagioclase, followed by crystallization (e.g., Streck, 2008).

Along with recharge, crustal assimilation also plays an important role in magma evolution. Crustal assimilation is the process in which crustal wall rock (called assimilant) mixes with a melt in the magma chamber (called resident or host magma), also causing a change in composition of magma chamber melts. Assimilation and fractional crystallization are typically coupled because the thermal requirements for melting of wallrock are provided by latent heat of crystallization (Bohrson and Spera, 2001). The importance of the connection between fractional crystallization and assimilation has been recognized for almost a century, at least since the seminal

publication of Bowen (1928). Assimilation can occur in a variety of ways. For example,

partial melts of wallrock can be incorporated into host magma. In addition, completely

dissolved crystals, country rock, and disintegrated country rock that disperses its

crystals can contribute a crustal signature (Streck, 2008). An example of crustal

assimilation is seen at the Skye Igneous Centre, Western Scotland. Energy-Constrained

Recharge, Assimilation and Fractional Crystallization (EC-RAFC) models were used to

understand variations in Sr- and Pb- isotopic composition of exposed rocks at the Skye

Igneous Centre. The best-fit models suggested that the character of the crustal

assimilant affecting the magmatic products of the Skye igneous centre changed

systematically from lower-crustal granulite, to middle—crustal amphibolite, to upper

crustal metasediments (Fowler et al., 2004).

As a consequence of RAFC, minerals can form in and separate from magmas,

and melt can evolve, typically to more Si-rich compositions. As minerals grow from

core to rim during closed and open system processes, they record the thermal and

chemical characteristics of the adjacent magma. Whole rock and crystal compositional

and textural changes can be preserved, and used to reconstruct conditions of melt and

crystal formation and evolution.

Whole Rock Compositional Data

Compositional relations among magmas in a single setting provide powerful

constraints on their differentiation. Major elements, compatible and incompatible trace

elements and radiogenic and stable isotopic data provide evidence for RAFC processes (e.g., Bohrson and Reid, 1995; Bohrson and Reid, 1997; Clynne, 1999; Davidson and Dungan, 1987; Furman et al., 1992; Hildreth and Moorebath, 1988; Peccerillo et al., 2004; Peccerillo and Wu, 1992).

For example, there is an abundance of whole-rock data that supports involvement of crustal assimilants in the evolution of magmas. Trace elements, such as Rb, Ba, La, and Y have been used to document crustal contamination. Large decreases in K/Rb and large increases in La/Yb seen at San Pedro-Pellado diverge greatly from fractional crystallization trends (Davidson and Dungan, 1987). Even in cases where Rb is perfectly incompatible (distribution coefficient of 0), 90% fractionation is required to generate dacites and rhyolites (150 ppm Rb) from basaltic andesites (10-20 ppm Rb). In order for 90% fractionation to be obtained with given values of Rb, hornblende must be an important fractionating phase. However, hornblende is not observed at San Pedro-Pellado. Thus, Davidson and Dungan (1987) concluded that trace element trends seen at San Pedro-Pellado suggest contamination of crustal components. Similarly, elemental ratios such as K/Rb, Zr/Hf, Ba/La from a cross-arc segment of the Andean arc represent intra-crustal contamination (Hildreth and Moorebath, 1988).

In addition to trace elements, radiogenic isotopic data can provide strong evidence of crustal assimilation. As seen in many volcanic settings, increasing $^{87}Sr/^{86}Sr$ with SiO_2 suggests interactions between magma and crustal wall rock (Bohrson and Reid, 1997; Ramos et al., 2004). In some cases, constant or decreasing $^{87}Sr/^{86}Sr$ with

increasing SiO_2 is evidence of assimilation of a low $^{87}Sr/^{86}Sr$ component (Wolff et al., 2005).

Another addition to the important record provided by whole rock data in constraining open system processes is crystals, such as plagioclase, which can record open and closed system magma chamber conditions. The importance of *in situ* crystal work is described below.

In situ Plagioclase Textural and Compositional Data as a Record of Magma Chamber Processes

Due to its slow rate of re-equilibration, stability in a wide range of magma compositions, and ability to respond to changes in magma chamber dynamics, plagioclase can provide a record of changing magma chamber conditions. *In situ* compositional work on plagioclase in volcanic rocks has documented the occurrence and relative timing of magma chamber processes such as RAFC, as well as provided evidence for magma decompression and convection (Ginibre et al. 2007). Similarly, *in situ* core to rim micro-sampling of plagioclase for $^{87}Sr/^{86}Sr$ provides evidence for magma mixing or contamination (e.g., Davidson et al., 2007).

Plagioclase Textural Data

Although different magma chamber processes, such as recharge or assimilation, can cause an array of textural patterns in plagioclase, it is important to couple textural changes with changes in major and trace element and radiogenic isotopes to definitively

distinguish the dominant processes. Open system processes can be "recorded" in plagioclase as different textures or zoning patterns as single crystals respond to changes in melt composition, volatile content, and/or temperature (Humphreys et al., 2009; Streck, 2008; Viccaro et al., 2010).

Nomarski Differential Interference Contrast Imaging (NDIC) and Back Scatter Electron Imaging (BSE) are used to identify textures in plagioclase. Zoning is defined as compositional changes in the mineral from core to rim as would be induced by compositional changes in the melt as it follows a liquid line of descent (Streck, 2008) or as caused by changes in parameters such as pressure, oxygen fugacity (fO_2), or temperature (Ginibre et al., 2002). Several types of zoning and textures that are relevant to this study are discussed below; this discussion is primarily taken from Streck (2008).

Oscillatory zones are compositionally varying growth-shells or layers that are generally parallel to crystallographic planes of low Miller indices and have thicknesses ranging from tens of nanometers to several tens of micrometers. Growth of thinner oscillatory bands is typically kinetically driven, whereas thicker bands reflect dynamic magmatic processes. Monotonous zones lack textural change from core to rim, have systematic variations in major and trace elements, and are typically associated with faster growth rates than those of oscillatory zones. Normal oscillatory or monotonous zones occur when anorthite, the Ca end member in plagioclase, decreases as the crystal grows from core to rim, whereas reverse zones occur when anorthite increases as the crystal grows from core to rim. Patchy zones are irregularly distributed zones and can result when crystallization into partially resorbed areas of a cyrstal produces solid

material in the resorbed areas that is different than that of the host crystal. Patchy

zoning can also occur when a crystal reequilibrates through diffusion. Dissolution

surfaces (or resorption rims) occur when dissolution of crystalline material occurs on

the exterior surfaces of a crystal; the result is typically faces that are rounded and

anhedral. Sieve textures occur when resorption of the entire crystal leads to an open,

cellular mineral structure. Dissolution surfaces and sieved textures can be caused by

rapid decompression or changes in melt composition or temperature.

Plagioclase Major, Minor, and Trace Element Data

Documentation of plagioclase compositions, using the electron microprobe has

led to recognition that the mineral records crystallization conditions (e.g., magma

composition, pressure, H_2O content) (Ginibre et al., 2002). A critical compositional

indicator in plagioclase is Anorthite (An)- Albite (Ab), Ca-Na end members of

plagioclase. Through fractional crystallization in a closed magma chamber system,

simple zoning is likely produced in plagioclase as a result of small variations in major,

minor, and trace elements. For example, a normally zoned plagioclase will decrease in

An (defined as Ca/(Ca+Na)*100) content from core to rim (normal oscillatory zones)

and may have as much as 30% variation in An content from core to rim (Humphreys et

al., 2006). However, if recharge or assimilation events occur, plagioclase may show

large variations from core to rim or sharp increases or decreases in major, minor, and

trace elements over textural boundaries. Such variations yield complex zoning. In this

scenario, plagioclase can have increasing An content from core to rim or have changes

of ≥10 mole % in An content across individual textural boundaries (5-10 microns). In

most arc rocks, plagioclase crystals show complex zoning patterns (Davidson et al., 2007; Ginibre et al., 2007; Humphreys et al., 2006; Streck, 2008; Viccaro et al., 2010).

In one study on Parinacota volcano, moderate An discontinuities of greater than 10 mole % and decreasing concentrations of some trace elements (Fe, Ti) rimward suggest recharge of a more mafic magma (Ginibre et al., 2002). In another study of volcanic rocks from Mount Etna, enrichment of ΔAn_{10-30} (i.e., change in An content over a spatial scale of 5 microns or across a textural boundary) and FeO increase suggest a recharging phase of more primitive, undegassed magma (Viccaro et al., 2010). An additional case study at Shiveluch Volcano shows normal oscillatory zoned plagioclases have diffuse, symmetrical zones in the cores (i.e., Fe/Al increases with decreasing An content), suggesting partial re-equilibration during long residence times in the magma chamber. Outer zones of plagioclase exhibit a sharp boundary to higher An, then an increase to a more albite-rich composition. The sharp change in An is attributed to recharge with mafic melt (Humphreys et al., 2006).

Plagioclase Strontium Isotope Analyses

Radiogenic isotopes can be used to identify open-system processes such as recharge or crustal assimilation (e.g., Davidson et al., 2007, Bohrson and Spera, 2001, 2004). Because of the abundance of Sr in plagioclase, *in situ* $^{87}Sr/^{86}Sr$ work can be used to document these processes.

Whole rock isotopes reflect and integrate a record of the Sr isotope history for all of the components of the whole rock; in contrast, element and isotope compositional profiling of plagioclase within the context of textures provides a record of changing

chamber dynamics during the time of crystal growth (Davidson et al., 2005). Variations in $^{87}Sr/^{86}Sr$ across single plagioclase crystals can show recharge of new melt or assimilation of crustal material. Typically, increases of whole rock $^{87}Sr/^{86}Sr$ are consistent with assimilation from crustal contamination. Similarly, increases of Sr isotopes rimward within individual plagioclase crystals suggest assimilation of a crustal component played an important role during crystal growth (Ramos and Reid, 2005; Tepley et al., 1999). In other cases, a decrease in $^{87}Sr/^{86}Sr$ may be evidence of a recharge event with a more mafic magma (Davidson et al., 2007). In rare cases, a decrease in $^{87}Sr/^{86}Sr$ may be caused by contamination by crust characterized by $^{87}Sr/^{86}Sr$ that is lower than the host/resident magma (Ramos and Reid, 2005). Although heterogeneous isotope signatures identify processes of assimilation, quantitative modeling can potentially document the composition of the assimilated component.

MELTS

Comparison of observed magma and crystal compositions with results of phase equilibria assimilation-fractional crystallization simulations (MELTS) can quantitatively document the conditions at which open-system processes occurred within a magmatic plumbing system. MELTS (Ghiorso and Sack, 1995) combines water content, fO_2, pressure, and temperature parameters with thermodynamic properties to predict mass and major element compositions of minerals and melts. Requiring a range of input parameters such as parental magma composition, pressure, and initial H_2O

abundance and $f\mathrm{O}_2$, MELTS defines the temperature, mineral assemblages, composition (including An content of plagioclase) and masses, and melt composition and mass. An example of the utility of this computational tool can be seen in the case study of the Campanian Ignimbrite by Fowler et al. (2007). Using a range of input parameters, best fit MELTS models illustrated the most likely pressure of magma differentiation and identified the likely involvement of wall rock assimilation of a small mass of upper crustal skarn and foid-bearing syenite; these rocks make up the crust beneath Campania (Fowler et al., 2007).

CHAPTER III

METHODS

Field Work and Sample Collection

In May 2010, using geologic maps of Alicudi (Figure 3), a field party and I collected samples of each lava flow lithologic unit exposed on Alicudi, Italy for detailed analysis. Seventeen samples, ALI10-01 - ALI10-17, were collected (Table 1) and analyzed for whole rock major and trace elements and isotopes. Detailed *in situ* plagioclase analysis was performed on ten fresh samples (ALI10-01, 03, 05, 07, 08, 09, 10, 11, 12, 17) that were chosen to represent lava flows from ten units exposed on Alicudi (ga, gf, gr, sg, pm1, pm2, pf, ch, fa, pmn). Units not included in this study were tuffs and scoriaceous beds (fallout eruption units) (pi) or were not accessible (pm2). For each representative sample, one 30 μm thin section and one 100 μm thick section were produced. Thin sections were used for petrographic analysis; thick sections were used to collect *in situ* plagioclase textural, major and trace element, and Sr isotope data.

Whole Rock Major and Trace Element Analysis

Whole rock data were gathered from Washington State University's (WSU) X-ray fluorescence (XRF) and inductively coupled mass spectrometry (ICP-MS) lab. Methods used for whole rock data were adapted from those used at WSU. XRF was

TABLE 1. STRATIGRAPHY OF SAMPLES COLLECTED ON ALICUDI

Stratigraphy	Stage	Sample Names	Lat	Long	Elev.	Whole Rock Name	Ages from Lit*	Creamers Ages*
Dikes		ALI10-06	N 38.54	E 14.33	7 m	Basalt	?	NA
pmn	3	ALI10-12	N 38.53	E 14.35	15 m	Andesite	?	NA
fa	3	ALI10-16	N 38.53	E 14.35	425 m	Andesite	28 ka	NA
fa	3	ALI10-17	N 38.54	E 14.36	253 m	Andesite	28 ka	NA
fa	3	ALI10-01	N 38.54	E 14.36	203 m	Andesite	28 ka	NA
fa	3	ALI10-15	N 38.54	E 14.35	413 m	Trachy Andesite	28 ka	NA
pf	3	ALI10-02	N 38.54	E 14.36	219 m	Trachy-andesite	28 ka	NA
ch	3	ALI10-03	N 38.54	E 14.36	230 m	Trachy-andesite	28 ka	NA
pm2	2	NO SAMPLE						NA
pm1	2	ALI10-04	N 38.55	E 14.35	309 m	Basaltic Andesite	60-55 ka	NA
	2	ALI10-05	N 38.54	E 14.36	240 m	Basalt	60-55 ka	NA
	2	ALI10-11	N 38.53	E 14.34	40 m	Basaltic Andesite	60-55 ka	59.3.3+/-1.3ka
	2	ALI10-13	N 38.55	E 14.35	10 m	Basaltic andesite	60-55 ka	NA
	2	ALI10-14	N 38.55	E 14.35	20 m	basaltic andesite	60-55 ka	NA
sg	1	ALI10-10	N 38.53	E 14.34	30 m	Basaltic Andesite	90 ka	NA
gr	1	ALI10-09	N 38.53	E 14.34	20 m	Basaltic Andesite	90 ka	66.8 +/-1.0 ka
gf	1	ALI10-08	N 38.53	E 14.34	10 m	Basalt	90 ka	64.1 +/- 4.1 ka
ga	1	ALI10-07	N 38.54	E 14.33	5 m	Basaltic Andesite	90 ka	167 +/- 21.6 Ka

*Peccerillo et al., 2004; Creamer, pers. communication
* Refer to Figure 3 for geologic map of Alicudi

used to document whole rock major and trace elements abundances, whereas ICP-MS wa s used to determine whole rock trace elements. ICP-MS is specifically used for its superior detection capabilities of rare earth elements (REEs) or any element with an abundance of <10 ppm (Jenner et al., 1990). For XRF and ICP-MS preparation (Johnson et al., 1999), fresh chips, broken in the field, were chosen (about 28 g) and ground in a swing mill with tungsten carbide surfaces for 2 minutes. For XRF data collection, 3.5 g of sample powder were weighed into a plastic mixing jar with 7.0 g of spec pure dilithium tetraborate ($Li_2B_4O_7$). The sample dilithium tetraborate mixture was poured into a graphite crucible. A set of 24 crucibles was placed on a silica tray and loaded into a muffle furnace, where the mixture was fused for 30 minutes, and then was allowed to cool to a glass "bead." Each cooled bead was reground in the swing mill for 35 seconds. The resulting glass powder was placed back in the furnace for 30 minutes and taken out for cooling. Once the second fusion was complete, each bead was labeled and polished. The samples were then placed in the ThermoARL Advant'XP+ sequential XRF.

X-ray intensities of 27 major and trace elements were measured on standards from two USGS sample beads and two beads of pure quartz (Johnson et al., 1999). Standard X-ray intensities were then compared with X-ray intensities of unknown Alicudi beads. Standard beads are run to recalibrate the instrument once every 3 weeks or after 300 unknowns are analyzed. Two USGS standard beads were used as internal standards and were run between every 28 unknowns. This use of standards continually checks instrumental performance and measures instrumental precision within a single

run or between runs that occur over longer periods. Tungsten, tantalum, and cobalt are
not analyzed due to contamination from the tungsten carbide mills. To measure
accuracy, WSU GeoAnalytical Laboratory uses the scatter of the standard samples
around the calibration curve for each element and compares standard values to those of
the same samples analyzed by other workers in different laboratories using different
techniques. The amount of scatter of any one sample is calculated from a calibration
curve drawn through all 20 analyzed standard beads. Observed WSU XRF values are
compared to the given values by Govindaraju (1994) normalized to 100% on a volatile-
free basis. When compared with other XRF laboratories (USGS-Denver, Rhodes
University- South Africa, and XRAL- Canada), the WSU data sets have consistently
lower Fe (0.3% FeO) and higher Si (0.45% SiO_2). In all cases, the biases are within
natural variation and are unlikely to have significance in petrologic studies (Johnson et
al., 1999). Precision for measurements of elements on XRF is 2σ: major elements
≤1.0% except for MgO, Na_2O and MnO, which are ≤1.5%; Ni, Cr, Sc, V, and Nb ≤8%;
Ba, Rb, Sr and Zr ≤2.5%; abundances ≤10 p.p.m. qualitative only.

For ICP-MS data collection, 2 g of ground rock sample was mixed with 2 g of
$Li_2B_4O_7$ and weighed into a plastic mixing jar. The mixture was placed in a carbon
crucible and fused at 1000° C in a muffle furnace for 30 minutes. After cooling, the
fused bead was ground in a carbon-steel ring mill, and 250 mg of the powdered bead
was placed into a 30 mL, screw top Teflon PFA vial for dissolution. Next, this mass
was dissolved with 2 mL of HNO_3, 2 mL of HF, and 2 mL of $HClO_4$ at 110° C. After
evaporation, the sample was wetted with a small amount of water, and a second

dissolution/evaporation involved 2 mL of $HClO_4$ at 160° C. After the second evaporation, the samples were mixed into a solution of 10 mL of water, 3 mL of HNO_3, 5 drops of H_2O_2, 2 drops of HF, and warmed on a hot plate until the solution cleared. The sample was then transferred to a clean 60 mL HDPE bottle and diluted up to a 60 g with de-ionized water.

Analysis of solutions was done on an Agilent model 4500 ICP-MS, and the solution was diluted an additional 10 times at the time of the analysis using Agilent's Integrated Sample Introduction System. Three rock standards were interspersed within each batch of 18 unknowns. Instrumental drift (intensity and peak position) is corrected using Ru, ln, and Re as internal standards. Precision for ICP-MS method is typically better than 5% for REEs and 10% for the remaining trace elements (Jenner et al., 1990).

Microdrilling of Groundmass Samples

Microdrilling of groundmass from ten representative samples was completed at Oregon State University. Microdrilling collected ~1 mg of sample, which was followed by chemical separation, discussed below. Samples were drilled with a semi-automated New Wave Microdrill. A carbide scriber point HP dentist drill bit was used to microdrill groundmass in all samples, and a clean drill bit was used for every sample. Thick section slides were mounted on a metal disk with hot glue. A small square of parafilm was placed on the desired drill area, and the mount was loaded onto the microdrill stage. Once the mount was loaded, one drop of distilled H_2O was put into the parafilm square.

Micromill semi-automated program was set to drill a 600 μm long X 100 μm wide X 50 μm deep trough. After the trough was drilled, the sample and drop of H_2O were collected with a pipette and placed into a 7 mL Teflon beaker. An additional 2-3 drops of distilled H_2O were used to collect any remaining sample left on the slide within the parafilm.

Radiogenic Isotope Analysis

Whole Rock Chemistry

Whole rock Sr and Nd isotope analysis was performed at New Mexico State University (NMSU) in collaboration with Dr. Frank Ramos. Analysis was completed on seventeen whole rock samples (ALI10-01 - ALI10-17). Rock powders, ground at WSU, were weighed out to 100 mg and placed in 15 mL Teflon beakers. 3 mL of concentrated HNO_3, used to dissolve carbonates, organics, and sulfates, and 3 mL of concentrated HF, used to dissolve silicates, were added to powders, left to dissolve for 24 hours, and then dried on a hot plate. The resulting dried product was mixed with 6 mL of 7N HNO_3 to dissolve organics. The HNO_3 mixture was left to dissolve for 24 hours, and then dried. The last step in the dissolution process was adding 6 mL of 6N HCl to the dried product. HCl dissolves fluorite that may have formed as a result of adding HF. After the HCl mixture was dissolved for 24 hours and dried, 1 mL of 2.5N HCl was added. The resulting mixture was centrifuged for 3 minutes, and then column chromatography was used to separate Sr and Nd.

For Sr collection, 2.5N HCl was used. Pyrex glass columns filled with chromatography cation resin underwent a pretreatment of 10 mL of 2.5 HCl. Then, 0.5 mL of the sample was loaded into the column. Columns were washed with 0.5 mL, 2.5 mL, 6.5 mL, and 3 mL of 2.5N HCl. An additional wash of 5 mL was done before the collection of Sr. Sr was collected with 6 mL of HCl into a Teflon beaker, and this mixture was then placed on a hot plate to dry. Total collected Sr sample was ~10-20 µg. REEs were collected in a Teflon beaker with 10 mL of 6N HCl, and placed on a hot plate to dry. The columns were cleaned with 15 mL of HCl and backwashed with H_2O.

Dried REEs were mixed 0.50 mL of 0.25N HCl. Nd was collected using Pyrex glass columns filled with HDEMP chromatography resin. Columns were pretreated with 10 mL of 0.25N HCl, and then 0.5 mL of sample was loaded into each column. Two washes of 0.5 mL, one wash of 1 mL, and one of 4 mL of 0.25N HCl were completed before collecting Nd. Nd was collected with 6 mL of 0.25N HCl. Total collected sample of Nd was ~0.5 µg. The columns were cleaned with 15 mL of 6.0N HCl. Collected Nd was placed on the hot plate to dry.

Groundmass Microchemistry

One mg of each microdrilled groundmass sample was dissolved with 0.5 mL of concentrated HNO_3 and 0.5 mL of concentrated HF. The mixture was left to dissolve for 24 hours, and then dried on a hot plate. Next, 1 mL of 2.5N HCl was added to the dried sample, left on a hot plate to dissolve for 24 hours, and then dried. Similar to Sr whole rock chemistry, 2.5N HCl was used. Micro Pyrex glass columns were filled with chromatography cation resin. The resin was changed after 2 rounds of chemistry (one

cycle consists of sample loading, Sr collection, and washing), and prepared with two to three 6 mL washes of 6N HCl, followed by a backwash of distilled H_2O and three 6 mL washes of 2.5N HCl. Columns were pretreated with 2 mL of HCl. Then, 0.05 mL of the sample was loaded into the columns followed by 2 washes of 0.05 mL, 1 wash of 0.1 mL, 0.85 mL, and 0.7 mL of 2.5N HCl. Sr was collected with 0.7 mL of 2.5N HCl. Columns were cleaned with 8 mL of 6N HCl. Collected Sr samples were placed on a hot plate to dry.

Thermal Ionization Mass Spectrometry Analysis

Dried samples of Sr from whole rock and groundmass chemistry, and Nd from whole rock chemistry were re-dissolved with 1-2 µL of 5% HNO_3 and loaded onto a filament. Ten loaded filaments were loaded onto a turret and into a VG Sector 54-30 thermal ionization mass spectrometry (TIMS) source barrel assembly. The barrel was evacuated of atmospheric gases. Then, filaments were heated to ionize the loaded element (i.e. Sr, Rb, Nd) to form a beam that was accelerated down the flight tube of the mass spectrometer. The ion beam is composed of all the isotopes of the element (i.e. Sr, Rb, Nd) that are separated by a magnetic field, depending on the mass of the isotopes that make up the ion beam. Light masses are deflected more than heavy masses. Each beam has an individual mass, and each beam travels into one of seven faraday collectors. The charge of the ions of the collectors was measured. The intensities of the isotopes were compared with standard intensities and data were compiled by a computer.

Sr is loaded on a single filament, and calibration is standardized to sample NBS 987. Standardization was conducted for each new turret. Uncertainty on the standard was typically ±0.00001. Sr samples were analyzed using five collectors in dynamic mode with $^{87}Sr/^{86}Sr$ normalized to $^{87}Sr/^{86}Sr = 0.1194$. The samples were analyzed for Sr mass 88 at a minimum intensity of 3×10^{-11} A.

Nd samples are loaded onto Re filaments on one side of triple filament assembly. Nd sample calibration was done on standard JNdi-1 for each new turret. Nd standards had typical uncertainties of ± 0.00001. Nd samples were analyzed using seven collectors, calibrated to one another using Nd mass 144 at a minimum of 5×10^{-12} A.

Petrographic Analysis of Thin Sections

In plane and cross-polarized transmitted light, ten 30 μm thin sections were described using a Nikon LABOPHOT-2 polarized optical microscope at Central Washington University. Modal percentages of minerals, such as plagioclase, clinopyroxene, and olivine were identified by visual estimations. In addition, textures of mineral phases clinopyroxene and olivine were identified using the petrographic microscope. Although textures in plagioclase were identified using transmitted plane and cross-polarized light, they were described in detail using Nomarski Differential Interference Contrast.

Plagioclase Textural Analysis

Nomarski Differential Interference Contrast (NDIC) is used to document differences in surface relief in plagioclase, allowing for textural identification and interpretation. This technique uses a standard petrographic microscope, Nomarski prism (beam splitting double-crystal prism), and reflected light (Streck et al., 2008). To view surface relief, a 100 μm thick section is etched by submersing it into concentrated hydrofluoroboric (HBF$_4$) acid for 20-22 seconds allowing calcium in plagioclase to preferentially dissolve producing the microtopography imaged by NDIC. Preparation of thick sections and NDIC analysis were done at Central Washington University.

Plagioclase Major and Trace Element Analysis

For each sample, three to four crystals of each textural type were analyzed for major and trace elements using an electron microprobe. Electron microprobe is an x-ray machine in which electrons emitted from a hot-filament source are accelerated electrostatically, and then focused an electromagnetic lens to an extremely small point (5 μm) on the surface of a sample. Characteristic X-rays are emitted from the sample giving unique wavelengths for each element. The intensities of X-ray production are detected and measured, and then compared to standard and matrix corrections. Microprobe data were collected at University of California Santa Barbara, using a fully automated Cameca SX-100 fitted with 5 wavelength spectrometers and a PGT C-ray

energy dispersive detector. Running conditions for plagioclase included an electron

beam current of 20 nA, an accelerating potential of 15 to 20 kV, 10 to 90 seconds count

time (element dependent) and a beam spot size of 3 to 5 microns. Detection limits for

given elements can be found in the Electronic Appendix E, raw microprobe data. The

probe computer runs 'Probe for Windows' analytical software (Kremser, 2006). Choices

of analysis points in the core to rim traverses of plagioclase were based on textural

boundaries such as dissolution rims or transitions from oscillatory zones to sieve or

patchy zones.

<div align="center">In Situ Plagioclase Sr Isotope Analysis</div>

In situ isotope analyses were performed using WSU's laser ablation

multicollector inductively coupled plasma mass spectrometer (LA-MC-ICPMS). The

LA-MC-ICPMS at WSU is a combination of a New Wave[TM] UP213 nm Nd:YAG Laser

Ablation System coupled with a double focusing Thermo-Finnigan Neptune[TM] MC-

ICPMS equipped with 9 Faraday collectors and 10^{-11} Ω resistors (Ramos et al., 2004).

Laser troughs of 80 X 600 μm were used to maximize Sr signals, while minimizing

depth of laser pit. Typical trough depth is 50 to 70 μm. Helium gas is used to carry a

sample through the laser ablation sample cell, and mixes with argon before the sample

is introduced into the plasma. Typical results for $^{87}Sr/^{86}Sr$ yield reproducibility of

<0.00005. Sr masses measured on LA-MC-ICPMS are $^{83-88}Sr$. Interferences are Rb and

Kr, which are corrected in data processing. Choice of analysis location was made based

on results of electron microprobe work; specifically, regions that showed large changes in An content were targeted for analysis to document a record of potential open system processes. In addition, only crystals larger than 600 microns could be analyzed.

MELTS Modeling

Models were generated using the thermodynamic phase equilibria program MELTS (Ghiorso and Sack, 1995) to investigate constraints on melt and mineral formation as a result of fractional crystallization. Sixty simulations were run with varying initial and final pressure and temperature, starting compositions, water content, and oxygen fugacity. MELTS input included observed whole rock data from primitive samples on Alicudi (ALI10-05, MgO wt. % of 6.63) and Filicudi (FIL10-22, MgO wt. % of 5.83) (Harris, pers. communication). Polybaric and isobaric conditions were employed; isobaric pressures ranged from 6 kbar-2 kbar, whereas polybaric simulations started with an initial pressure of 2 kbar and ended at 10 bar. All starting temperatures were liquidus temperatures specified by MELTS based on starting composition. For the parental compositions employed, the initial temperature was 1500° C; the final temperatures varied from 900-1000° C. Water content ranged from 1-4 wt. %, and the oxygen fugacity buffers used were nickel/nickel/oxide (NNO), quartz/fayalite/magnetite (QFM), and hematite/magnetite (HM). Best-fit MELTS runs were determined by comparison to observed whole rock data from Alicudi. As described in the results and interpretations sections, misfits between model and observed Al_2O_3 and MgO (wt. %)

suggested processes not modeled by MELTS. As a consequence, plagioclase and

olivine addition of 5, 10, and 15 wt. % were applied to best fit models to simulate

assimilation of a gabbroic component. Plagioclase composition applied in models was

taken from Alicudi's most primitive sample (ALI10-05). The olivine composition used

in models was taken from sample St179 (Peccerillo and Wu, 1991). Plagioclase and

olivine compositions can be found in Table 2.

TABLE 2. RUN 52, BEST FIT MELTS RESULTS

Observed Data				
Element Oxide	Parental Magma Alicudi	* Parental Magma Filicudi	Plagioclase Composition	Olivine Composition
SiO_2	51.37	51.04	49.26	38.58
TiO_2	0.79	0.70	0.04	-
Al_2O_3	16.88	19.07	30.59	-
Fe total	8.64	8.27	0.67	21.54
MnO	0.17	0.16	0.01	0.4
MgO	6.63	5.38	0.17	40.06
CaO	11.81	11.44	14.34	0.29
Na_2O	2.46	2.48	3.12	-
K_2O	0.94	1.26	0.18	-
P_2O_5	0.32	0.19	-	-

Melts Parameters	
H_2O wt. %	3%
Initial Temp	1500 C
Final Temp	1000 C
dT	1 C
P Initial	2 kbar
P Final	10 bar
dP	20
dP/dT	20
fO2	HM
Liquidus	1210

*Parental Magma Filicudi gave best fit for MELTS runs when compared to observed data from Alicudi.

CHAPTER IV

RESULTS

Whole Rock Major and Trace Element and Sr and Nd Isotope Data

For the purpose of consistency, samples will be arranged by eruption stages,

which are based on the work of Peccerillo et al. (2004) and Bonelli et al. (2004). Stage 1

basalts and basaltic andesites are represented by samples ALI10-7, 8, 9, and 10; stage 2

basalts and basaltic andesites encompass ALI10-4, 5, 11, 13, and 14; stage 3 andesites

are comprised of samples ALI10-1, 2, 3, 15, and 17. ALI10-6 is a dike of unknown

absolute age that cross cuts ALI10-7. ALI10-12 represents small lava domes erupted

concurrently with stage 3 (Table 1). All oxides abundances are presented in weight %.

Major Oxides

Samples in this study range in composition from basalts to andesites (51.26-

58.72) (Figure 4). SiO_2 in stages 1 and 2 have similar ranges (51.26-55.36, stage 2

51.37-54.61) and are dominated by basalts and basaltic andesites, whereas stage 3 is

characterized by higher SiO_2 samples (57.02-58.72) and includes andesites and

trachyandesites (Table 3). FeO, MgO, CaO (Figure 5a, c, and d) and MnO are

negatively correlated with SiO_2. Na_2O and K_2O (Figure 5e and f) are positively

correlated with SiO_2. Al_2O_3 (Figure 5b) and P_2O_5 are generally positively correlated

with SiO_2 but scatter between ~51 and 55 SiO_2. Alicudi whole rock data will be

TABLE 3. WHOLE ROCK MAJOR AND TRACE ELEMENT DATA

Sample	ALI10-07	ALI10-08	ALI10-09	ALI10-10	ALI10-04
Stage	1	1	1	1	2
SiO_2	55.36	51.26	55.13	54.48	52.00
TiO_2	0.64	0.67	0.77	0.71	0.74
Al_2O_3	16.95	14.17	18.08	16.39	16.08
FeO*	6.83	8.68	6.76	7.35	8.51
MnO	0.13	0.17	0.14	0.15	0.16
MgO	5.88	9.80	4.44	6.14	7.37
CaO	9.55	11.83	8.67	10.24	11.70
Na_2O	3.01	2.19	3.29	2.87	2.20
K_2O	1.38	0.93	2.36	1.41	0.98
P_2O_5	0.26	0.29	0.37	0.25	0.26
Ni	49	118	31	42	8
Cr	142	472	51	163	9
Sc	29	41	25	32	18
V	200	249	212	212	162
Ba	554	366	639	379	827
Rb	34	24	66	39	61
Sr	848	790	676	596	712
Zr	108	74	131	97	157
Y	16.63	18.78	24.51	19.97	18.59
Nb	12	12	15	11	30
Th	8.63	5.02	8.39	5.45	3.23
Hf	2.43	1.75	2.99	2.37	1.7
U	2.24	1.43	2.40	1.54	0.95
Pb	4.30	4.00	4.20	4.92	3.66
Cs	0.65	0.48	0.72	0.78	0.42
La	40.1	32.0	39.7	26.4	20.4
Ce	69.4	55.8	71.6	45.3	37.2
Pr	7.4	6.6	7.9	5.2	4.7
Nd	26.6	24.7	29.6	20.0	18.7
Sm	4.6	4.8	5.9	4.1	4.1
Eu	1.38	1.41	1.69	1.25	1.28
Gd	3.7	4.1	5.2	3.8	3.8
Tb	0.56	0.63	0.81	0.62	0.61
Dy	3.3	3.7	4.8	3.8	3.7
Ho	0.66	0.74	0.94	0.77	0.74
Er	1.80	2.00	2.55	2.12	1.97
Tm	0.26	0.29	0.37	0.31	0.28
Yb	1.7	1.8	2.4	2.0	1.7
Lu	0.27	0.29	0.37	0.32	0.27
La/Yb	24.05	17.73	16.76	13.11	11.76

TABLE 3. (CONT.)

Sample	ALI10-05	ALI10-11	ALI10-13	ALI10-14	ALI10-01
Stage	2	2	2	2	3
SiO$_2$	51.37	54.61	54.50	53.60	57.35
TiO$_2$	0.79	0.71	0.74	0.77	0.69
Al$_2$O$_3$	16.88	16.54	16.07	16.18	17.73
FeO*	8.64	7.30	7.56	7.63	6.45
MnO	0.16	0.15	0.15	0.15	0.14
MgO	6.63	6.02	6.31	6.78	4.07
CaO	11.81	10.11	9.85	10.29	7.44
Na$_2$O	2.46	2.91	3.02	2.88	3.58
K$_2$O	0.94	1.40	1.49	1.42	2.16
P$_2$O$_5$	0.32	0.25	0.31	0.29	0.39
Ni	56	43	54	61	24
Cr	166	154	216	231	58
Sc	40	30	32	32	22
V	278	216	235	243	188
Ba	263	390	500	468	665
Rb	26	39	35	32	62
Sr	646	606	625	630	667
Zr	68	100	98	92	136
Y	19.48	19.60	19.58	19.98	20.54
Nb	8	11	13	12	19
Th	4.34	5.48	6.79	6.17	10.57
Hf	1.81	2.37	2.29	2.17	3.01
U	1.20	1.59	1.87	1.73	2.98
Pb	2.58	3.78	3.66	4.31	6.93
Cs	0.47	0.52	0.45	0.35	1.18
La	27.9	26.4	32.5	30.1	47.2
Ce	48.6	45.5	54.9	51.5	80.9
Pr	5.7	5.3	6.3	6.0	8.3
Nd	21.6	19.9	27.9	22.5	28.9
Sm	4.4	4.0	4.6	4.6	5.1
Eu	1.37	1.24	1.40	1.41	1.52
Gd	4.1	3.8	4.1	4.1	4.3
Tb	0.64	0.61	0.64	0.64	0.67
Dy	3.8	3.7	3.8	3.8	4.0
Ho	0.77	0.76	0.77	0.77	0.80
Er	2.05	2.11	2.10	2.10	2.20
Tm	0.29	0.31	0.31	0.31	0.33
Yb	1.9	2.0	1.9	1.9	2.1
Lu	0.29	0.32	0.31	0.31	0.34
La/Yb	14.93	13.39	16.76	15.47	22.32

TABLE 3. (CONT.)

Sample	ALI10-02	ALI10-03	ALI10-15	ALI10-16	ALI10-17
Stage	3	3	3	3	3
SiO_2	58.38	58.72	58.65	58.19	57.69
TiO_2	0.80	0.79	0.79	0.68	0.69
Al_2O_3	18.58	18.56	18.60	17.59	17.60
FeO*	6.00	5.76	5.99	6.22	6.34
MnO	0.12	0.11	0.12	0.14	0.14
MgO	2.72	2.48	2.55	3.72	3.90
CaO	6.49	6.52	6.32	6.99	7.37
Na_2O	4.05	4.17	4.09	3.73	3.67
K_2O	2.43	2.46	2.46	2.34	2.21
P_2O_5	0.43	0.42	0.43	0.40	0.39
Ni	10	8	10	21	22
Cr	9	9	7	46	53
Sc	17	18	18	19	22
V	172	162	173	176	185
Ba	809	827	820	726	685
Rb	60	61	65	66	64
Sr	694	712	691	695	691
Zr	153	157	155	144	139
Y	23.72	24.22	25.27	20.75	20.36
Nb	30	30	30	20	20
Th	10.39	10.66	10.45	11.73	10.88
Hf	3.55	3.63	3.59	3.18	3.04
U	3.31	3.39	3.25	3.28	3.09
Pb	6.30	5.65	6.36	6.97	6.06
Cs	0.59	0.55	1.05	1.38	1.26
La	47.5	49.3	50.4	51.9	48.2
Ce	83.0	85.5	87.5	86.8	81.2
Pr	8.9	9.2	9.4	8.9	8.3
Nd	31.7	32.5	33.4	30.3	28.9
Sm	5.7	5.9	6.0	5.2	5.0
Eu	1.65	1.66	1.69	1.54	1.51
Gd	5.0	5.0	5.2	4.3	4.2
Tb	0.76	0.78	0.80	0.67	0.65
Dy	4.6	4.6	4.7	4.0	3.9
Ho	0.93	0.94	0.96	0.79	0.79
Er	2.59	2.61	2.67	2.22	2.17
Tm	0.38	0.39	0.39	0.33	0.33
Yb	2.4	2.5	2.5	2.1	2.1
Lu	0.39	0.40	0.40	0.35	0.34
La/Yb	19.47	20.07	20.07	24.23	23.07

TABLE 3. (CONT.)

Sample	ALI10-12	ALI10-06	LOD*
Stage	Dome	Dike	2-sigma
SiO$_2$	57.02	51.51	0.19
TiO$_2$	0.69	0.75	0.012
Al$_2$O$_3$	17.74	16.09	0.082
FeO*	6.44	8.48	0.18
MnO	0.14	0.16	0.002
MgO	4.14	7.04	0.073
CaO	7.66	12.07	0.043
Na$_2$O	3.65	2.56	0.036
K$_2$O	2.13	1.09	0.015
P$_2$O$_5$	0.38	0.25	0.0003
Ni	24	67	3.5
Cr	57	234	3.0
Sc	22	35	1.6
V	191	260	5.0
Ba	633	287	11.7
Rb	61	27	1.7
Sr	694	650	4.6
Zr	134	75	3.9
Y	20.45	19.27	0.009
Nb	18	9	1.20
Th	9.99	3.41	0.013
Hf	2.90	1.80	0.02
U	2.86	0.95	0.014
Pb	4.35	3.17	0.07
Cs	0.68	0.20	0.02
La	45.4	20.9	0.011
Ce	76.9	37.8	0.009
Pr	8.0	4.6	0.009
Nd	23.3	18.2	0.04
Sm	4.9	3.9	0.03
Eu	1.47	1.23	0.009
Gd	4.2	3.8	0.03
Tb	0.66	0.61	0.006
Dy	3.9	3.7	0.018
Ho	0.80	0.76	0.006
Er	2.18	2.07	0.02
Tm	0.32	0.30	0.007
Yb	2.1	1.8	0.02
Lu	0.33	0.30	0.006
La/Yb	22.00	11.31	-

*Major elements in wt% normalized to 100%; trace elements in p.p.m. Major elements and Ni, Cr, Sc, V, Ba, Rb, Sr, Zr, Nb analyses done by X-ray fluorescence (XRF); all others done by inductively coupled plasma mass spectrometry (ICP-MS). Samples are arranged by eruption stage. LOD- Limit of Detection.

compared with Filicudi whole rock data (Harris, 2012) and Salina whole rock data

(Mayfield, 2012).
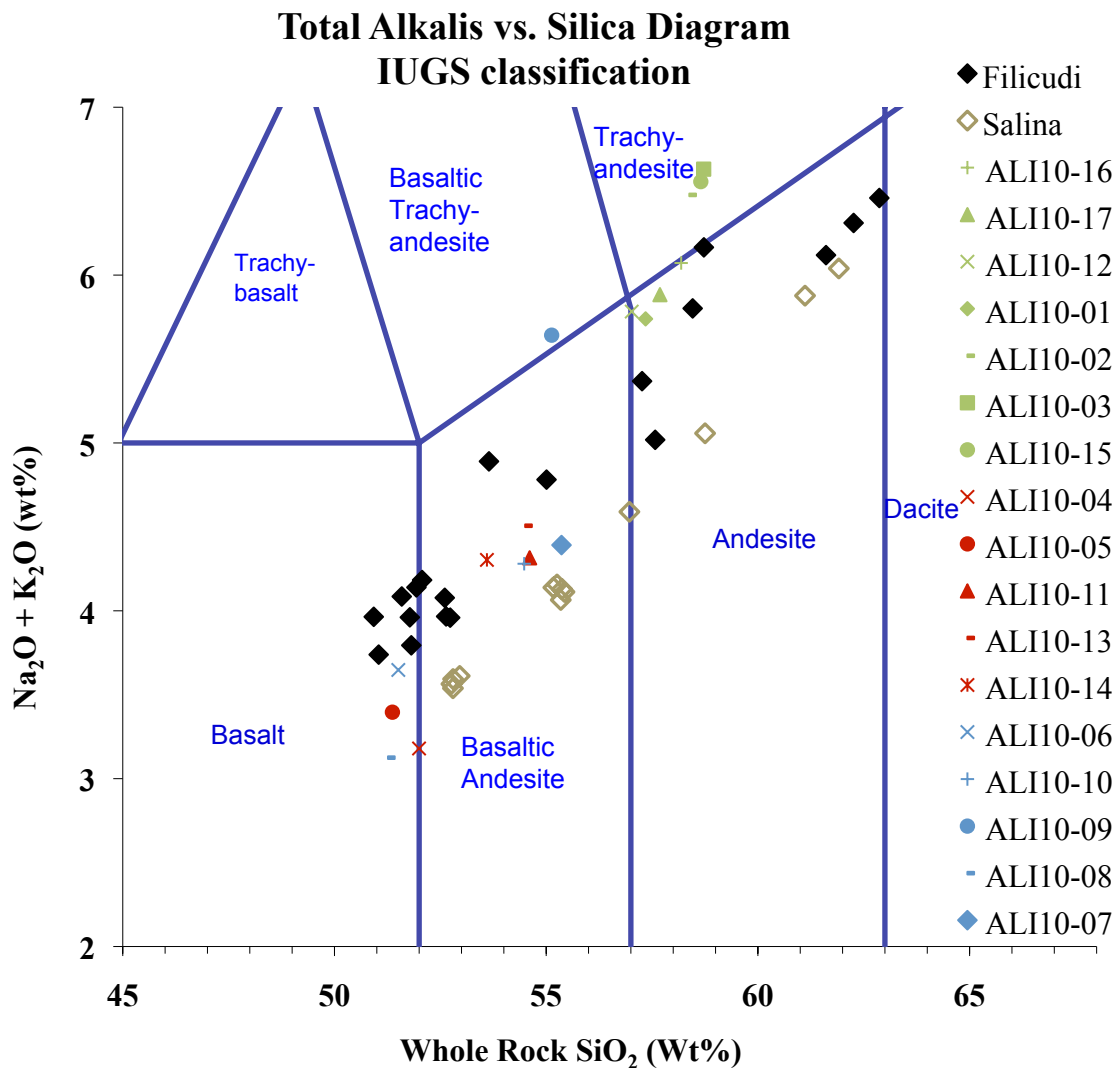
Figure 4. IUGS Volcanic Rock Classification (LeBas et al., 1986). Stage 1 represented by blue points; Stage 2 represented by red points; Stage 3 represented by green points. Samples arranged in stratigraphic order based on eruption time. Surrounding islands Salina (open brown diamonds) and Filicudi (open black diamonds) are shown for comparison.

FeO in Alicudi samples with ~53 SiO_2 or greater from all stages is less abundant

than that in samples from Filicudi (Harris, pers. communication) and Salina (Mayfield,

pers. communication), whereas MgO is higher for stages 1 and 2 compared to rocks of similar SiO_2 (Figure 5a and c). When compared to Filicudi and Salina, stage 3 has higher concentrations of Na_2O (Figure 5e). Al_2O_3 in stages 1 and 2 is lower than that of samples from Filicudi and Salina (Figure 5b), whereas Al_2O_3 in stage 3 andesites is similar to rocks of similar SiO_2 from Filicudi and Salina.

Trace Elements

Whole rock compatible trace element data (Figure 6) show that Sc (Figure 6c) and V decrease with increasing with SiO_2. Ni and Cr are generally negatively correlated with SiO_2 but show scatter between 51-55 SiO_2 wt. % (Figure 6b and d). Sr shows no correlation (Figure 6a), but of particular note is the abundances of Sr in stage 3 andesites are equal to or greater than more mafic rocks of stages 1 and 2.

Alicudi exhibits higher abundances of Ni and Cr than Filicudi and Salina (Figure 6b and d). Stages 1 and 2 have similar abundances of Sc when compared to Filicudi and Salina over a range of 50-55 SiO_2 wt. %. However, stage 3 has lower abundances of Sc than Filicudi and Salina (Figure 6c). Sr values show scatter for Alicudi, Filicudi, and Salina. However, Alicudi has the highest range in Sr concentrations when compared to Filicudi and Salina. Whole rock trace element trends from Alicudi show Ba, Zr, Nb (Figure 7a, c, and e), Ta, and Hf increase with increasing SiO_2 and exhibit systematic trends. Rb, U, Th, Pb, and Cs concentrations generally increase with SiO_2, however, scatter is observed from 51-56 SiO_2.

Rare earth elements (REEs), such as La, Lu (Figure 8a and d), Yb, and Ce increase with increasing SiO_2 and have the most systematic trends. Nd, Eu (Figure 8b
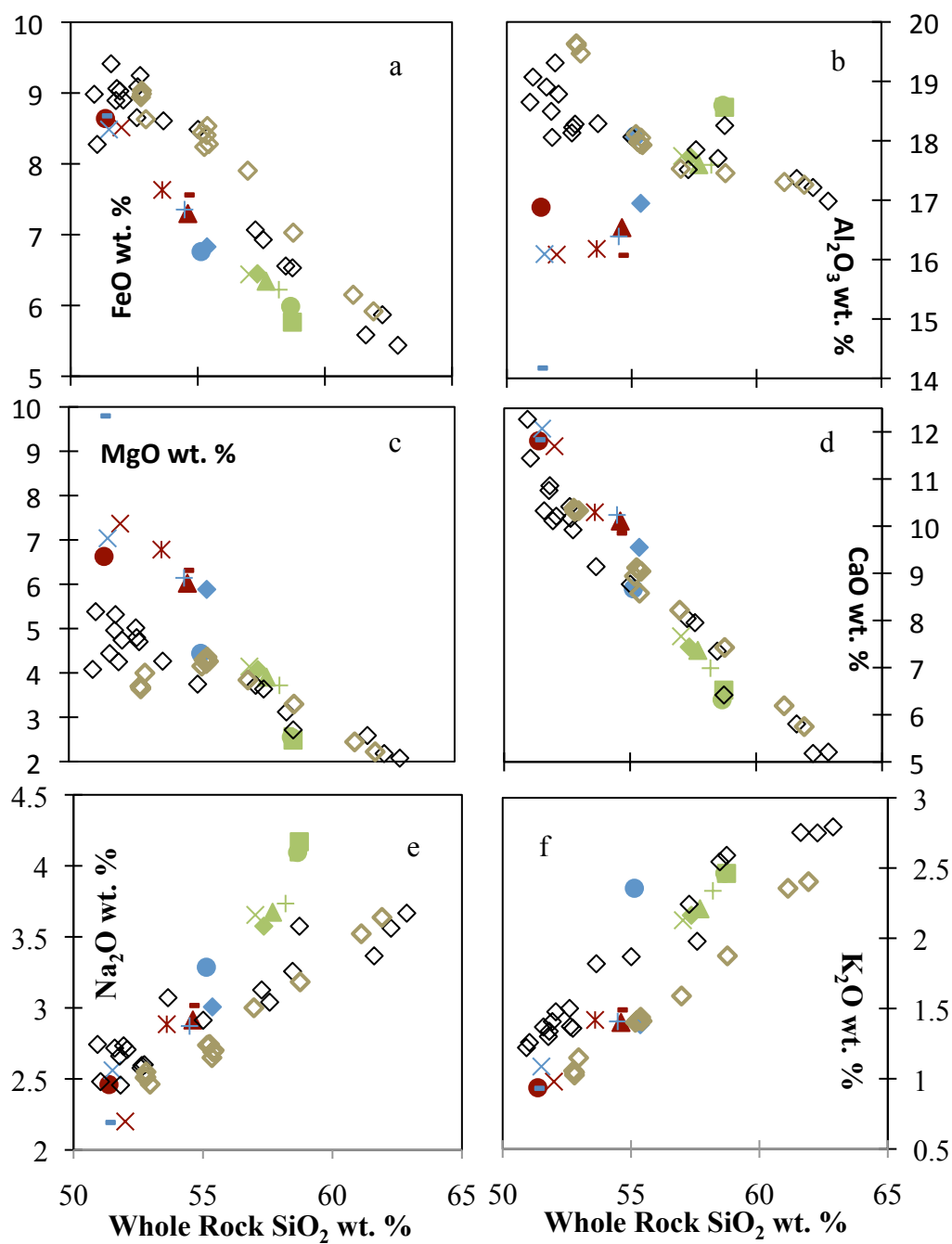
Figure 5. Whole rock SiO_2 wt. % plotted against whole rock (a) FeO, (b) Al_2O_3, (c) MgO, (d) CaO, (e) Na_2O, and (f) K_2O wt. %. Blue symbols represent Stage 1; red symbols represent Stage 2; green symbols represent Stage 3; open black diamonds represent Filicudi, open brown diamonds represent Salina; see Figure 4 for Alicudi sample symbols.
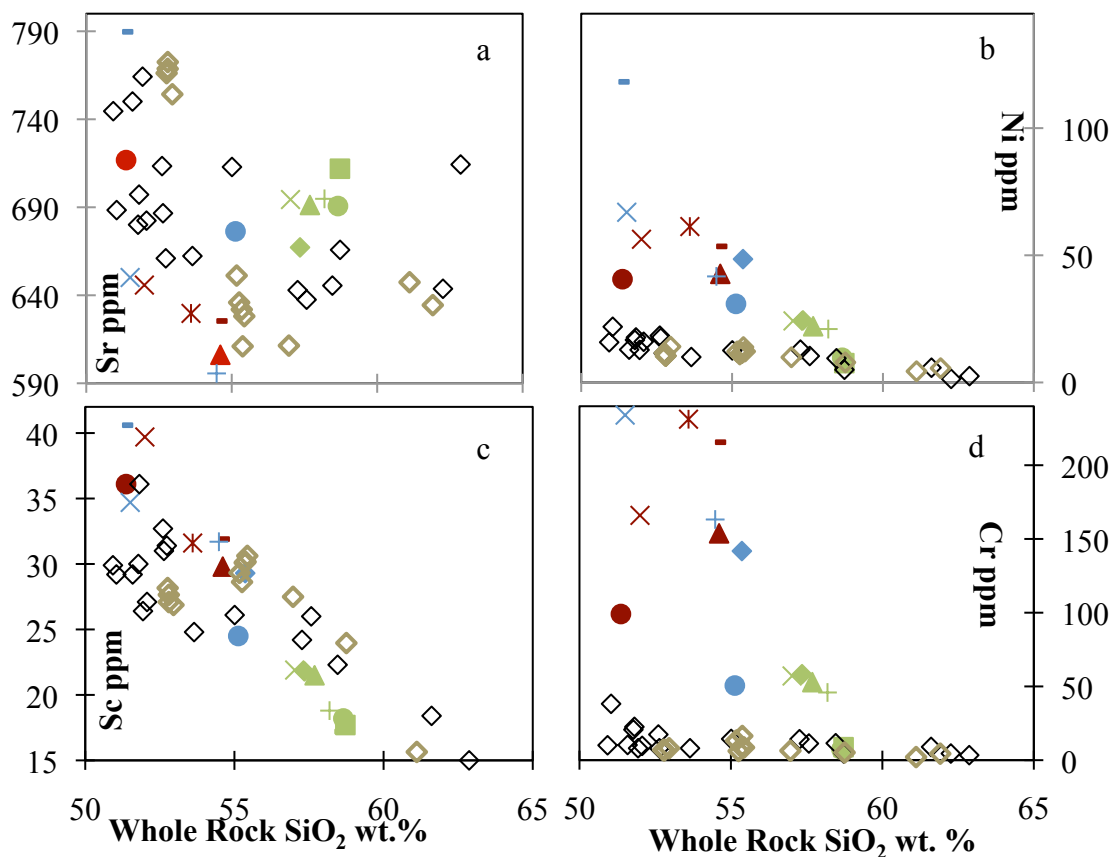
Figure 6. Whole rock SiO$_2$ wt. % plotted against whole rock compatible trace elements (a) Sr, (b) Ni, (c) Sc, and (d) Cr ppm variation diagrams for lavas on Alicudi. Symbols are same as Figure 4.

and c), and Sm increase with increasing SiO$_2$, except there is scatter between 52-55 SiO$_2$ wt.%. Y data show an increase with increasing SiO$_2$; however there is scatter between 51-58 SiO$_2$ wt.%. Stage 1 is least enriched in LREE, with the largest (La/Yb)$_N$ range- 11.3-17.7. (La/Yb)$_N$. Stage 2 ranges from 11.8-16.8. Stage 3 is the most enriched in LREE and has the smallest range in (La/Yb)$_N$ - 19.5-24.2. (Figure 9).

Alicudi andesites are more enriched in Ba, Zr, Th, U, Nb, and La, than Filicudi and Salina over the same range in SiO$_2$ (Figure 7 and 8). Pb concentrations are lower in Alicudi samples compared to samples from Filicudi and Salina.

Figure 7. Whole rock SiO₂ wt. % plotted against whole rock incompatible trace elements (a) Ba, (b) Rb, (c) Zr, (d) Th, (e) Nb, and (f) U ppm variation diagrams for lavas on Alicudi. Pink lines represent fractionation trends, with a distribution coefficient of 0, and 40% remaining liquid. Symbols are same as Figure 4.
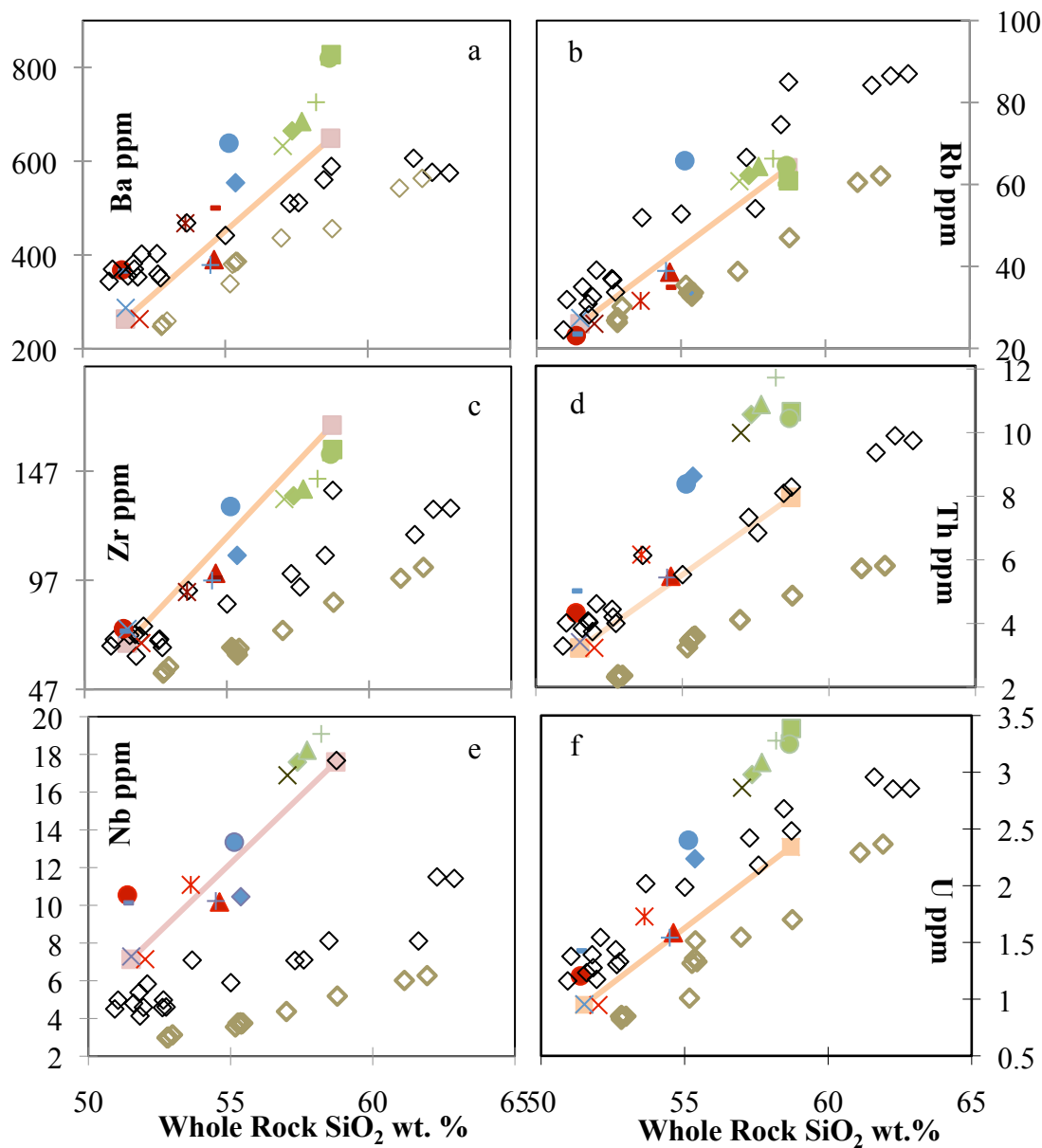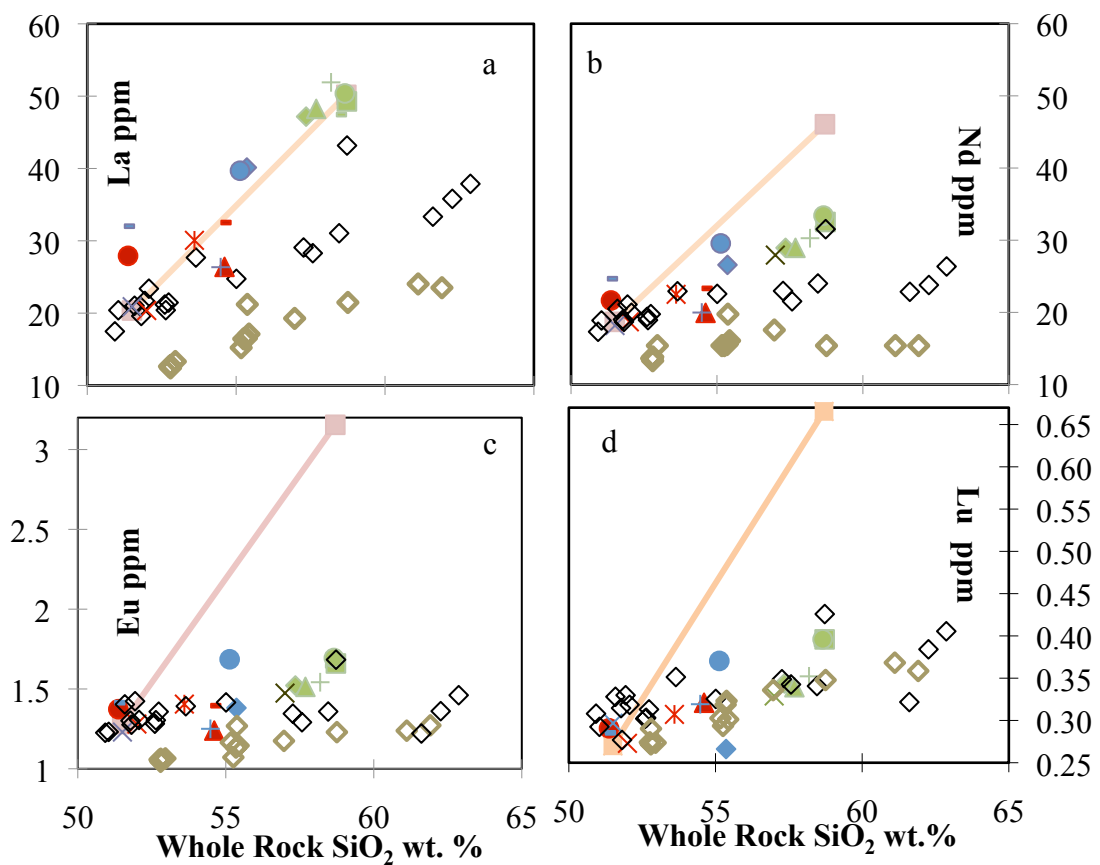
Figure 8. Whole rock SiO₂ wt. % plotted against whole rock incompatible REE elements (a) Nd, (b) La, (c) Lu, and (d) Yb ppm variation diagrams for lavas on Alicudi. Pink lines represent fractionation trend, with a distribution coefficient of 0, and 40% remaining liquid. Symbols are same as Figure 4.
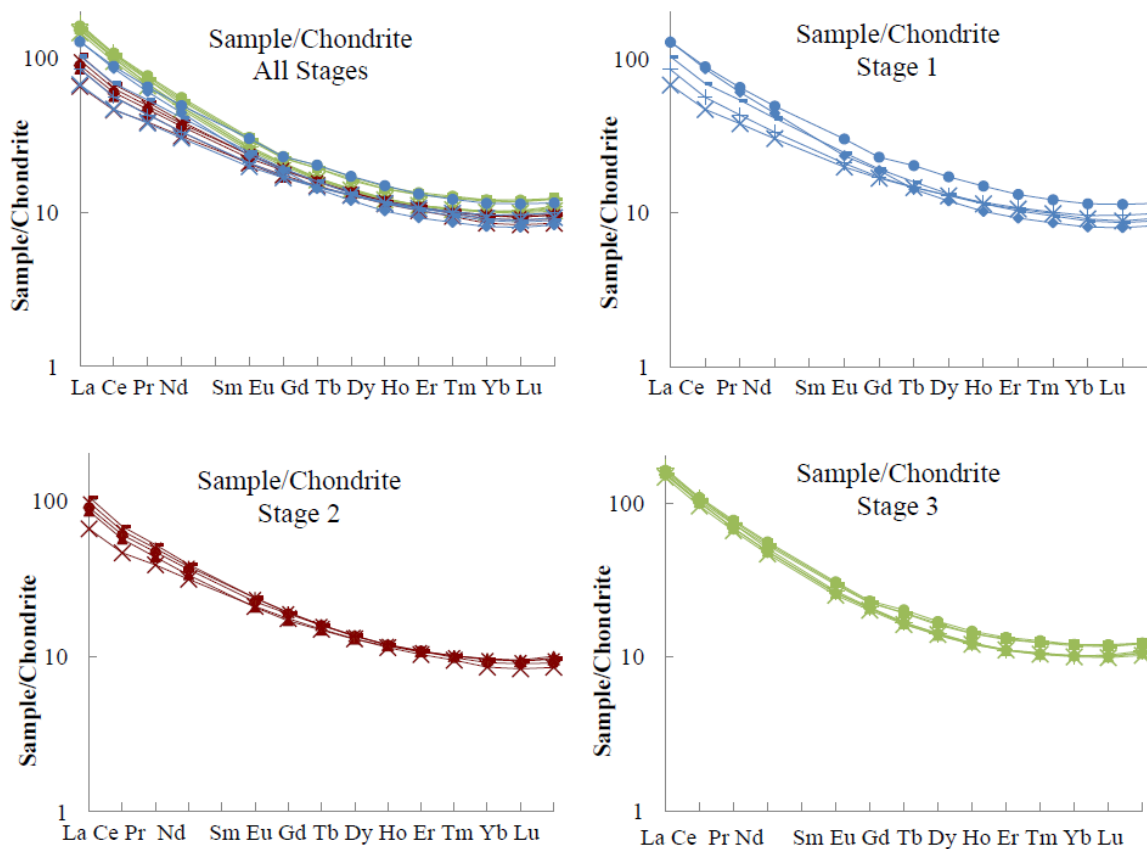
Figure 9. Chondrite-normalized REE diagrams for Alicudi Island. Normalization constants are from Boynton (1984). (a) All stages; stage 1- blue symbols, stage 2- red symbols, and stage 3- green symbols (b) Stage 1 (c) Stage 2. (d) Stage 3. For individual sample symbols, see Figure 4.

Sr and Nd Isotopes

The $^{87}Sr/^{86}Sr$ range, from 0.70315-0.70395 (Table 4), shown in Figure 10 includes samples from this study and that of Peccerillo (2004); the ranges for the two studies are similar. Roughly 65 % of the samples have $^{87}Sr/^{86}Sr$ in the range 0.70345-0.70365. From 54-60 wt.% SiO_2, $^{87}Sr/^{86}Sr$ decreases with increasing SiO_2; ALI10-07 is

TABLE 4. WHOLE ROCK SR AND ND ISOTOPE DATA FOR ALICUDI

Sample	$^{87}Sr/^{86}Sr$	Error	$^{143}Nd/^{144}Nd$	Error
Stage 1				
ALI10-7	0.70316	$11 * 10^{-6}$	0.512925	$12 * 10^{-6}$
ALI10-8	0.70376	$11 * 10^{-6}$	0.512910	$13 * 10^{-6}$
ALI10-9	0.70382	$11 * 10^{-6}$	0.512852	$13 * 10^{-6}$
ALI10-10	0.70361	$11 * 10^{-6}$	0.512879	$15 * 10^{-6}$
ALI10-7 P22C	0.70336	$34 * 10^{-6}$	-	-
ALI10-8 GM	0.70380	$19 * 10^{-6}$	-	-
Stage 2				
ALI10-4	0.70364	$11 * 10^{-6}$	0.51291	$13 * 10^{-6}$
ALI10-5	0.70355	$10 * 10^{-6}$	0.51287	$11 * 10^{-6}$
ALI10-11	0.70360	$13 * 10^{-6}$	0.51287	$11 * 10^{-6}$
ALI10-13	0.70369	$13 * 10^{-6}$	0.51287	$19 * 10^{-6}$
ALI10-14	0.70368	$13 * 10^{-6}$	0.51295	$13 * 10^{-6}$
ALI10-5 GM	0.70358	$38 * 10^{-6}$	-	-
ALI10-11 GM2	0.70370	$42 * 10^{-6}$	-	-
ALI10-11 P5	0.70373	$56 * 10^{-6}$	-	-
Stage 3				
ALI10-1	0.70361	$14 * 10^{-6}$	0.51290	$9 * 10^{-6}$
ALI10-2	0.70334	$17 * 10^{-6}$	0.51291	$8 * 10^{-6}$
ALI10-3	0.70346	$10 * 10^{-6}$	0.51293	$12 * 10^{-6}$
ALI10-15	0.70349	$13 * 10^{-6}$	0.51292	$10 * 10^{-6}$
ALI10-15	0.70350	$17 * 10^{-6}$		
ALI10-16	0.70354	$10 * 10^{-6}$	0.51294	$12 * 10^{-6}$
ALI10-17	0.70359	$13 * 10^{-6}$	0.51295	$12 * 10^{-6}$
ALI10-17	0.70362	$13 * 10^{-6}$		
Dome				
ALI10-12	0.70355	$14 * 10^{-6}$	0.51289	$9 * 10^{-6}$
Dike				
ALI10-6	0.70391	$13 * 10^{-6}$	0.51283	$10 * 10^{-6}$

* GM = Groundmass analysis,
** P#C = Single plagioclase TIMS analysis

the outlier, plotting at ~0.70316. Over the SiO_2 range of 50-54 wt.%, $^{87}Sr/^{86}Sr$ does not

systematically correlate with SiO_2 and the range 0.70334-0.70382.
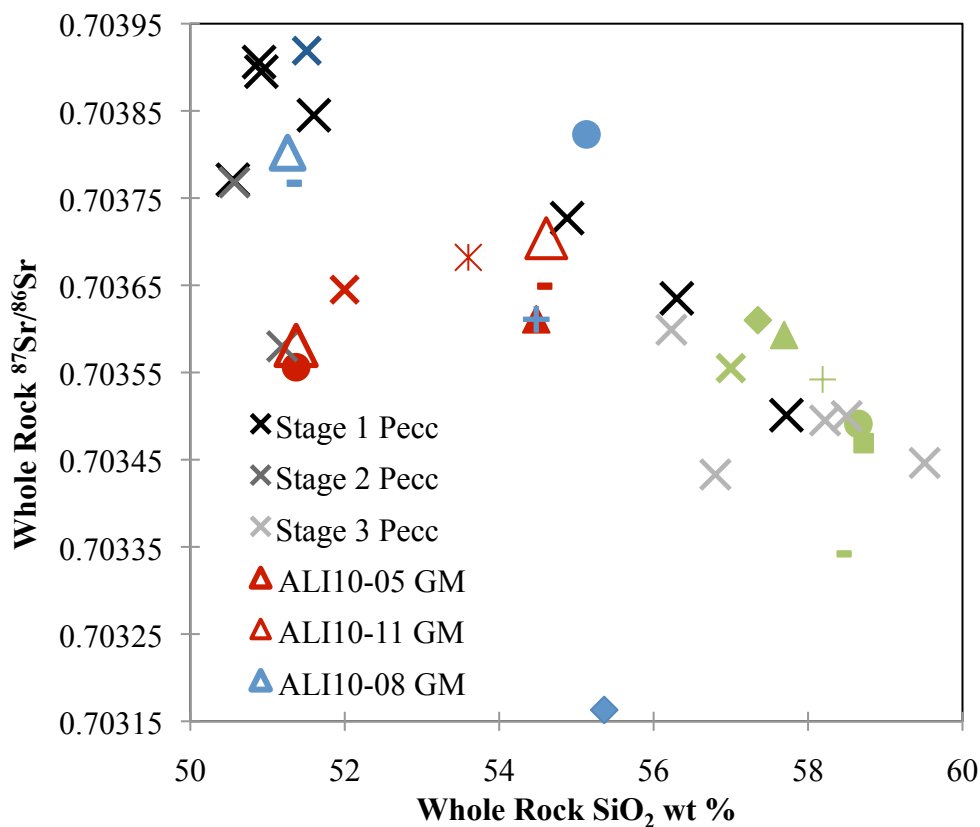
Figure 10. Whole rock SiO$_2$ wt. % plotted against whole rock ^{87}Sr/^{86}Sr. Stage 1- blue symbols, stage 2- red symbols, stage 3- green symbols. Open enlarged triangles represent groundmass, which plot within error of whole rock data. Black, dark grey, and light grey x symbols are from Peccirillo et al. (2004). Reproducibility for TIMS analysis is ±0.00001, smaller than symbol size. See Figure 4 for sample symbols.

Stages 1 and 2 ^{87}Sr/^{86}Sr (stage 1- 0.70316-0.70391; stage 2- 0.70361-0.70368) are generally more radiogenic than those of stage 3 (0.70334-0.70362). Stage 3 has the smallest range of radiogenic Sr. Available groundmass ^{87}Sr/^{86}Sr plots within error of whole rock values (Figure 10).

Nd isotopes range from 0.51285-0.51295 (Table 4). A systematic trend between Sr and Nd isotopes is lacking, and there is no simple relationship between stage of

eruption and Nd isotope value. Stages 1 and 2 have generally lower and more variable

$^{143}Nd/^{144}Nd$ (0.51285-0.51293; 0.51287-0.51295) than stage 3 (0.51290-0.51250).

Alicudi has the lowest $^{87}Sr/^{86}Sr$ signature when compared to Salina, and highest

$^{143}Nd/^{144}Nd$ signature when compared to Salina (Figure 11) and Filicudi. Filicudi Nd

isotopic values range from 0.51271-0.51288, whole Sr isotopic data for Filicudi are

pending analysis.
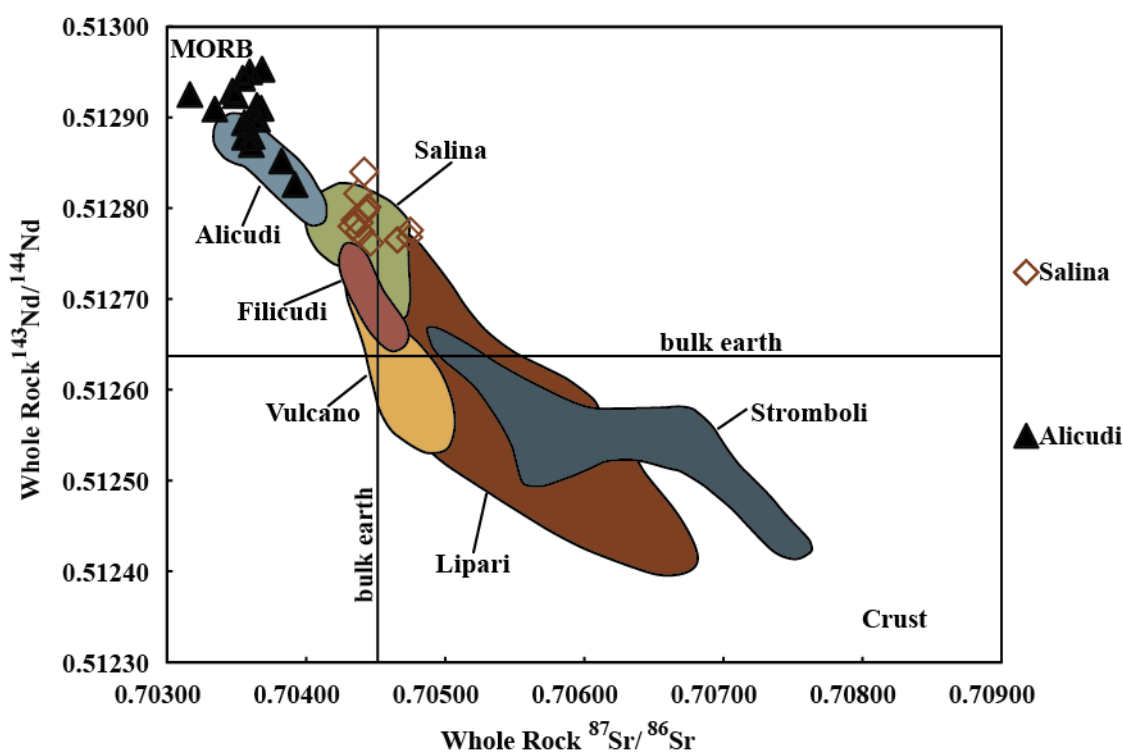
Figure 11. Whole rock $^{87}Sr/^{86}Sr$ plotted against whole rock $^{143}Nd/^{144}Nd$. Alicudi
samples are labeled as closed black triangles, Salina- open brown diamonds.
Reproducibility on $^{87}Sr/^{86}Sr$ is ±0.00001; reproducibility on $^{143}Nd/^{144}Nd$ is ±0.00001.
Also labeled on this figure are $^{87}Sr/^{86}Sr$ and $^{143}Nd/^{144}Nd$ ranges for other islands in the
Aeolian Arc (Filicudi- red polygon, Vulcano- tan polygon, Lipari-brown polygon, and
Stromboli- blue polygon). (Modified from Gertisser and Keller, 2000).

Petrographic Descriptions

Samples from ten lithologic units on Alicudi were cut into thin sections and petrographically analyzed using a standard petrographic microscope (Table 5). The ten representative samples are ALI10-01, 03, 04, 05, 07, 08, 09, 10, 11, 12, and 17. These samples were also cut into thick sections, and plagioclase was analyzed for textural, major and trace, and Sr isotopic data, described in sections below.

Stage 1- Basalts and Basaltic Andesites

Stage 1 samples from Alicudi (ALI10-07, 08, 09, 10) are porphyritic, with phenocryst abundances of ~30-50 vol% (Figure 12). Phenocryst phases are plagioclase, clinopyroxene, and olivine. Plagioclase is the dominant phase, representing up to 60 vol% of the non-groundmass phases. Plagioclase has many complex textures and zoning that will be discussed in later sections. The next most abundant phase is clinopyroxene, which composes up to 25 vol% of the mode. Clinopyroxene shows oscillatory zoning, exhibits polysynthetic twinning, and is subhedral to euhedral. In some cases, clinopyroxene appears in glomerocrysts with plagioclase and olivine. Less than 1% clinopyroxenes have sieved cores, as seen in Figure 12. Olivine is the least abundant phenocryst phase at <10% and is subhedral to euhedral. Olivine also appears as inclusions in clinopyroxene. In samples ALI10-07 and ALI10-09, olivine phenocrysts exhibit undulatory extinction and have reactions rims of Fe-Ti oxides or iddingsite. Apatite, <1%, occurs as inclusions in plagioclase. Groundmass consists of the same phases as the phenocryst phases plus Fe-Ti oxides.

TABLE 5. PETROGRAPHY

Sample	Plag (%)	Cpx (%)	Ol (%)	Opx (%)	Hrnbld (%)	Apatite (%)	Fe-Ti Oxides (%)	Gl (%)	Rock Type
Stage 1	pl=ox>cpx>ol>gl								
ALI10-07	45	20	8	0	0	1	25	1	BA
ALI10-08	35	25	7	0	0	1	30	2	B
ALI10-09	45	15	5	3	0	1	30	1	BA
ALI10-10	60	10	7	0	0	1	20	2	BA
Stage 2	pl=ox>cpx>ol>opx								
ALI10-04	50	20	7	0	<1	1	20	2	BA
ALI10-05	45	25	7	1	0	1	20	1	B
ALI10-11	55	20	6	2	0	1	15	1	BA
Stage 3	pl=ox>cpx>opx>ol>gl								
ALI10-01	60	15	1	3	1	<1	15	5	A
ALI10-03	70	4	3	1	0	1	20	1	A
ALI10-17	65	10	<1	5	<1	1	15	4	A
Dome	pl=ox>cpx>opx>ol>gl								
ALI10-12	60	10	<1	7	<1	1	20	2	A

*plag=plagioclase, ox=oxides, cpx=clinopyroxene, ol=
olivine, gl=glass, opx= orthopyroxene, hrnbld=hornblende;
% are volume percents (modal abundances); modes are for
non-groundmass phases; B= Basalt, BA= Basaltic Andesite,
A = Andesite; Samples are arranged by eruption stage
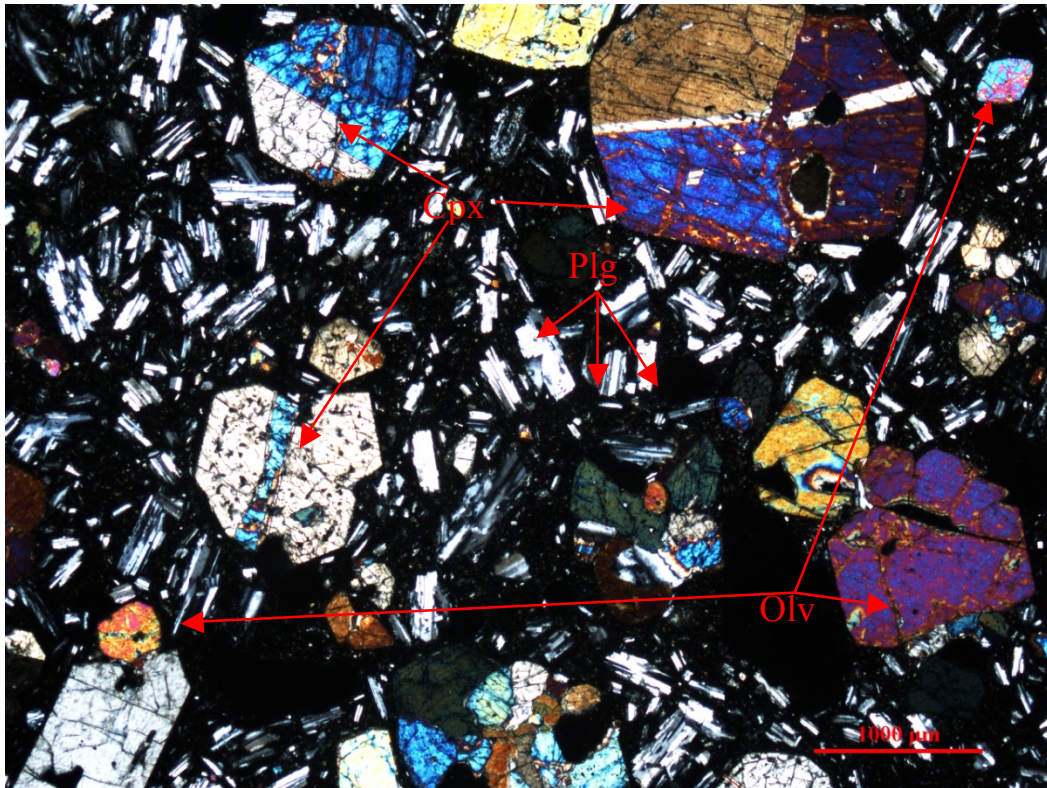
Figure 12. Cross-polar, 4x photomicrograph of basalt, ALI10-08, example of stage 1 on Alicudi. Phases present are plagioclase (plg), clinopyroxene (cpx), and olivine (olv). Groundmass exhibits same phases as phenocrysts and FeTi oxides. Red scale bar is 1000μm.

Stage 2- Basalts and Basaltic Andesites

Stage 2 basalts and basaltic andesites (ALI10-05 and ALI10-11) are similar to stage 1 rocks. Plagioclase is the dominant phase at 45-55 modal percent (Figure 13). Clinopyroxene is the next most abundant, 20-25%. Clinopyroxene has oscillatory zones, and 20% exhibit sieve textures in the core and intermediate regions of crystals. Olivine
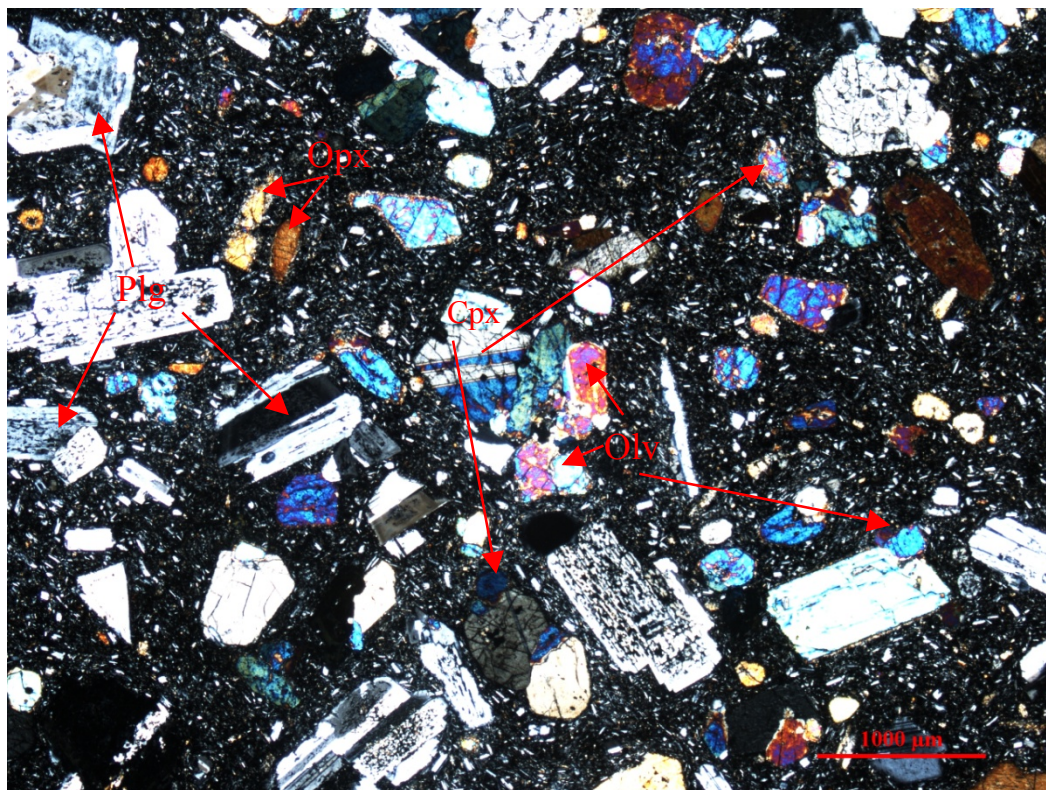
Figure 13. Cross-polar, 4x photomicrograph of basaltic andesite, ALI10-11, example of stage 2 on Alicudi. Phases present are plagioclase (plg), clinopyroxene (cpx), olivine (olv), and orthopyroxene (opx). Groundmass exhibits same phases as phenocrysts and FeTi oxides. Red scale bar is 1000μm.

exhibits extinction and has Fe-Ti oxide reaction rims; in some cases olivine has altered to iddingsite. Orthopyroxene appears with a model abundance of 1%, and amphibole has an has an abundance of 6-7% and is subhedral. Olivine exhibits Fe-Ti oxide reaction rims, or rims that have altered to iddingsite. Additionally, olivine crystals have undulatory abundance of <1%. Amphibole crystals have wide Fe-Ti oxide reaction rims of ~100μm. At less than 1%, apatite is noted as inclusions in plagioclase. Glomerocrysts of plagioclase, clinopyroxene, and olivine are present. Groundmass includes the same phases plus Fe-Ti oxides (Table 4).

Stage 3- Andesites

Plagioclase is also the most abundant phase in stage 3 (ALI10-01, 03, 12, 17)

and has a modal abundance of 60-70% (Figure 14). Plagioclase abundance is followed

by clinopyroxene, which is present at 4-15% of the modal abundance. Clinopyroxenes

are subhedral and have oscillatory zones. The abundance of orthopyroxene is 1-5%.

Olivine's abundance is up to 3%, and crystals are characterized by undulatory extinction

and reaction rims of clinopyroxene, plagioclase, and Fe-Ti oxides. In some cases,

olivine has completely altered to iddingsite. Hornblende's abundance is <1%, and

crystals exhibit reaction rims of Fe-Ti oxide (10 μm). Glomerocrysts of plagioclase and

clinopyroxene are present. Inclusions of apatite in plagioclase occur and compose 1% of

the mode. Groundmass is comprised of plagioclase, clinopyroxene, orthopyroxene,

scarce olivine, glass, and Fe-Ti oxides (Table 4).

Plagioclase Textural Types Defined by Nomarski Differential Interference Contrast

Imaging

Nomarski Differential Interference Contrast Imaging (NDIC) microscopy was

used to capture textural features in plagioclase crystals. Twelve crystals per sample

were imaged, totaling to 120 plagioclase crystals. From the crystals imaged, four main

textural types were identified: simple oscillatory, complex oscillatory, sieved/patchy

intermediate, and sieved/patchy core (Figure 15). Crystals can be characterized by more

than one textural type; however, the textural types described below are the dominant

texture within the crystal. For all plagioclase NDIC images, see Electronic Appendix C, NDIC.

Figure 14. Cross-polar, 4x photomicrograph of andesite, ALI10-01, example of stage 3 on Alicudi. Phases present are plagioclase (plg), clinopyroxene (cpx), orthopyroxene (opx), and olivine (olv). Groundmass exhibits same phases as phenocrysts and FeTi oxides. Red scale bar is 1000μm.

Figure 16 provides a schematic drawing of the textural types. Simple oscillatory-zoned plagioclase is normally zoned plagioclase with no visual and compositional irregularities in zones. Monotonous zones may accompany simple oscillatory zones. Complex oscillatory zones are normal or reversed zoned plagioclase with truncations of

zones, wavy zones, or complex patterns within oscillations. Complex oscillatory zones also exhibit dissolution rims. Sponge-like or box-like textures in the core or intermediate
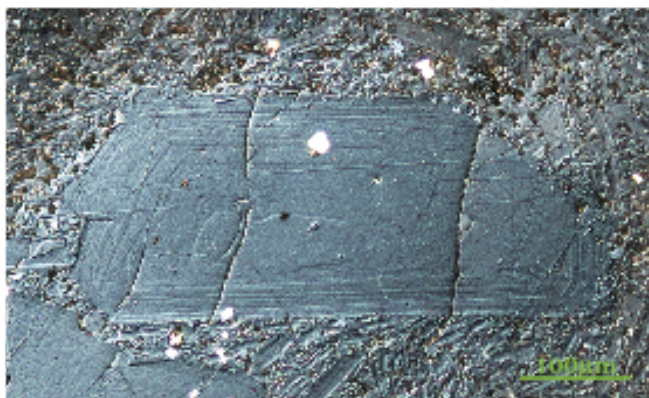
Figure 15. Examples of NDIC plagioclase images for four representative textural types found on Alicudi: (a) simple oscillatory; (b) complex oscillatory; (c) sieved intermediate; (d) patchy core.

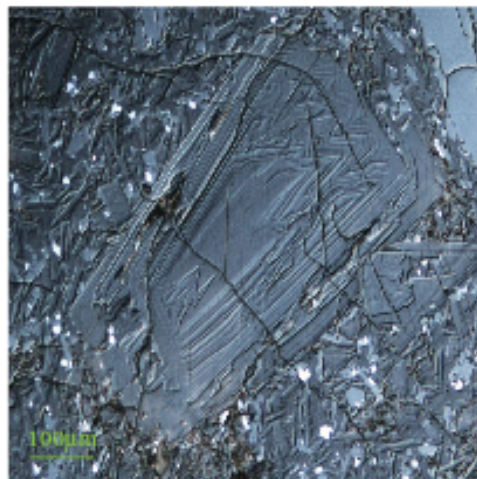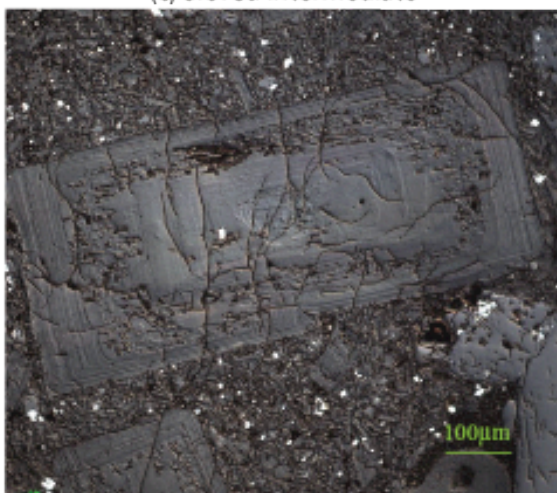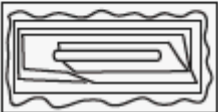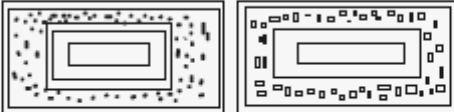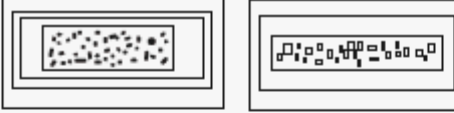| Texture Type	Schematic	Description
Simple Oscillatory		Normally zoned plagioclase with no irregularities in zones. May be accompanied by monotonous zones
Complex Oscillatory		Normal or reversed zoned plagioclase with truncations, wavy, or irregular zones
Sieved or Patchy Intermediate		Plagioclase crystals that exhibit sieved or patchy textures in intermediate areas. Textures appear sponge-like or patch-like in intermediate areas..
Sieved or Patchy Core		Plagioclase crystals that exhibit sieved or patchy textures in the core of the crystal. Also appear sponge or patch-like in crystal

Interpretation of Textures

Oscillatory zones formed by simple fractional crystallization as plagioclase follows the liquid line of descent during cooling.

Dissolution rims or irregular zones are formed as a result of disequilibrium in the melt due to open system processes, or changes in pressure and temperature. Major and trace data suggest both recharge and assimilation occurred on Alicudi.

Sieve and patchy textures are also the result of disequilibrium in the melt caused by open system processes, or changes in pressure and temperature. Changes, both decreases and increases, in Anorthite content with in sieve and patchy textural zones suggest assimilation with crustal wall rock, and recharge from mafic melts played a small role in Alicudi's magmatic history.

Figure 16. Schematic of plagioclase textural types found in all samples. Sieve/Patchy textures are abundant in basalts and basaltic andesites, and simply or complex oscillatory are present. Andesites have abundant simple or complex oscillatory textures, but sieve/patchy textures are also present.

regions of plagioclase crystals are classified as patchy or sieve textures. Patchy zones

have irregularly distributed areas, typically block or patch like in shape, of a different

composition that are irregularly distributed in a "matrix" of plagioclase. Patchy zones are caused when resorption processes lead to removal of previously crystallized material, and new plagioclase in fills the resorbed areas. Patchy zones can form as result of disequilibrium caused by a recharge of a more mafic melt. Once the plagioclase re-equilibrates, new plagioclase of a higher An begins to fill in the resorbed areas (Ginibre et al., 2005). An additional process that leads the formation of patchy zones is from partial resorption during magma ascent. As magma rises in the conduits, PH_2O increases, causing the melt to become over saturated with H_2O and plagioclase to become unstable, forming resorbed areas. As the H_2O is released into the atmosphere, re-equilibrium in the plagioclase is established, and new plagioclase of lower An in fills the resorbed areas (Humphreys et al., 2006). This gives the plagioclase a patch-quilt like appearance. Like patchy zones, sieve textures are caused from resorption processes that lead to removal of previously crystallized material. Sieve textures can be the result of rapid growth and represent a form of quenched textures due to rapid ascent of the magma. On the other hand, sieve textures can be attributed to pervasive dissolution caused by disequilibrium as a result of open system processes (e.g. recharge of a new melt, or assimilation with crustal wall rock). Sieve zones are characterized by pools of glass that are irregularly distributed and are different sizes. The areas filled with glass give the crystal a sponge-like appearance. Sponge-like or box-like textures can be present in the intermediate and/or core region of plagioclase crystals. (Streck, 2008).

Stage 1 and 2 plagioclase crystals in basaltic and basaltic andesitic exhibit abundant patchy/sieve textures, with simple or complex oscillatory zoning present but

less abundant. In contrast, plagioclase crystals in andesites are characterized by abundant simple or complex oscillatory textural zones, and sieve/patchy textures are present but less abundant.

In Situ Plagioclase Major and Trace Element, and Sr Isotopic Data

Plagioclase major and trace elements (Fe, Mg, Ti, Ba, and Sr) were collected on 12 crystals per sample (120 crystals total) (Electronic Appendix A). Core to rim spot analyses were done on all phenocrysts, whereas microphenocrysts were characterized by a single analysis. Locations of all major and trace element spot analyses were based on textures and textural boundary identified in a subset of crystals imaged by NDIC (Electronic Appendix B). The distance between analyses within a single crystal ranges from 5 - 200 microns.

An Content

Microprobe results reveal ranges of An_{50}-An_{88} in basalts, An_{42}-An_{93} in basaltic andesites, and An_{45}-An_{88} in andesites (Figure 17a). Average An values overlap among all samples, but there is a general decrease in the range of average crystal An contents with increasing SiO_2 (Figure 17b). Stage 1 and 2 cores and rims have a wide range (An_{53-92}) in An. Stage 3 cores and rims also have a wide range in An (An_{42-87}), but are dominated by lower values. Although all stages have wide ranges in An, cores for all stages are dominated by higher An values, whereas rims are dominated by lower An values. For stages 1 and 2, microlites (plagioclase <20 μm) have similar An values
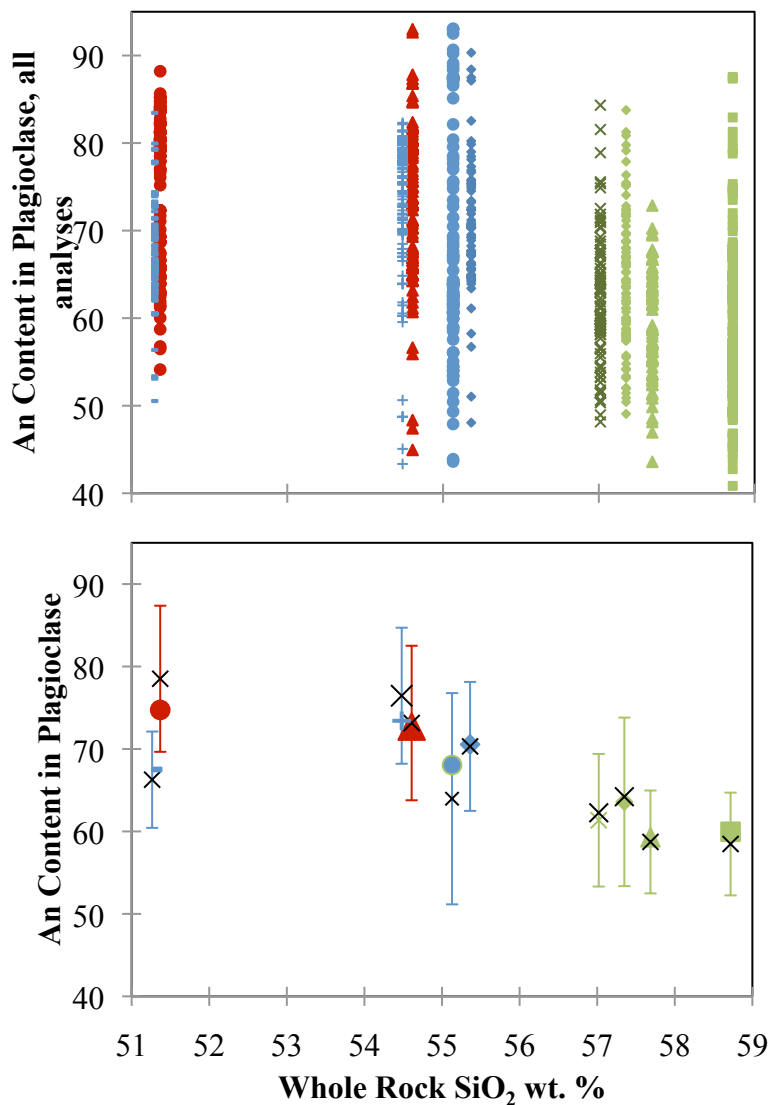
Figure 17. (a) Whole rock SiO_2 wt. % plotted against plagioclase An content ranges for all stages. (b) Whole rock SiO_2 wt. % plotted against plagioclase An content. Symbols represent average An for samples, black X's represent the median for the sample, whereas bars represent the standard deviation of the An content for the sample. Symbols are the same as in Figure 4.

(An_{48-80}) to rims of plagioclase phenocrysts (An_{43-83}). Stage 3 microlites typically have

lower values (An_{40-51}) than rims of plagioclase phenocrysts (An_{45-75}) (Figure 18a).
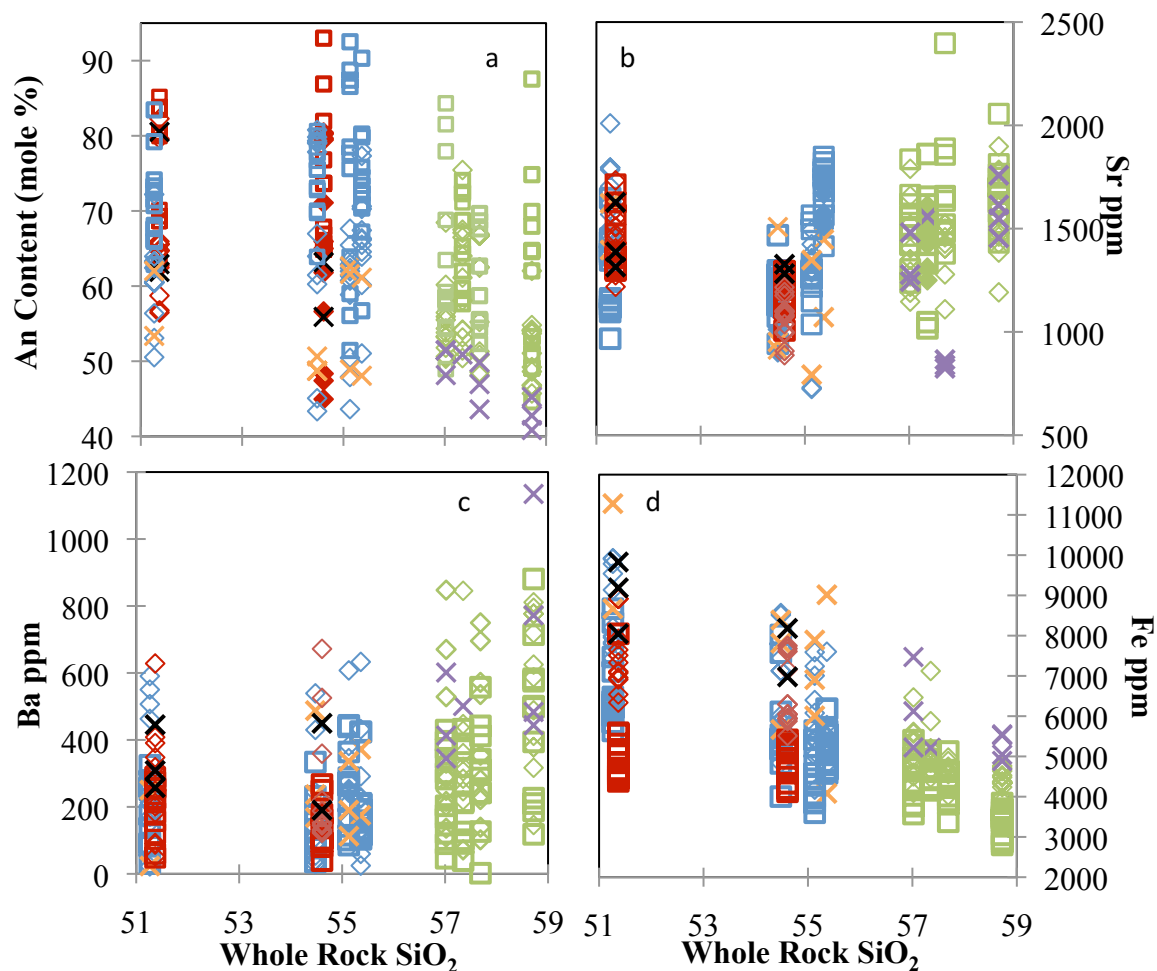
Figure 18. Whole rock SiO$_2$ wt.% plotted against (a) An content (mole %), (b) Sr (ppm), (c) Ba (ppm), and Fe (ppm) in rims (open diamond symbols), core (open square symbols), and microlites (x symbols) for all samples. Stage 1- blue diamonds and squares, orange x; stage 2- red diamonds and squares, black x; stage 3- green diamonds and squares, purple x.

Trace elements in plagioclase

Fe in plagioclase generally decreases with increasing whole rock SiO$_2$, although there is overlap in the Fe range for all of the samples (Figure 18b). Fe concentrations range from ~3,000-13,500 ppm for stage 1, 900-9,700 ppm for stage 2, and 2,300-7,400

ppm for stage 3 (Figure 20b). Mg (ppm) in plagioclase decreases with increasing whole

rock SiO_2 wt.% (Figure 19c), but an increase with Fe, overlap is noted. Mg

concentration in Stage 1 ranges from 100-1,900 ppm; stage 2 ranges from 250-1,300

ppm; stage 3 ranges from 120-800 ppm (Figure 20c). Overlap in Sr concentration is

evident across the compositional range, but the maximum Sr values generally increase

with increasing whole rock SiO_2 wt.% (Figure 19d). Sr in stage 1 ranges from 150-

2,100 ppm, stage 2 ranges from 1,400-1,750 ppm, and stage 3 ranges from 800-3,800

(Figure 20d). Ba concentration in plagioclase increases with increasing SiO_2, however

overlap is observed from 51.37-55.35 SiO_2 wt% (Figure 19e). Ba in stage 1 ranges from

10-800 ppm, stage 2 from 10-700 ppm, and stage 3 from 20-1,200 ppm (Figure 20e).

Plagioclase Ti concentrations overlap when plotted against whole rock SiO_2 wt%, and

lack systematic relationship with SiO_2 (Figure 19f). Ti concentrations range from 4-

1,030 ppm in stage 1, 5-800 ppm in stage 2, and 5-600 ppm in stage 3 (Figure 20f).

Stages 1, 2, and 3 microlites (plagioclase <20 μm) have similar Sr

concentrations (~450-1,800 ppm) and Ba ppm values (~20-800 ppm) to Sr ppm and Ba

ppm values in rims of plagioclase phenocrysts (~150-2,100 ppm and ~20-900 ppm)

(Figure 18b and c). However, one microlite from sample ALI10-03 (stage 3) has

anomalously high Ba (1134 ppm). Additionally, in sample ALI10-17 (stage 3),

microlites have lower Sr (~800-900 ppm) than cores and rims of plagioclase

phenocrysts (~1,300-1,900 ppm). Fe concentrations in microlites from stages 1 (4,000-

9,100), 2 (6,900-10,000), and 3 (4,500-7,500) are typically similar to or higher than Fe

ppm values for plagioclase phenocryst rims (3,800-7,100) (Figure 18d).
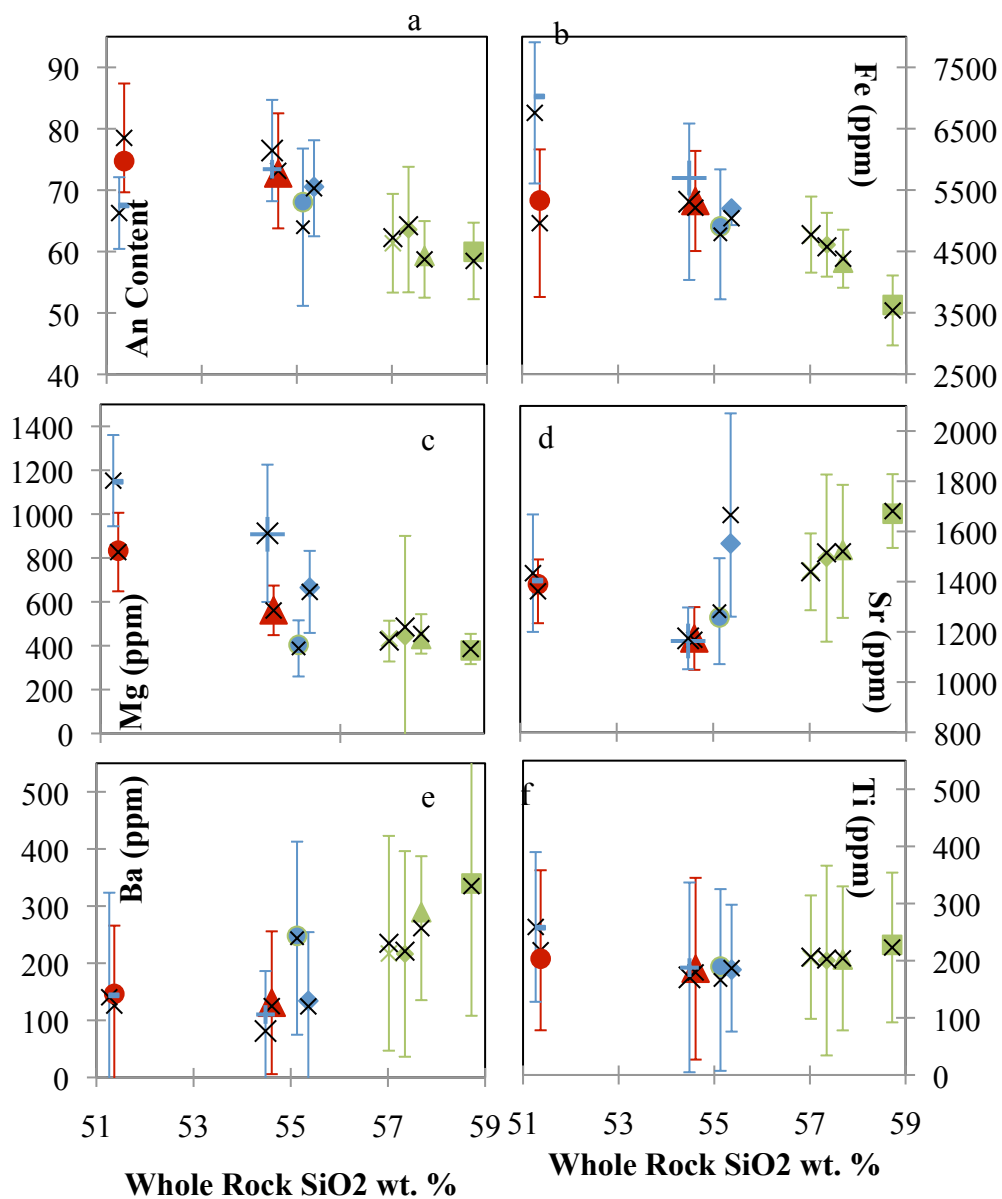
Figure 19. Whole rock SiO₂ (wt.%) plotted against the average (colored symbols), the median (black x's), and standard deviation (colored error bars) of (a) An content, (b) Fe, (c) Mg, (d) Sr, (e) Ba, and (f) Ti. For individual sample symbols, see Figure 4.
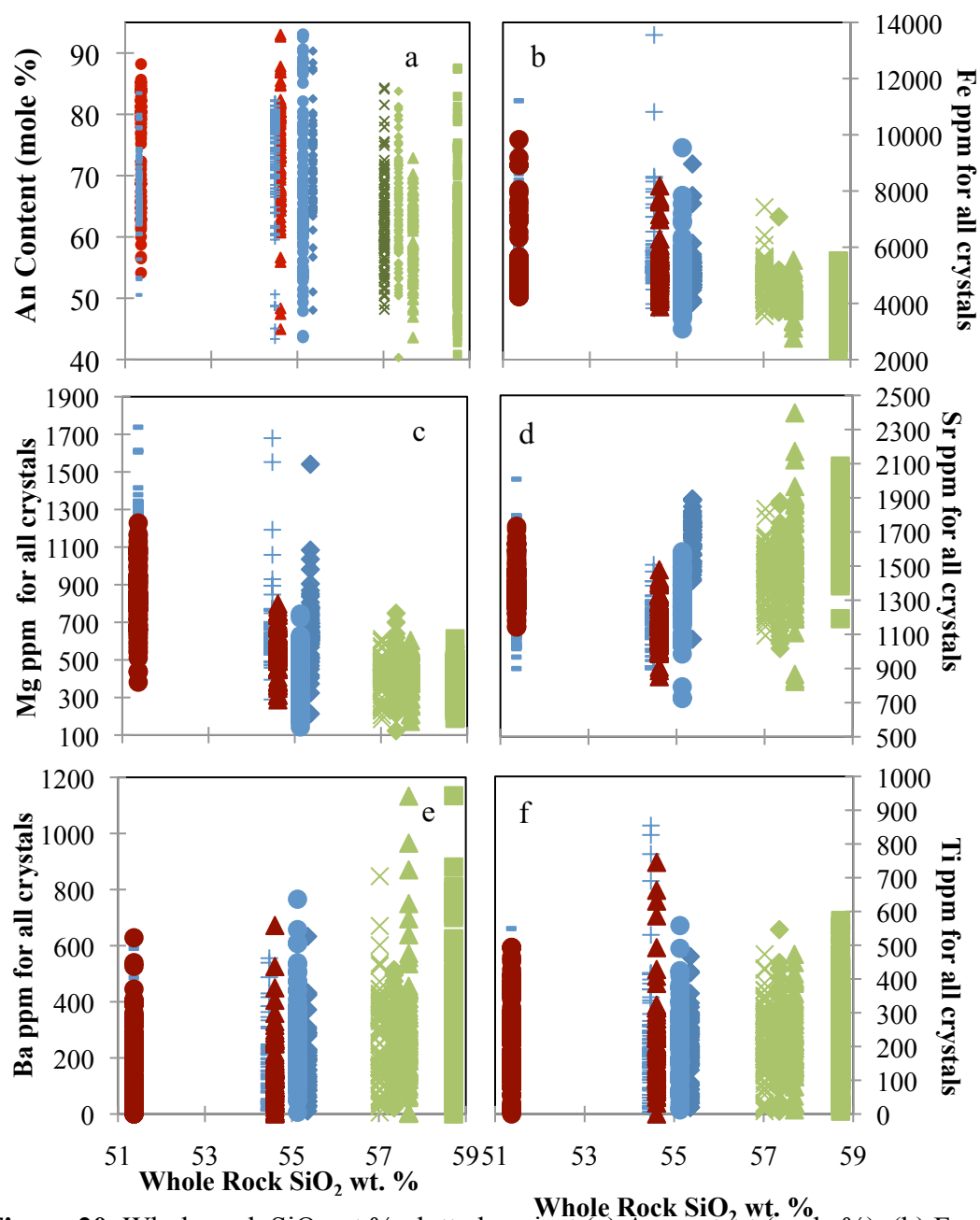
Figure 20. Whole rock SiO$_2$ wt.% plotted against (a) An content (mole %), (b) Fe (ppm), (c) Mg (ppm), (d) Sr (ppm), (e) Ba (ppm), and (f) Ti (ppm) for all plagioclase microprobe point analyses. Symbols are the same as in Figure 4.

When plotted against An content (mole %), Sr, Ba, and Ti (ppm) generally decrease

with increasing An content, although there is a wide range of values of all of these

elements at the same An (Figure 21). For most samples, Fe and Mg exhibit wide ranges;
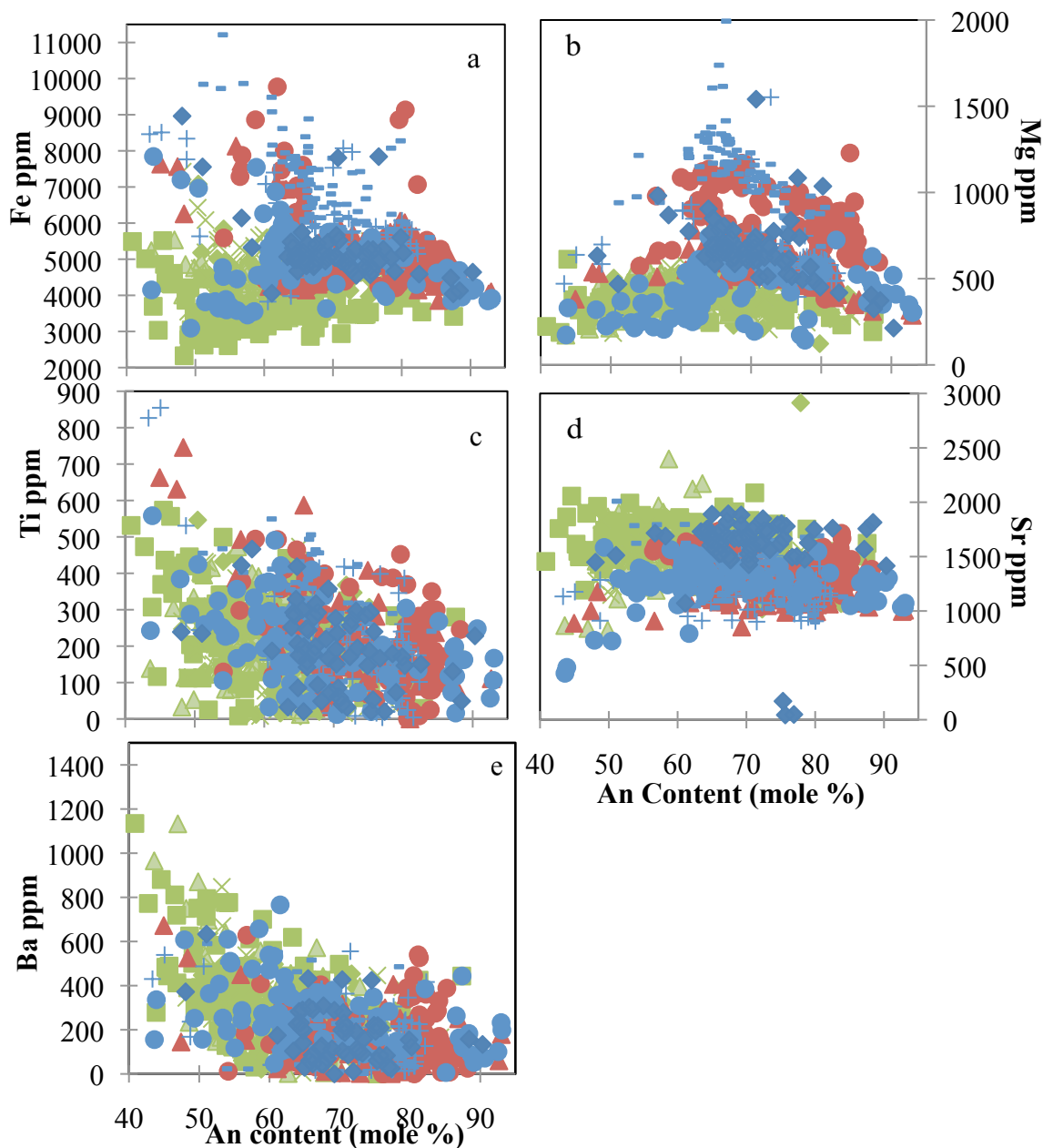
Figure 21. An content (mole %) plotted against plagioclase trace elements (a) Fe, (b) Mg, (c) Ti, (d), Sr, and (e) Ba (ppm) for all plagioclase crystals analyzed. See Figure 4 for sample symbols.

stages 1 and 2 have higher Fe and Mg ppm than stage 3 (Figure 22). Samples ALI10-05, 07, 08, and 10 have decreasing Mg with increasing An (Figure 22a-c). Additionally, andesites typically have higher Sr concentrations than stages 1 and 2 (Figure 23).

Plagioclase Major and Trace Element and Textural Data Combined

Figure 24 rim-core illustrates the rim to core An zoning in crystals larger than microlites. Typically, crystals are normally zoned; however, reversely zoned plagioclase is present (Figure 24). In most samples, changes in An content of $\geq$10% are noted rimward of dissolution rims/boundaries or within sieved/patchy zones (Figure 25). Decreases in An content $\geq$ 10% after textural transitions are more common than increases in An content of $\geq$ 10% after textural transitions. However, the most common scenario is changes in An that are <10% (Figure 24b).

Fe is typically inversely correlated with An content. Thus Fe typically increases rimward of dissolution boundaries, whereas An decreases. Although plagioclase textural changes are often accompanied by sharp changes in major and trace elements, systematic correlations between delta An or An content and textural transition are lacking. For example, sample ALI10-07 plagioclase 12 has a patchy textural zone characterized by an analysis of An_{65}. After a rimward textural transition to oscillatory, the An content increases by 10 mole % to An_{75}. Sample ALI10-05 plagioclase 12 (Figure 24) exhibits the opposite trend in which the An content increases by 10 mole % (from An_{63} to An_{75}) with a rimward textural transition from oscillatory to sieve. Comprehensive illustration of the plagioclase core to rim profiles can be found in Electronic Appendix A, Reduced microprobe data and profiles.
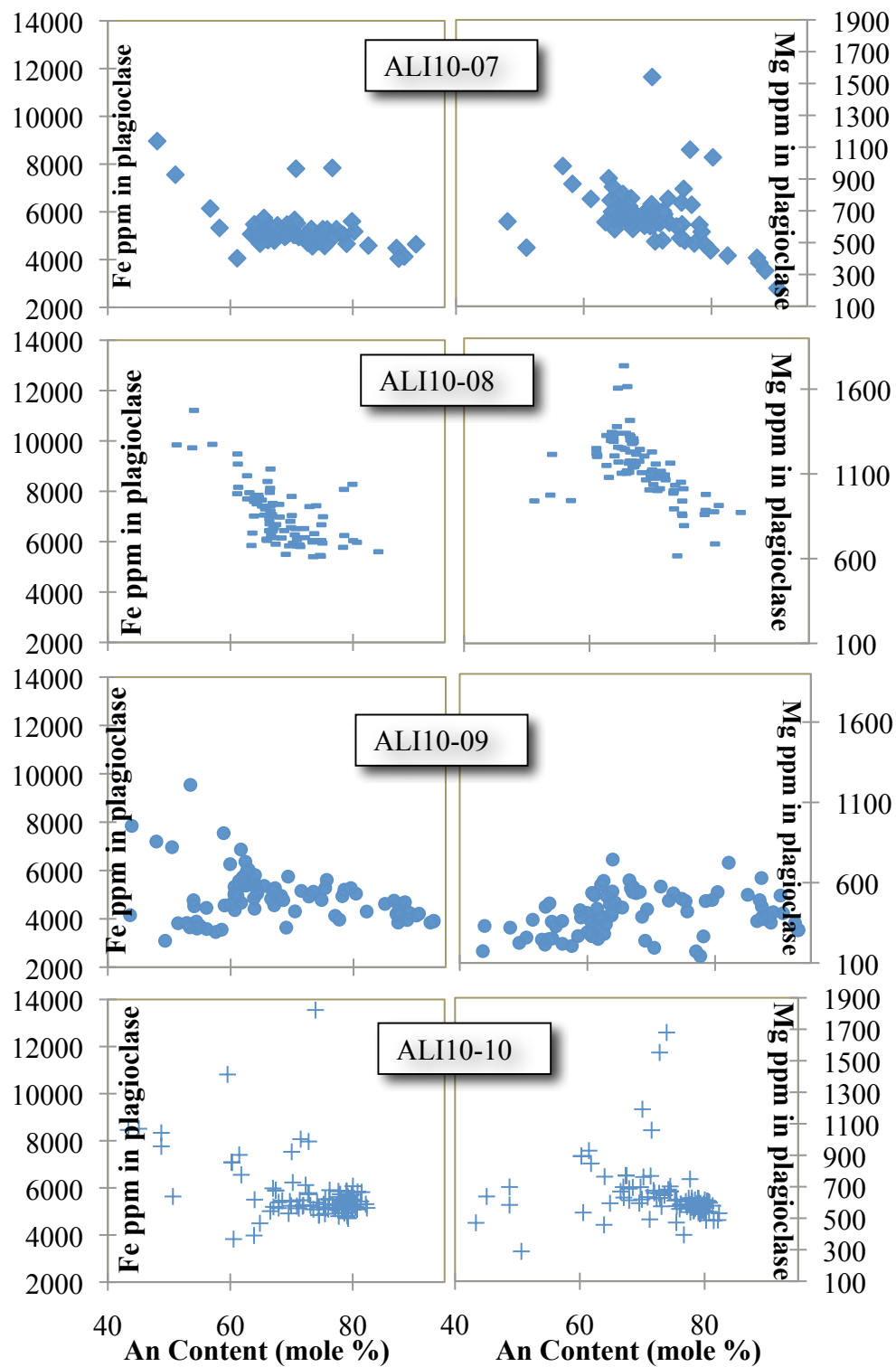
Figure 22. (a) Plagioclase An content (mole %) plotted against stage 1 Fe and Mg ppm in plagioclase. Symbols are the same as Figure 4.
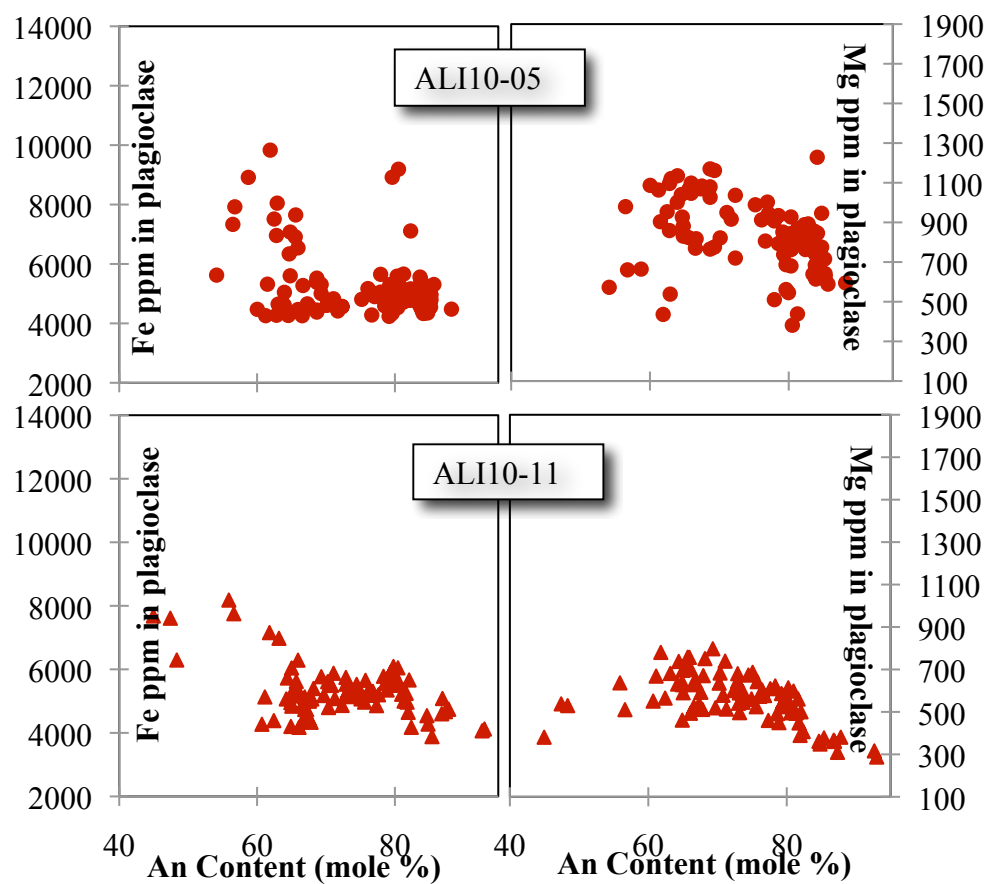
Figure 22 (cont.). b) Plagioclase An content (mole %) plotted against Stage 2 Fe and Mg ppm in plagioclase. Symbols are the same as Figure 4.
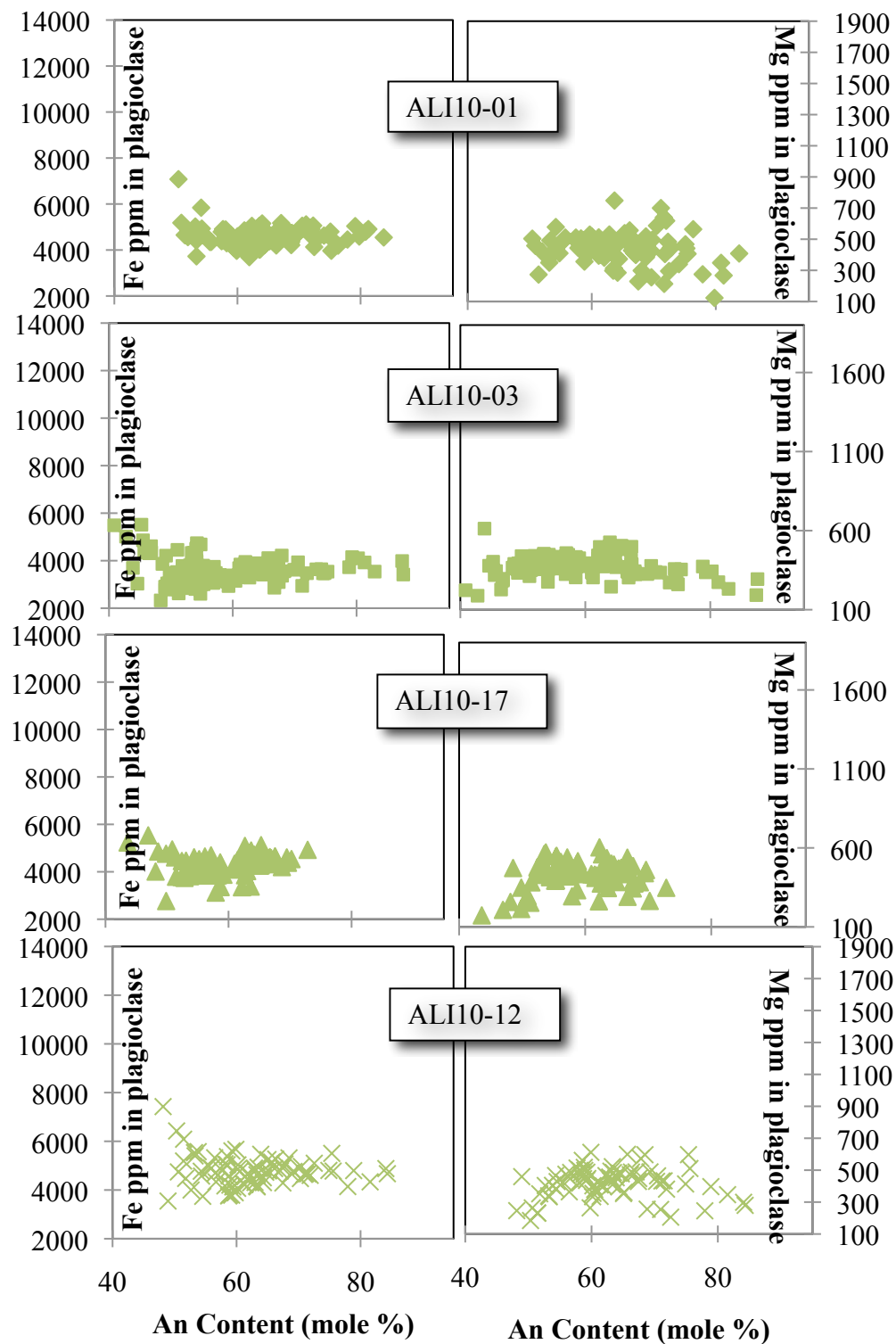
Figure 22 (cont.). (c) Plagioclase An content (mole %) plotted against stage 3 Fe and Mg ppm in plagioclase. Symbols are the same as Figure 4.
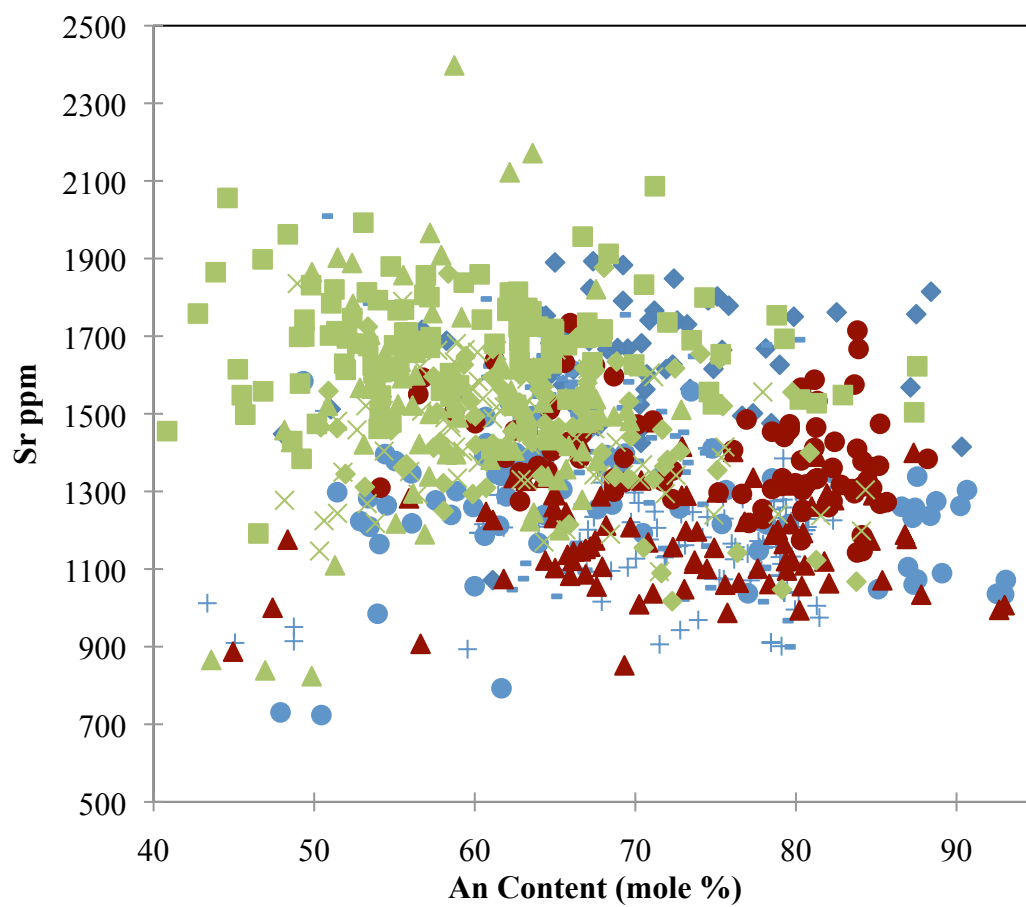
Figure 23. Plagioclase An content (mole %) plotted against Sr (ppm) for all stages. Symbols are the same as Figure 4.
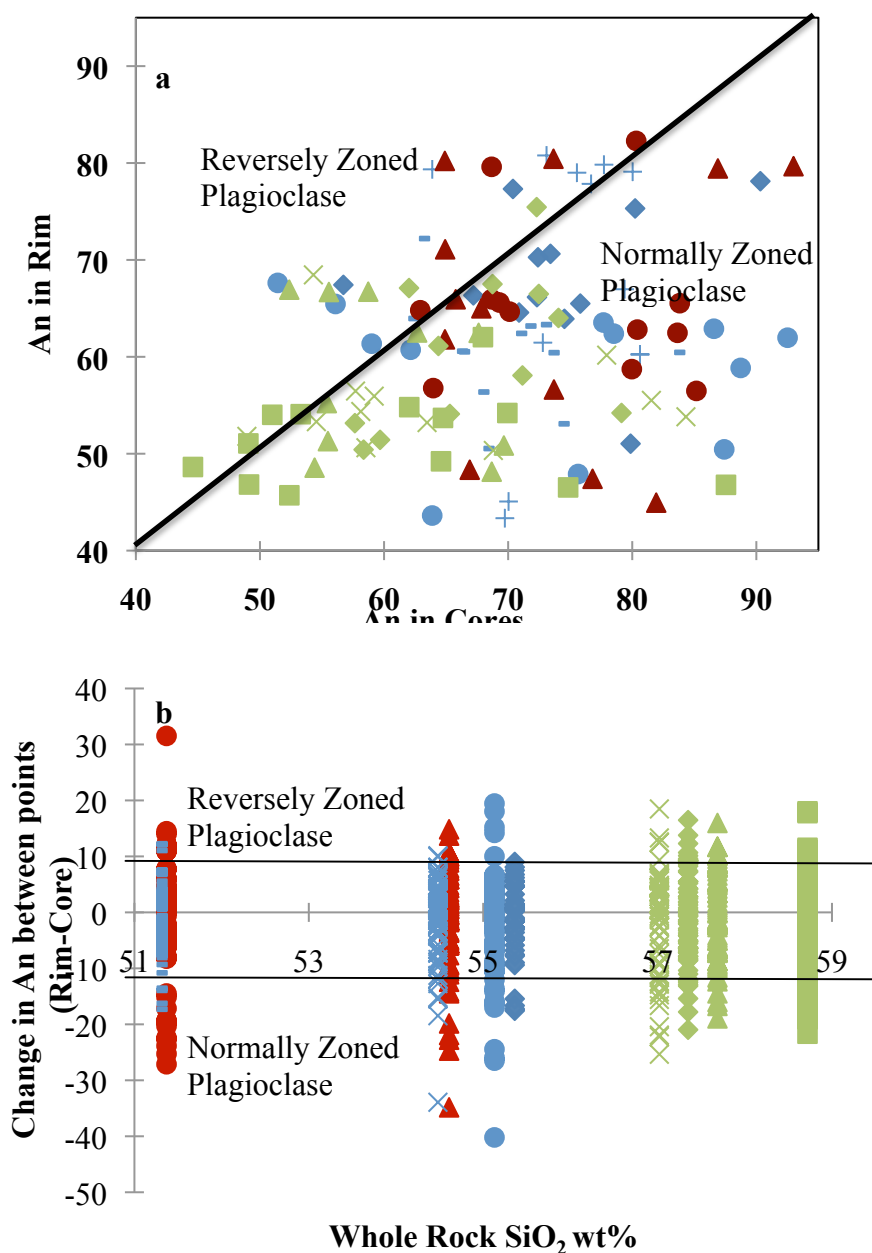
Figure 24. (a) An content in cores plotted against An content in rims. Black line represents 1:1 trend. Values plotted above black line represent reversely zoned crystals, whereas values that plot below line represent normally zoned crystals. (b) Whole rock SiO_2 wt.% plotted against change in An between all adjacent microprobe points (rimward point subtracted from coreward point). Samples that have increases of $>An_{10}$ (reversely zoned plagioclase) are evidence of recharge. Samples that have decreases $>An_{10}$ (normally zoned plagioclase) may be the result of AFC. Samples with changes $<An_{10}$ may be the result of FC processes. For sample names, see Figure 4.
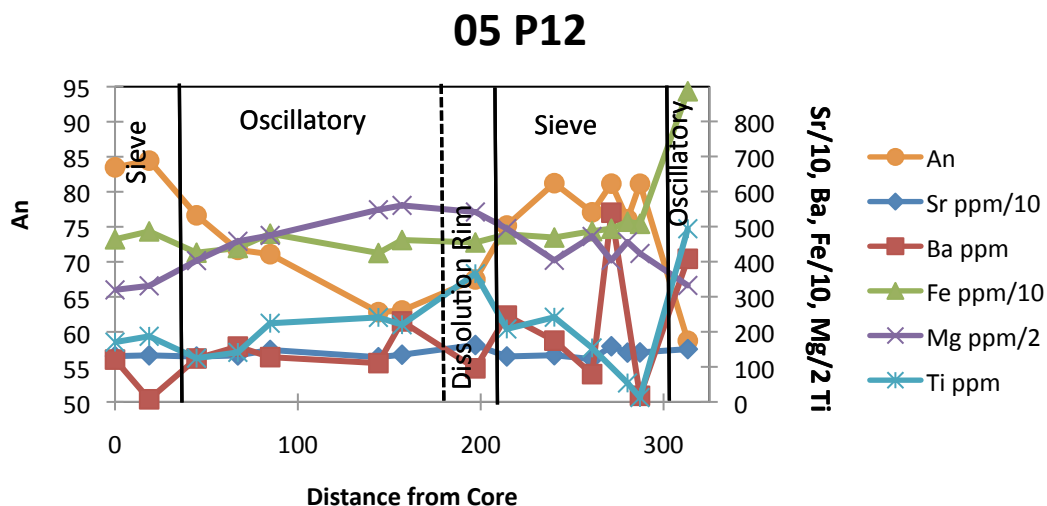
Figure 25. (a) Plagioclase major and trace element profile of sample ALI10-05 (stage 2, basaltic andesite), plagioclase 12. Distance from the core plotted against An content is plotted on the left, trace elements plotted on the right. Thick black lines represent sieve and oscillatory boundaries and dashed black lines represent dissolution boundary. (b) NDIC image of ALI10-05 plagioclase 12. Red dots are microprobe points, associated with An value labeled in red above dots. Laser trough is noted by black polygon, and $^{87}Sr/^{86}Sr$ value in black.

In Situ Plagioclase $^{87}Sr/^{86}Sr$

Radiogenic Sr in plagioclase was measured using LA-MC-ICPMS (Table 6). Eighty-one analyses were completed on crystals from stages 1, 2, and 3 that were analyzed for major and trace elements. Crystals within all samples have heterogeneous $^{87}Sr/^{86}Sr$ signatures: stage 1 plagioclase crystals have the highest and most variable $^{87}Sr/^{86}Sr$ (0.70277-0.70386), whereas andesitic plagioclase crystals have the lowest and least variable (0.70284-0.70357). Stage 2 plagioclase crystals $^{87}Sr/^{86}Sr$ values are 0.70323-0.70423 (Figure 26).
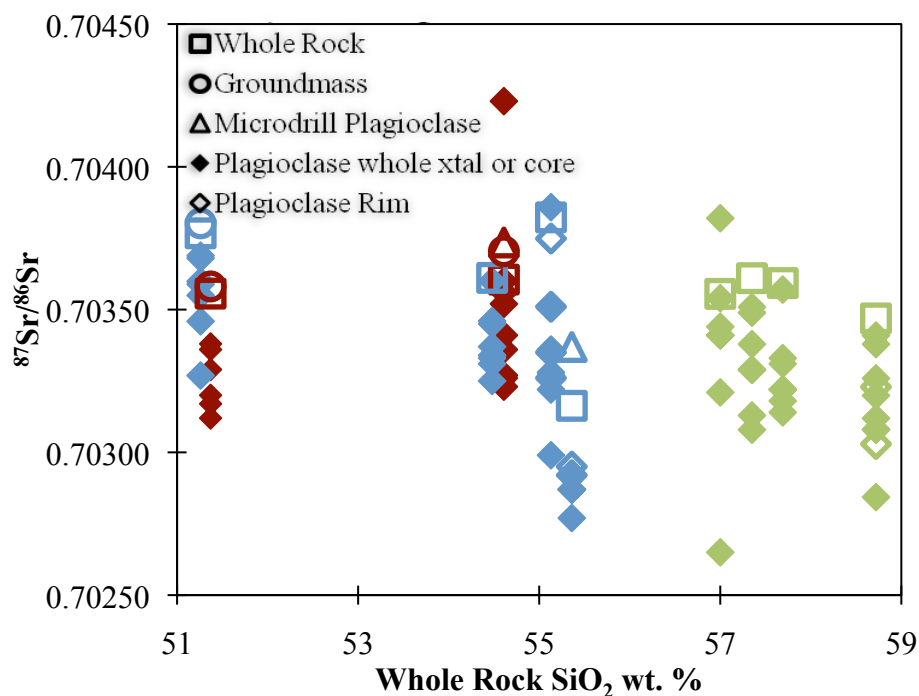
Figure 26. Whole rock SiO_2 wt.% plotted against whole rock, groundmass, and *in situ* plagioclase $^{87}Sr/^{86}Sr$. Colors same as Figure 4.

Because the typical size of plagioclase crystals in the Alicudi samples was less than 600 μm, only eight crystals were analyzed for core and rim $^{87}Sr/^{86}Sr$ (ALI10-11 P21, ALI10-09 P23, P10, P21, ALI10-07 P14, P22, and ALI10-03 P13, P2) (Figure 27).

TABLE 6. LA-MC-ICPMS PLAGIOCLASE DATA

Sample	$^{87}Sr/^{86}Sr$	Uncertainty	LA analysis Location
Stage 1			
ALI10-07-P18	0.70277	0.000042	Core
ALI10-07_P23	0.70292	0.000042	Core
ALI10-07_P14C	0.70287	0.000042	Core
ALI10-07_P14R	0.70292	0.000042	Rim
ALI10-07_P1	0.70287	0.000042	Rim
ALI10-07_P22C	0.70287	0.000042	Core
ALI10-07_P22R	0.70295	0.000042	Rim
ALI10-07_P9	0.70287	0.000042	Rim
ALI10-08_P4	0.70369	0.000033	Rim
ALI10-08_P12	0.70327	0.000033	Core
ALI10-08_P10	0.70359	0.000033	Core
ALI10-08_P23	0.70360	0.000033	Rim
ALI10-08_P24	0.70355	0.000042	Whole Xtal
ALI10-08_P14	0.70368	0.000042	Whole Xtal
ALI10-08_P1	0.70346	0.000033	Rim
ALI10-09_P4	0.70219	0.000033	Core
ALI10-09-P8	0.70299	0.000033	Core
ALI10-09-P8L	0.70386	0.000033	Sieve left
ALI10-09-P8R	0.70375	0.000033	Sieve right
ALI10-09-P23C	0.70335	0.000042	Core
ALI10-09_P23R	0.70351	0.000042	Rim
ALI10-09_10C	0.70326	0.000042	Core
ALI10-09_10R	0.70327	0.000042	Rim
ALI10-09_P14	0.70328	0.000042	Rim
ALI10-09_P21C	0.70336	0.000042	Core
ALI10-09_P21R	0.70322	0.000042	Rim
ALI10-10_P6	0.70325	0.000042	Rim
ALI10-10_P12	0.70334	0.000042	Core
ALI10-10_P21R	0.70333	0.000042	Rim
ALI10-10_P14	0.70331	0.000042	Core
ALI10-10_P22	0.70360	0.000042	Whole Xtal
ALI10-10_P19	0.70345	0.000042	Whole Xtal
ALI10-10_P20	0.70337	0.000042	Core
ALI10-10_P17	0.70346	0.000042	Core

TABLE 6. (CONT.)			
Sample	$^{87}Sr/^{86}Sr$	Uncertainty	LA analysis Location
Stage 2			
ALI10-05-P8	0.70317	0.000042	Core
ALI10-05_P3	0.70329	0.000042	Rim
ALI10-05_P4	0.70320	0.000042	Rim
ALI10-05_P11	0.70338	0.000042	Whole Xtal
ALI10-05_P2	0.70312	0.000042	Rim
ALI10-05_P12	0.70336	0.000042	Whole Xtal
ALI10-11-P21C	0.70352	0.000042	Core
ALI10-11_P21R	0.70360	0.000042	Rim
ALI10-11_P14	0.70327	0.000042	Core
ALI10-11_P9	0.70336	0.000042	Rim
ALI10-11_P11	0.70323	0.000042	Rim
ALI10-11_P5	0.70423	0.000042	Rim
ALI10-11_P2	0.70326	0.000042	Whole Xtal
ALI10-11_P22C	0.70341	0.000042	Core
ALI10-11_P13	0.70356	0.000042	Rim
Stage 3			
ALI10-01_p4	0.70349	0.000033	Core
ALI10-01_P9	0.70338	0.000033	Core
ALI10-01_P6	0.70313	0.000033	Rim
ALI10-01_P17	0.70329	0.000033	Core
ALI10-01_P12	0.70308	0.000033	Core
ALI10-01_P13	0.70329	0.000033	Whole Xtal
ALI10-01_P25	0.70351	0.000033	Rim
ALI10-01_P20	0.70524	0.000033	Rim
ALI10-03_P13C	0.70312	0.000033	Core
ALI10-03_P13R	0.70323	0.000033	Rim
ALI10-03_P2C	0.70341	0.000033	Core
ALI10-03_P2R	0.70303	0.000033	Rim
ALI10-03_P4	0.70308	0.000033	Core
ALI10-03_P7C	0.70284	0.000033	Core
ALI10-03_P3	0.70326	0.000033	Rim
ALI10-03_P9	0.70338	0.000033	Rim
ALI10-03_P10	0.70308	0.000033	Core
ALI10-03_P8	0.70320	0.000033	Rim

TABLE 6. (CONT.)

Sample	$^{87}Sr/^{86}Sr$	Uncertainty	LA analysis Location
Stage 3			
ALI10-17-P3	0.70314	0.000042	Core
ALI10-17_P8	0.70322	0.000042	Rim
ALI10-17_P13	0.70333	0.000042	Core
ALI10-17_P19	0.70331	0.000042	Rim
ALI10-17_P5	0.70318	0.000042	Rim
ALI10-17_P7	0.70322	0.000042	Whole Xtal
ALI10-17_P6	0.70357	0.000042	Core
ALI10_12-P1	0.70265	0.000042	Core
ALI10-12_P3	0.70382	0.000042	Rim
ALI10-12_P20	0.70354	0.000042	Rim
ALI10-12_P13	0.70341	0.000042	Core
ALI10-12_P14	0.70341	0.000042	Core
ALI0-12_P17	0.70321	0.000042	Rim
ALI10-12_P16	0.70344	0.000042	Rim

$*^{87}Sr/^{86}Sr$ plagioclase analyses.

For all crystals except ALI10-03 P2 and ALI10-09 P21, $^{87}Sr/^{86}Sr$ values are higher in the rims. The exceptions (ALI10-03 P2 and ALI10-09P21) show the $^{87}Sr/^{86}Sr$ value is lower in the rim. See Figure 25 for an example of trough size on plagioclase samples.

For all samples, whole rock $^{87}Sr/^{86}Sr$ is within uncertainty of the groundmass values (Figure 26). In most samples, whole rock and groundmass values are higher than to most *in situ* plagioclase Sr isotope values. Also, Alicudi has lower $^{87}Sr/^{86}Sr$ values than Filicudi and Salina (Figure 28).
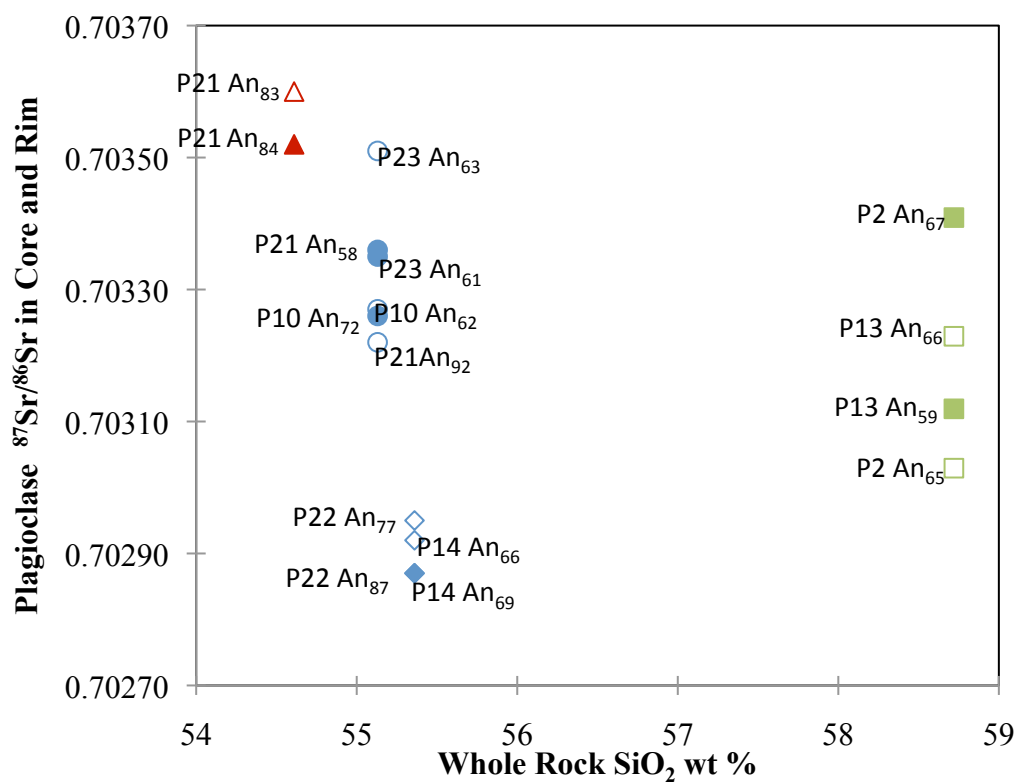
Figure 27. Whole rock SiO_2 wt. % plotted against *in situ* plagioclase $^{87}Sr/^{86}Sr$ in core and rim. An content annotated next to points. P# = Plagioclase #. Open symbols represent $^{87}Sr/^{86}Sr$ plagioclase rim, whereas closed symbols represent plagioclase core analyses of $^{87}Sr/^{86}Sr$. Symbol shapes are same as in Figure 4.
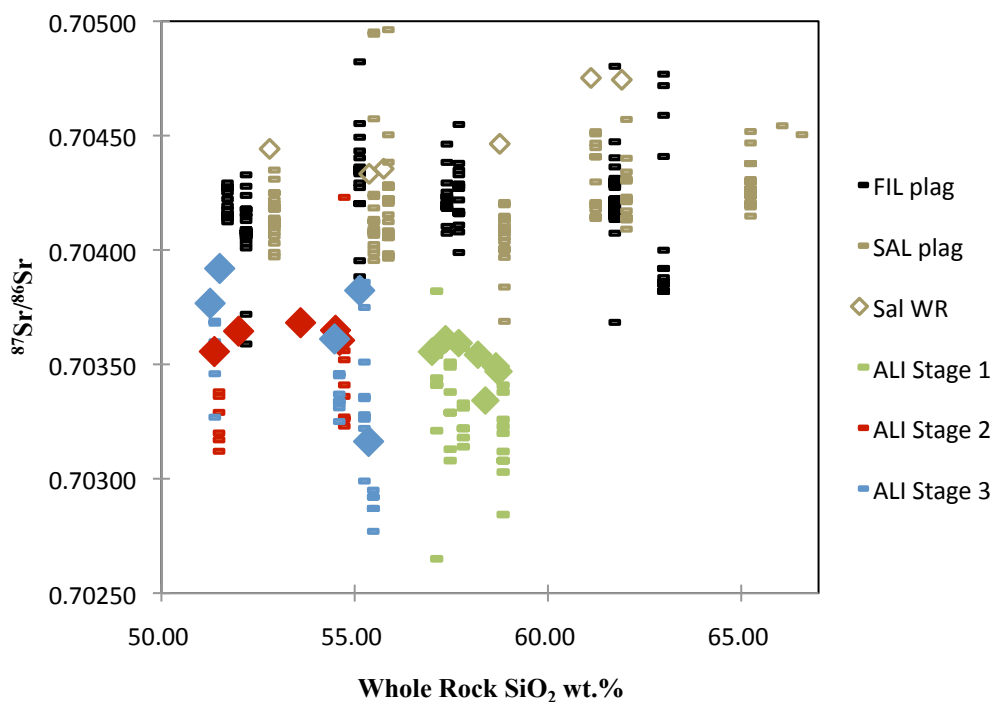
Figure 28. Whole rock SiO_2 wt. % plotted against whole rock and plagioclase $^{87}Sr/^{86}Sr$ for Alicudi, and adjacent islands of Salina, and Filicudi. Symbols are as follows: plagioclase are marked by -, whole rock analyses are marked by diamonds. Alicudi stage 1- blue symbols; stage 2- red symbols; stage 3- green symbols. Salina's symbols are brown; Filicudi's symbols are black. Filicudi's whole rock $^{87}Sr/^{86}Sr$ values are pending. Uncertainties for TIMS analysis are ±0.00001. Reproducibility for LA-MC-ICPMS is ±0.00004

MELTS Models

Alicudi whole rock major element data were compared with the results of 60

MELTS models. All simulations were run using the whole rock compositions of

Alicudi, sample ALI10-05, or Filicudi, sample FIL10-22 (Harris, pers. communication)

as parental magma input. Both parental magmas were compared to observed major

elements trends from Alicudi, but trends using the Alicudi parent yield results that do

not fit many of the major element trends. Comparison of whole trends for Alicudi,

Filicudi, and Salina suggest that several of the major element trends, including MgO

and Al_2O_3, do not likely represent a crystal fractionation liquid line of descent. Thus,

Filicudi's most mafic sample, FIL10-22, was used as a representative parental magma.

The Filicudi sample shares characteristics with the mafic samples from Alicudi and thus

the assumption is made that it best represents a potential parental magma (Figure 4). Of

the 60 MELTS runs, the most successful were run under polybaric mode, fO_2 of

hematite-magnatite, and water content of 3 %.

CHAPTER V

DISCUSSION

Collectively, whole rock and *in situ* plagioclase major and trace element and Sr isotope data permit an integration of three new hypotheses to explain the causes of compositional diversity seen on Alicudi. The first hypothesis suggests that mantle source heterogeneity, as seen in mafic whole rock trace element and isotope data from stages 1, and 2, played a critical role in establishing the variable mafic signatures observed on Alicudi. The second hypothesis, formed from whole rock major and trace element and *in situ* plagioclase textural, major, and trace data, suggest recharge and assimilation contributed to Alicudi's magmatic evolution. Source heterogeneity and open-system processes are evident in the petrogenetic evolution of Alicudi and can be integrated into a third hypothesis that proposes a mixing, assimilation, storage, and homogenization scenario. This is primarily supported by the combination of data from the two previous hypotheses and decreasing degree of variability in whole rock and plagioclase data, particularly Sr isotopes, from stage 1 to 3. Each hypothesis is described in detail below.

The Role of Mantle Source Heterogeneity

Variations in whole rock trace element and isotope trends for basalt and basaltic andesite rocks from Alicudi can best be explained by invoking melting of a heterogeneous mantle source region. This hypothesis is examined in detail below, as is

the alternative hypothesis put forward by Peccerillo et al. (2004) that suggests

assimilation in basalts is the primary cause of compositional heterogeneity in the mafic

rocks.

Within a relatively narrow range of SiO_2, stage 1 and 2 samples (basalt and

basaltic andesite) show variability in selected trace elements (Figures 6, 7, and 8). For

example, Ba varies by 300 ppm in mafic samples between 50 and 55 SiO_2 (wt.%), the U

range for the same SiO_2 range is 2.5 ppm, and La varies by 20 ppm. Additional

elements that vary are Nb, and Th. In comparison Ba in andesites varies by 200 ppm, U

ranges by .5 ppm, and La varies by 5 ppm for a sample range of 55-60 SiO_2. Stage 3 is

more enriched with REEs, as expected for andesitic whole rock compositions. However,

the range of REEs abundances is least variable in stage 3; stage 1 is the most variable

and least enriched (Figure 9). Similar to trace elements, $^{87}Sr/^{86}Sr$ is more variable in

stage 1 than stage 3 (Figure 10). Furthermore, Sr isotope values are typically lower in

stage 3 andesites compared to stage 1 and 2 rocks. A likely hypothesis that explains

both the trace element and radiogenic isotope variability involves melting of a source

region that is compositionally heterogeneous. Different degrees of melting of the same

source might lead to trace element heterogeneity, but this model is less plausible to

explain variable radiogenic isotope signatures because simple modal melting of such a

source region yields melts with the same isotope characteristics.

The importance of source heterogeneity at Alicudi is supported by comparisons

between data from Alicudi and those from neighboring islands, Filicudi and Salina

(Figures 6, 7, and 8). Within the same SiO_2 range of 50 to 55 wt.%, Ba in Filicudi

samples range by 100 ppm and Salina ranges by 50 ppm, U ranges by 1 and .5 ppm, and La varies by 5 and 2, respectively. Nb and Th also have higher ranges on Alicudi than Filicudi and Salina (Figure 6, 7, and 8). Pb is slightly less enriched on Alicudi. Additionally, Alicudi has less radiogenic $^{87}Sr/^{86}Sr$ signatures than Filicudi and Salina (Figure 28) and more radiogenic $^{143}Nd/^{144}Nd$ signatures than Salina (Figure 11). While variability of whole rock trace elements could be explained by different degrees of melting of a common source, distinct isotope signatures amongst sample populations from the three islands support melting of a heterogeneous mantle source region.

A possible mechanism to introduce heterogeneity into magmatic systems at arc volcanoes such as Alicudi, Salina and Filicudi is addition of variable amounts of radiogenic Sr and incompatible elements to the mantle wedge from fluids or melts from the down going slab (Peccerillo and Wu, 1992). Melting of a source region enriched by subduction zone fluids or melts might typically lead to increases in $^{87}Sr/^{86}Sr$ and abundances of incompatible elements soluble in fluids (such as Rb and Ba). While the range of Ba, U, La, and other trace elements in the most mafic rocks might be explained by mantle enrichment, all stages have much lower $^{87}Sr/^{86}Sr$, stage 3 being the lowest, than samples from the other islands. This suggests a melting process that is complex.

Role of Crustal Level Processes

Whole rock major and trace element data and plagioclase *in situ* textural, major and trace element and isotope data provide evidence that recharge of more mafic

magma into a host chamber and assimilation of gabbro played integral parts in the evolution of Alicudi's magmas.

Fractional Crystallization

Fractional crystallization in all stages is supported by MELTS modeling and fractionation trends seen in trace element data. Polybaric MELTS model, Run 52 (Table 1), that used Filicudi's most mafic sample as the parental magma for Alicudi yielded trends that matched most observed major oxide trends on Alicudi (Figure 29). Because MELTS is based on equilibria assimilation-fractional crystallization, it is suggested that stage 3 partially evolved from fractionatal crystallization of stages 1 and 2. In addition, fractionation trends with a liquid fraction of 0 and 40% remaining liquid were added to incompatible trace element diagrams. For most incompatible trace elements, the fractionation trends are similar to observed trends (Figure 7 and 8), again suggesting the andesites are in some way related to previous stages by fractional crystallization. Furthermore, decreases in An content $\geq$10% coupled with textural changes such as dissolution rims or sieved/patchy textures are common in Alicudi plagioclase crystals. Also, decreasing An $\geq$10% rimward over a distance of 10 to 20 microns (normally zoned crystals) is consistent with fractional crystallization (Figure 24).

Assimilation

Assimilation in stage 1 and 2 basalts and basaltic andesites is supported by high values of MgO (wt. %) and Ni (ppm), compared to samples with similar SiO_2 (wt. %) from Salina and Filicudi (Figure 5 and 6). MgO and Ni are also positively correlated (Figure 30). Additional whole rock observations include relatively depleted Al_2O_3,
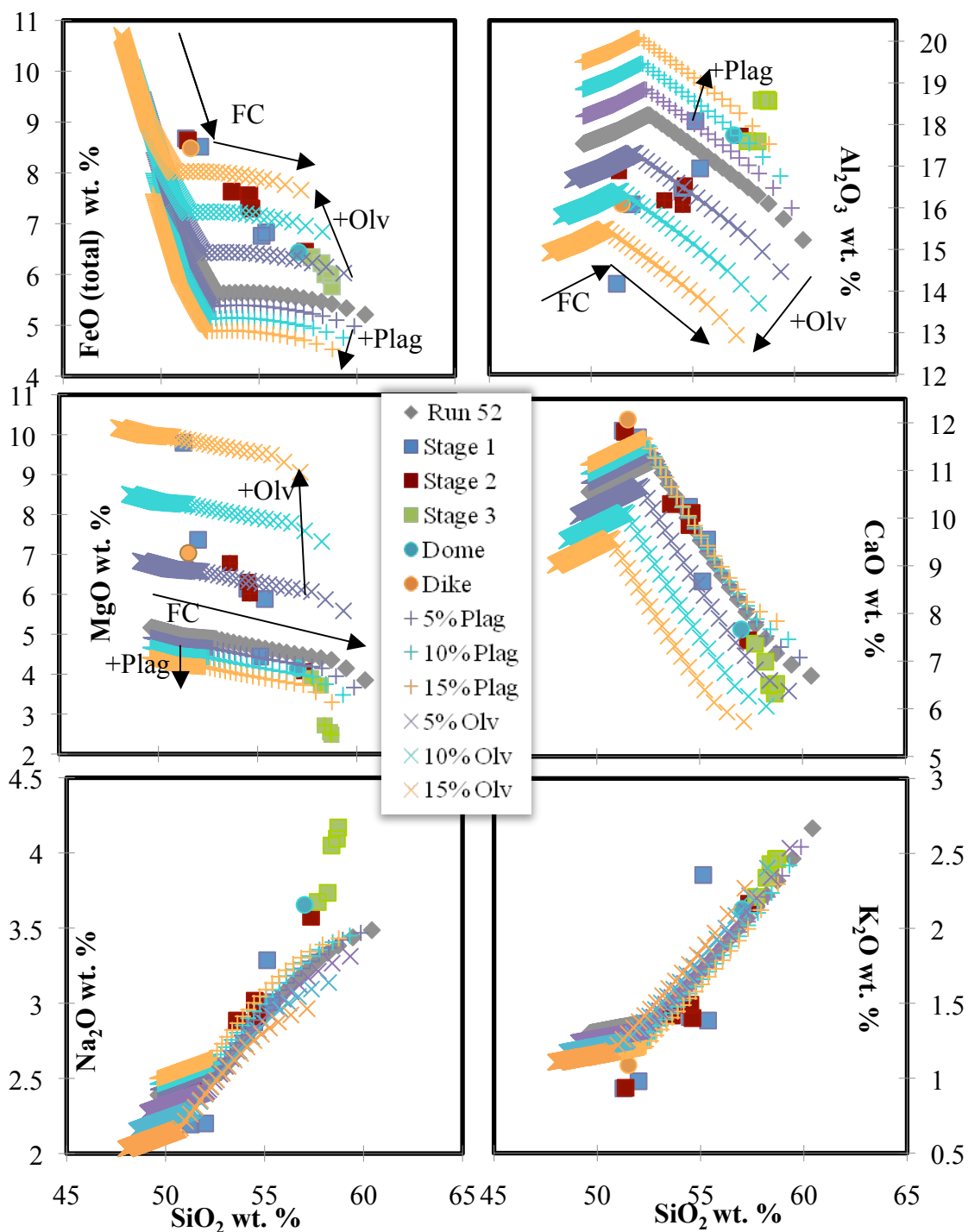
Figure 29. MELTS model, Run 52, based on polybaric conditions and addition of 5%, 10%, and 15% plagioclase (+ symbols) and olivine (x symbols). MELTS results are represented by gray trends. Results plot SiO_2 wt. %. vs. (a) FeO (total), (b) Al_2O_3, (c) MgO, (d) CaO, (e) Na_2O, and (f) K_2O wt. %. For specific parameters used, see Table 6.

compared to mafic rocks from the other two islands. Enrichment of MgO and Ni

(coupled with distinct depletion in Al₂O₃) above that of basalts and basaltic andesites

from Salina and Filicudi may suggest olivine accumulation.
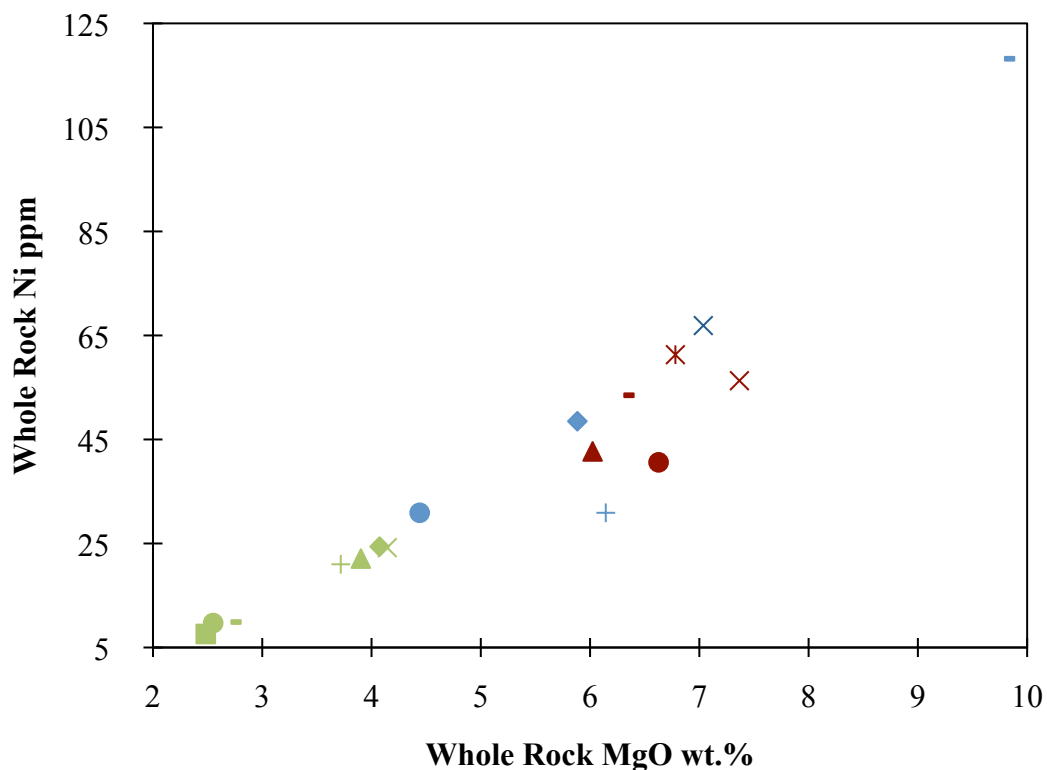
Figure 30. Whole rock MgO wt. % vs. Ni (ppm). Stage 1- blue symbols, stage 2- red symbols, stage 3- green symbols. For sample symbols, see Figure 4.

In addition, in contrast to the comparatively low Al₂O₃ and Sr in mafic samples

from Alicudi, whole rock Al₂O₃ (wt. %) and Sr (ppm) are elevated in stage 3 andesites.

Fractional crystallization trends that have plagioclase as a liquidus phase typically have

decreasing Al₂O₃ and Sr with increasing SiO₂ wt.%. Thus, assuming the mafic magmas

are genetically related to the andesitic ones, the expectation for the Al₂O₃ and Sr vs.

SiO_2 trends is that the andesites would have significantly lower values than they do. Plagioclase accumulation could explain the elevated Al_2O_3 and Sr trends.

To test the petrogenetic relationships among the Alicudi rocks as well as the suggestion that the more mafic rocks have accumulated olivine and the andesitic rocks have accumulated plagioclase, a series of MELTS simulations were performed. Using compositions of the best fit MELTS results (Run 52, which is polybaric simulation with FIL10-22 as a parent (Table 1)), many of the observed SiO_2 vs. oxides trends match those from the simulation. Two clearly do not—MgO and Al_2O_3. To examine the impact that accumulation of olivine and plagioclase has on major element oxide trends, a simple mixing equation was applied to determine the composition of a melt that had additions of 5, 10, and 15 wt. % plagioclase and olivine. Trends of compositions derived from variable plagioclase and olivine addition bracket observed Alicudi data well, specifically Al_2O_3 and MgO (Figure 29).

Based on the olivine addition models (Figure 29), 7-10% modal percent olivine in stages 1 and 2 cannot explain the most MgO-rich samples. However, if 5-15% olivine is added to MELTS Run 52's composition, high MgO values, similar to observed MgO values, can be achieved. In addition, most olivine crystals in Alicudi samples exhibit undulatory extinction, suggesting olivine was in disequilibrium with the melt. Olivine incorporated from wall rock or a crystal mush lining the magma chamber commonly exhibit undulatory extinction and reaction rims (Streck, 2008). Because olivine is not present in sufficient abundance in the samples, it is suggested that olivine was incorporated from a magma chamber mush, disaggregated and potentially reacted or

melted because it was in disequilibrium with the magma. This addition explains the higher MgO and Ni and also may have acted to dilute Al_2O_3 in basalts and basaltic andesites.

Based on plagioclase addition models (Figure 29), when 5-15% plagioclase is added to MELTS run 52's composition, the observed Al_2O_3 in Alicudi's whole rocks can be matched. In addition, plagioclase crystals present in all Alicudi samples exhibit complex textures, which may be attributed to RAFC processes (Streck, 2008). The addition of plagioclase explains higher Al_2O_3 and Sr found in stage 3. Alicudi samples do not exhibit Eu anomalies (Figure 9). However positive Eu anomalies are indicative of plagioclase accumulation. In contrast, lack of Eu anomalies can be due to high H_2O content, which yields high fO_2 (Gertisser and Keller, 2000). MELTS runs were most successful with an initial H_2O content of 3% and a fO_2 buffer of HM, which supports lack of Eu anomalies as a result of high fO_2. Also in support of high H_2O content is the fractionation of cryptic amphibole (Davidson et al., 2007). Positive correlations of La/Yb with SiO_2 is consistent with garnet and amphibole fractionation. However, most arc volcanoes, including Alicudi, exhibit trends of decreasing Dy/Yb with SiO_2; this is consistent with significant amphibole, but not garnet, fractionation (Figure 31).

Additional evidence also suggests that some of the olivine and plagioclase reacted or melted. Fe and Mg concentrations in plagioclase from samples ALI10-07, 08, 09, and
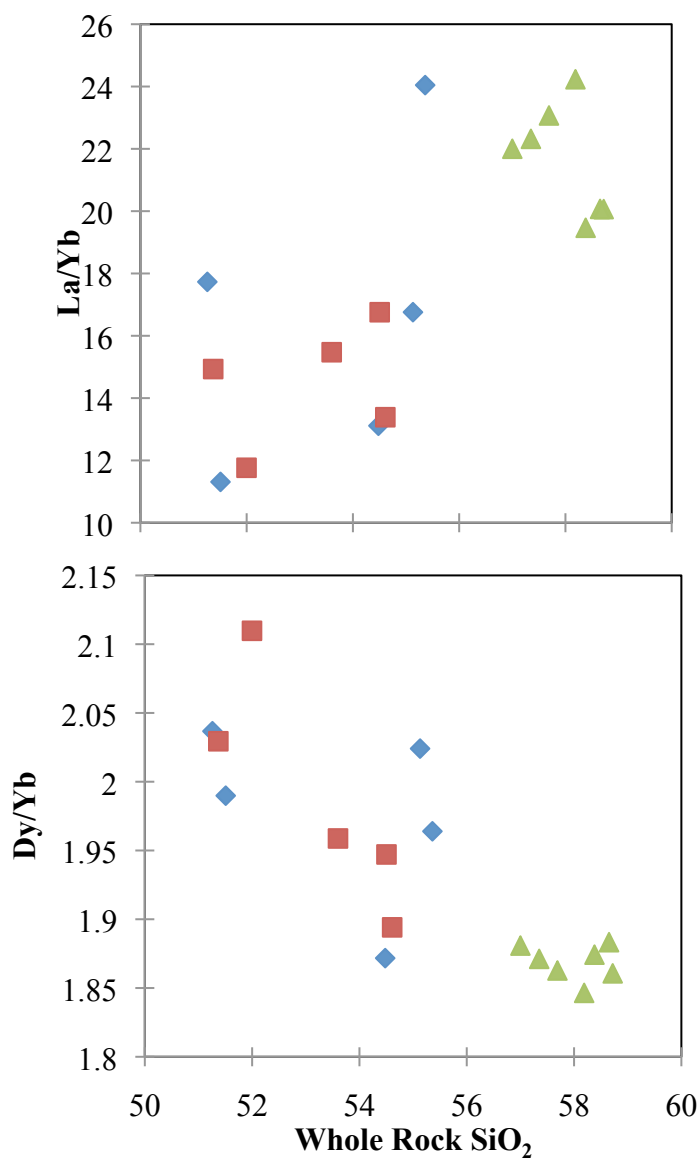
Figure 31. Whole rock SiO_2 plotted against (a) La/Yb and (b) Dy/Yb. Stage 1 is represented by blue diamond's; stage 2 by red squares; stage 3 by green triangles. Positive correlations of La/Yb with SiO_2 is consistent with garnet and amphibole fractionation, whereas negative correlations of Dy/Yb with SiO_2 is consistent with amphibole, not garnet, fractionation.

05 (stages 1 and 2) are noticeably higher and decrease with increasing An (Figure 21).

Also, Sr concentrations in plagioclase are highest in stage 3 (Figure 22). Fe partitioning

in plagioclase is strongly dependent on fO_2, as temperature increases and P_{H2O} decrease, Fe in plagioclase increases. Increases of Fe content in crystals, rims of crystals, and high Fe in microlites can be explained by cooling related to eruption and possibly an increase in fO_2 (Figure 18d) (Ginibre et al., 2002). However, Mg and Sr concentrations in plagioclase crystals reflect MgO and Sr whole rock data, suggesting plagioclase preserves olivine and plagioclase accumulation and disaggregation, evidence of signatures seen in whole rock. In contrast, Mg differentiation into plagioclase can be affected by temperature, however more work is needed to investigate temperature effects.

Based on the whole rock and plagioclase compositional observations, assimilation of a dominantly olivine+plagioclase rock explains some of the anomalous major and trace element data. Cr also has higher concentrations in stages 1 and 2 compared to mafic rocks from the other two islands, possibly suggesting accumulation and reaction/melting of small amounts of clinopyroxene. Thus, the most likely assimilant was gabbro, which would yield a source of olivine+plagioclase±clinopyroxene. Gabbroic xenoliths with olivine, plagioclase, and clinopyroxene are commonly found within samples on Alicudi (Peccerillo and Wu, 1992; Bonelli et al., 2004).

Andesites typically have the lowest radiogenic Sr isotope values, as seen in whole rock and plagioclase data (Figure 26). If assimilation is the explanation for the lower Sr isotope signatures in the andesite, then it is possible that the assimilant had less radiogenic $^{87}Sr/^{86}Sr$ than the mantle melts (Wolff et al., 2005). An assimilant, such as a

gabbro, will allow the most assimilated magma to have the lowest radiogenic Sr isotope value.

Recharge

Recharge of more mafic magma into a host chamber is suggested by plagioclase textural, major and trace element data. Reverse zoning is apparent in some plagioclase crystals, in which An in rims is higher than An in cores (Figure 24). Complex plagioclase textures are seen in rocks from all stages including dissolution rims and sieve/patchy textures. Textural boundaries can be accompanied by increases in An content $\geq$10% rimward (scale of 5-10 microns between microprobe spot analyses). Changes in textures and increases in An content $\geq$10% are consistent with recharge events from a more mafic melt (Ginibre et al., 2002), and are seen in all stages (Figure 25).

Finally, *in situ* Sr isotope signatures of most crystals in each sample are less radiogenic than groundmass and whole rock $^{87}Sr/^{86}Sr$, which are in equilibrium with each other within uncertainty (Figure 10). Plagioclase crystal Sr isotope heterogeneity (outside of analytical uncertainty) preserves a record of melts with variable $^{87}Sr/^{86}Sr$ that is similar to or less radiogenic than most whole rock values. These crystals may therefore record evidence of recharge. Recharge often leads to mixing (Streck, 2008), which allow plagioclase to preserve heterogeneous $^{87}Sr/^{86}Sr$ signatures amongst crystal populations and within crystals (Figure 26 and 27).

Alternative hypotheses may explain whole rock and crystal heterogeneity in Sr isotopes. Basalt plagioclase crystals and whole rocks mostly have the highest Sr

isotopes, whereas andesite plagioclase crystals and whole rocks have the lowest. This variation is atypical because typical assimilation trends show increasing $^{87}Sr/^{86}Sr$ with increasing SiO_2 wt.% (Davidson et al., 1987; Ramos et al., 2004; Wolff et al., 2005). In the case of Alicudi, there are several processes that can contribute to this trend. (1) Peccerillo and Wu (1992) propose that hotter mafic liquids are better able to incorporate crustal wall rock, changing isotopic signatures, whereas cooler andesites are not as greatly affected due to their inability to incorporate as much wall rock. However, while basalts are typically hotter than andesites, a significant proportion of the enthalpy of melting comes from latent heat of crystallization (Spera and Bohrson, 2005). This would suggest that although andesites typically have lower liquidus and sub-liquidus temperatures, they have generally experienced more crystallization than more mafic rocks, suggesting that they should experience the most assimilation and therefore have higher $^{87}Sr/^{86}Sr$ signatures than the more mafic rocks. (2) Although Stages 1 and 2 have higher Sr isotope signatures than stage 3, Sr concentrations are highest in stage 3. Thus, for equal masses of the same assimilant, stage 3 andesites $^{87}Sr/^{86}Sr$ would not change as much as those of the more mafic rocks. Quantitative modeling using EC-RAFC (Spera and Bohrson, 2004) and the Magma Chamber Simulator (Bohrson, pers. communication) is required to test the RAFC hypotheses.

Mixing, Assimilation, Storage, and Homogenization in Alicudi's Plumbing System

A critical observation about the whole rock and plagioclase compositional data for the Alicudi rocks is that the degree of variance decreases from basalt/basaltic andesite to andesite. These characteristics are particularly evident in trends of whole-rock trace elements and Sr isotopes and plagioclase major elements and isotopes. As noted above, mantle source heterogeneity and RAFC processes played important roles in the evolution of the magmatic system. These features are consistent with the existence of a MASH zone beneath Alicudi. MASH (mixing, assimilation, storage, and homogenization) zones are generated when basaltic magmas ascend from the mantle and establish neutral buoyancy; cause wall rock melting, assimilate and mix extensively; and either crystallize fully or partially undergo fractionation that reestablishes buoyant ascent. As the magma system evolves, the chemical signatures are predicted to homogenize (Hildreth and Moorebath, 1988).

Mixing

Mixing is supported by whole rock trace element and Sr and Nd isotope data and *in situ* plagioclase data. Whole rock trace elements are more variable in stages 1 and 2 than in stage 3 and samples from Filicudi and Alicudi with the same range of SiO_2 (wt.%) (Figure 6, 7, and 8). In addition, $^{87}Sr/^{86}Sr$ is more variable in stages 1 and 2 (Figure 10), and all stages have less radiogenic Sr and more radiogenic Nd than Filicudi and Salina (Figure 11 and 28). Plagioclase crystals also exhibit heterogeneous $^{87}Sr/^{86}Sr$ signatures. Variability of trace elements and isotopes are preserved in plagioclase, as

evidence of recharge. Additionally, populations of reversely zoned plagioclase and increases in An of >10% over textural boundaries (5-10 microns) are present in all stages. Collectively, these data suggest stages 1 and 2 were supplied and recharged by melts from a heterogeneous mantle source.

Assimilation

Assimilation is supported by whole rock major and trace element and *in situ* plagioclase textural, major and trace element, and isotope data. MgO and Ni are higher in mafic samples, whereas Al_2O_3 and Sr are higher in andesites, suggesting accumulation of olivine and plagioclase, respectively. Plagioclase Mg and Sr data reflect whole rock MgO and Sr data, which is consistent with olivine and plagioclase reaction or melting. All stages have complex textures in plagioclase, such as oscillatory, patchy, sieve, and dissolution surfaces. Coupling textural data with major, trace, and isotope data has helped identify assimilation and fractional crystallization (Humphreys et al, 2006; Salisbury et al., 2008; Streck, 2008). For example, plagioclase profiles for An content, Sr, Ba, Fe, Mg, and Ti (ppm) plotted against distance from core show significant changes, some of which are associated with texture boundary changes (Figure 25 and Electronic Appendix A, Reduced microprobe data). In addition to whole rock major and trace element data, and plagioclase textural and major and trace element data, simple addition of variable amounts of plagioclase and olivine wt. % to compositions of MELTS results bracketed observed Alicudi data. Lastly, the presence of xenoliths containing plagioclase, olivine, and clinopyroxene suggests a possible gabbroic assimilant (Figure 29).

Homogenization

Decrease in variance from stages 1 to 3 with respect to whole rock trace element and isotope trends and *in situ* plagioclase textural data and major and trace element trends supports homogenization. Ba, Th, Nb, U, and La in stages 1 and 2 have larger variations than stage 3 (Figure 7 and 8). Also, REEs are more variable in mafic samples than in andesitic samples (Figure 9). Lastly, radiogenic Sr isotopes are more variable in basalts and basaltic andesites than in the andesites (Figure 10).

Stage 1 and 2 plagioclase has a wide range in An. Stage 3 plagioclase crystals also have a wide range in An, but are generally less variable than previous stages (Figure 10). Additionally, plagioclase trace elements Fe, Mg, and Ti are more variable in stages 1 and 2 (Figure 21). Furthermore, Sr isotopes in plagioclase are more variable in stage 1, and least variable in stage 3 (Figure 26). This decrease in variance is consistent with aggregation of smaller magma bodies (e.g., plexus of dikes and sills), which allowed compositional heterogeneity to be recorded in mafic rocks. A larger magma body that is better homogenized is predicted for stage 3.

Storage

Shoaling (storage) of magma chamber(s) at Alicudi is supported by successful MELTS simulations. MELTS models successfully match Alicudi's whole rock data trends when run in the polybaric mode. Best-fit models have initial pressures of 2 kbar and final pressures of 10 bar, suggesting multiple magma reservoir depths. Stage 3 andesites possibly formed in a coalesced plexus that resides at a shallower level compared to the plexus of stages 1 and 2 that resided at deeper levels. As a result, stage

3 has lower variability in whole rock trace and isotope trends, and *in situ* plagioclase trends.

Evolution of Alicudi's Magmas

Whole rock major and trace element and Sr and Nd isotope data and *in situ* plagioclase data strongly support a MASH scenario (cf. Hildreth and Moorebath, 1987). First, isotopically heterogeneous basaltic magmas ascend from deeper levels until neutrally buoyant. Whole rock and plagioclase crystals associated with this stage are characterized by heterogeneous Sr isotopes and varying An content, documenting a plexus of dikes and sills in middle to upper crust. Next, continued recharge and assimilation potentially promote aggregation of smaller magma bodies, as evidenced by lower variance in compositional parameters from stage 1 to 3. Lastly, stage 3 andesites possibly formed in a coalesced plexus that resides at a shallower level compared to the plexus of stages 1 and 2, as suggested by polybaric MELTS simulations (Figure 32).
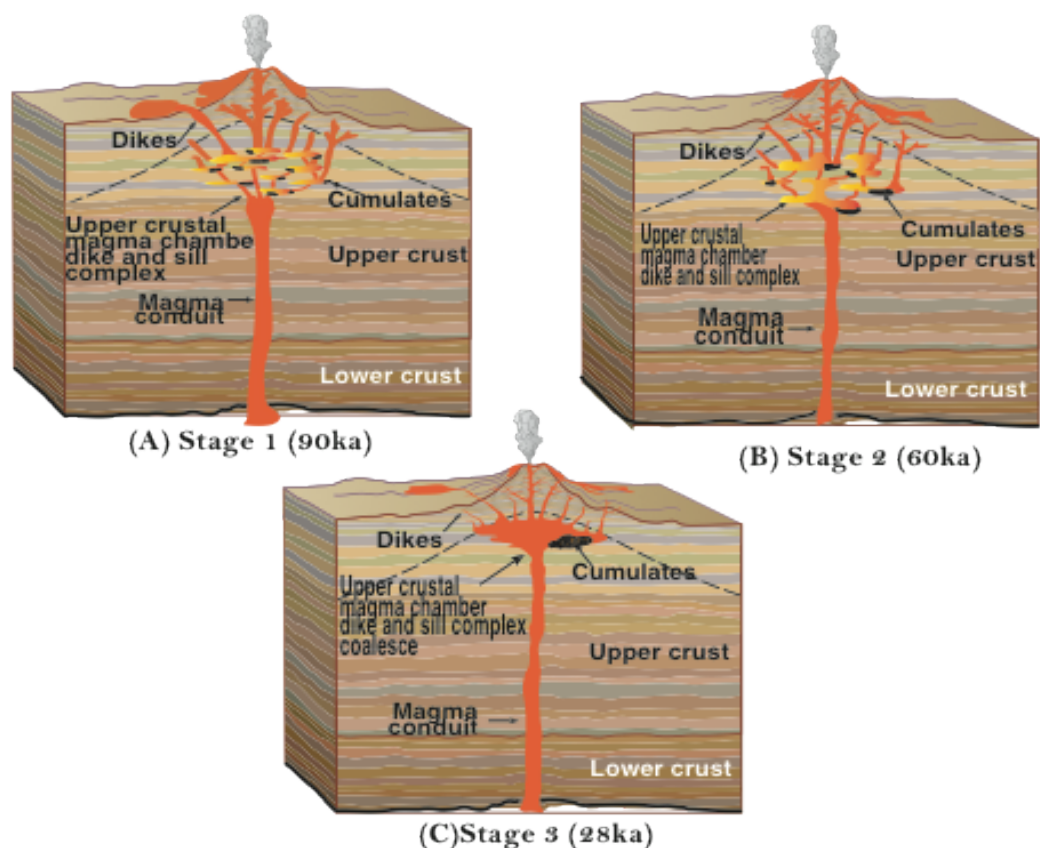
Figure 32. Schematic MASH model for stages 1, 2, and 3. (A) Isotopically heterogeneous basaltic magmas ascend from deeper levels until neutrally buoyant. Plagioclase associated with this stage is characterized by heterogeneous Sr isotopes and varying An content, documenting a plexus of dikes and sills in upper crust. (B) Continued recharge and assimilation potentially promote aggregation of plexus, as evidenced by lower variance in compositional parameters in stage 2. (C) Stage 3 andesites possibly formed in a coalesced plexus that resides at a shallower level compared to the plexus of stages 1 and 2, as suggested by polybaric MELTS simulations. (Magma chamber diagrams modified from Spera and Bohrson, 2004).

CHAPTER VI

CONCLUSIONS

In this study, I present whole rock major and trace element and Sr and Nd

isotope data, *in situ* plagioclase textural, major and trace element, and Sr isotope data,

and MELTS models to document the processes that lead to compositional diversity at

Alicudi. This compilation of data suggests mixing of heterogeneous mantle sources,

assimilation, storage, and homogenization characterize Alicudi's magmatic evolution.

Variations seen in whole rock trace element and Sr and Nd isotope data suggest

mantle source heterogeneity. Stages 1 and 2 exhibit larger ranges of trace elements Ba,

Th, Nb, U, and La than stage 3. Additionally, over a 50-55 range of SiO_2 (wt.%), trace

elements in Alicudi's samples are more variable than those found in Filicudi's and

Salina's samples. Lastly, Alicudi exhibits lower $^{87}Sr/^{86}Sr$ and higher $^{143}Nd/^{144}Nd$ than

Filicudi and Salina.

Alicudi's *in situ* plagioclase textural, major and trace element data support

mixing. Complex plagioclase textures are seen in all stages. Sharp changes in

plagioclase major and trace elements are noted rimward of textural transition of 5-10

microns. Specifically noteworthy are increases in An of ≥ 10 mole % rimward of

dissolution rims or other textural transitions, which are common in cases of recharge.

Additionally, heterogeneous $^{87}Sr/^{86}Sr$ is preserved within plagioclase crystals, and

amongst plagioclase crystal populations.

Assimilation is supported by whole rock major element data and *in situ*

plagioclase major and trace element data. Whole rock major element data are

characterized by mostly systematic trends; however, MgO, Al_2O_3, Ni, Sr and Cr are exceptions. MgO, Ni, and Cr are highest in stages 1 and 2, whereas Al_2O_3 and Sr are highest in stage 3. Assimilation of a gabbroic component can explain variable trends in whole rock data. The addition of variable amounts of plagioclase and olivine to the composition of MELTS Run 52 supports accumulation of plagioclase and olivine (common minerals found in gabbros). In addition, plagioclase trace elements, Fe and Mg are highest in stages 1 and 2, whereas Sr in plagioclase is highest in stage 3. Plagioclase trace element trends mimic whole rock major trends; suggesting olivine and plagioclase reacted or melted, and thus higher Mg and Sr signatures are recorded in the whole rock and preserved in plagioclase crystals. Lastly, *in situ* plagioclase major element data show decreases rimward of dissolution rims or textural changes in An of ≥10 mole %, suggesting assimilation and fractional crystallization processes.

Decrease in variation of whole rock trace element and isotope data and *in situ* plagioclase major and trace element and isotope data support homogenization. Whole rock trace elements Ni, Cr, Ba, Zr, Th, U, and La are more variable in stages 1 and 2. Sr isotopes are also more variable in stage 1. Additionally, An content from plagioclase in stages 1 and 2 exhibit large variations. Stage 3 also has large variations in An content, but is typically less variable than stage 1 and 2. Trace elements and Sr isotopes in plagioclase exhibit similar variability. A complex plexus of dikes and sills is used to describe the degree of variability in stages 1 and 2.

Successful MELTS polybaric simulations support storage, and possibly shoaling of magma reservoirs. MELTS models successfully match observed Alicudi data when

run in polybaric mode, suggesting multiple magma reservoir depths. Because andesites exhibit mostly systematic whole rock major and trace and isotope trends, and *in situ* plagioclase major and trace element and isotope trends, it is suggested that stage 3 formed in a coalesced magma reservoir, possibly at a shallower level than the plexus that formed stages 1 and 2.

Strong evidence of mantle source heterogeneity, magma mixing and crustal assimilation, and homogenization suggest a MASH scenario (cf. Hildreth and Moorebath, 1987). From whole rock trace element and isotope data, it is suggested that isotopically heterogeneous basaltic magmas ascend from deeper levels until neutrally buoyant. Additionally, heterogeneous Sr and varying An content in plagioclase crystals are associated with this stage and document a plexus of dikes and sills in the middle to upper crust. Variations in mafic whole rock MgO, Al_2O_3, Ni, Sr, and incompatible trace elements, and plagioclase An, Mg, and Sr support recharge and assimilation, which potentially promote aggregation of smaller magma bodies. Also, evidenced by lower variance in compositional parameters in stage 2, aggregation of plexus from stages 1 and 2 is suggested. Lastly, stage 3 andesites possibly formed in a coalesced plexus that resides at a shallower level compared to the plexus of stages 1 and 2, as suggested by polybaric MELTS simulations.

Future Work

The data provided in this study suggest possibilities for future work on Alicudi. Although assimilation and recharge have been recognized as processes that have occurred on Alicudi, parameters such as the compositions and masses of recharge and assimilated melts have not been documented. Thus, more extensive MELTS modeling and the addition of EC-RAFC models (Ghiorso and Sack, 1995; Bohrson and Spera, 2001) would better define the processes that have occurred, as well as examine mass and thermal constrants.

It is recognized that mass balance requires more radiogenic Sr or a higher $^{87}Sr/^{86}Sr$ component in order for the groundmass to be in equilibrium with the whole rock. Radiogenic Sr values found in plagioclase are typically lower than whole rock and groundmass values. However, limitations of crystal size prevented an accurate analysis of radiogenic Sr in all plagioclase. By identifying larger plagioclase crystals, analyzing Sr isotopes in cores and rims of plagioclase is possible. Additionally, microdrilling and analyzing plagioclase smaller than the crystals analyzed by LA-MC-ICPMS will allow an investigation of the mass balance between the whole rock, groundmass, and plagioclase. Assimilation can be attributed to heterogeneous Sr isotope signatures within plagioclase at the time of crystallization.

In addition to *in situ* plagioclase analysis, *in situ* textural, major and trace, and Sr isotope data could be collected on olivine and clinopyroxene to further elucidate magma chamber conditions at the time of crystal formation for these minerals.

Additionally, the study of melt inclusions found in plagioclase, olivine, and clinopyroxene might identify varying degrees of contamination, compositions of assimilants, and magma chamber depths.

Lastly, looking at geochemical and petrological data from samples below sea level may further the understanding of magma chamber processes at Alicudi. Studies on Alicudi, including this one, are restricted to eruptions that are present above sea level; this only represents the summit of Alicudi and a short period of activity (28-167 ka). Alicudi volcano extends 2000 m below sea level. Additional geochemical or petrologic data from the beginning of Alicudi's activity (i.e. data on volcanic products from Alicudi below sea level) would allow a more comprehensive assessment of the factors that have contributed to compositional diversity at Alicudi.

REFERENCES CITED

Bohrson, W., and Reid, M., 1995, Petrogenesis of alkaline basalts from Socorro Island, Mexico: Trace element evidence for contamination of ocean island basalt in the shallow ocean crust: Journal of geophysical research, v. 100, p. 24,555-24,576.

Bohrson, W., and Reid, M., 1997, Genesis of silicic peralkaline volcanic rocks in an ocean island setting by crustal melting and open-system processes: Socorro Island, Mexico: Journal of Petrology, v. 38, p. 1137-1166.

Bohrson, W., and Spera, A., 2001, Energy-Constrained Open-System Magmatic Processes II: Application of Energy-Constrained Assimilation–Fractional Crystallization (EC-AFC) Model to Magmatic Systems: Journal of Petrology, v. 42 p. 1019-1041.

Bohrson, W., 2012, personal communication.

Bonelli, R., Frezzotti, M., Zanon, V., and Peccerillo, A., 2004, Evolution of the volcanic plumbing system of Alicudi (Aeolian Islands- Italy): evidence from fluid and melt inclusions in quartz xenoliths: Annals of Geophysics, v.47, p. 1409-1422.

Bowen, N., 1928, The Evolution of Igneous Rocks, Princeton, NJ: Princeton University Press, 334 p.

Boynton, W., 1984, Cosmochecmistry of the rare earth elements: meteorite studies: Rare Earth Element Geochemistry: New York, Elsevier, p.63-114.

Calanchi, N., Peccerillo, A., Tranne, C., Lucchini, F., Rossi, P., Kempton, P., Barbieri, M., and Wu, T., 2002, Petrology and geochemistry of volcanic rocks from the island of Panarea: implications for mantle evolution beneath the Aeolian island ac (southern Tyrrhenian sea): Journal of Volcanology and Geothermal Research, v. 115, p. 367-395.

Cortini, M., 1981, Aeolian Island Arc (South Tyrrhenian Sea) magma heterogeneities in historical lavas: Sr and Rb isotopic evidence: Bulletin Volcanologique, v. 44, p. 711-722.

Clynne, M., 1999, A complex magma mixing origin for rocks erupted in 1915, Lassen Peak, California: Journal of Petrology, v. 40, p. 105-132.

Creamer, J., personal communication.

Davidson, J., Dungan, M., Ferguson, K., Colucci, M., 1978, Crust-magma interactions and the evolution of arc magmas: The San Pedro-Pellado volcanic complex, southern Chilean Andes: Geology, v. 15, p. 443-446.

Davidson, J., Hora, J., Garrison, J., and Dungan, M., 2005, Crustal Forensics in arc magmas: Journal of Volcanology and Geothermal Research, v. 140, p. 157-170.

Davidson, J., Morgan, D., and Charlier, B., 2007, Isotopic Microsampling of magmatic rocks: Elements, v. 3, p. 253-259.

Davidson, J., Simon, T., Handley, H, Macpherson, C., and Dosseto, A., 2007, Amphibole "sponge" in arc crust?: Geology, v. 35, p. 787-790.

De Rosa, R., Guillou, H., Mazzuoli, R., and Ventura, G., 2001, New unspiked K-Ar ages of volcanic rocks of the central and western sector of the Aeolian Islands: reconstruction of the volcanic stages: Journal of Volcanology and Geothermal Research, v. 120, p. 161-178.

Eichelberger, J., 1975, Origin of andesite and dacite: Evidence of mixing at Glass Mountain in California and at other circum-Pacific volcanoes: Geology Society of American Bulletin, v. 86, p. 1381-1391.

Einstein, N, 2005, File:Aeolian Islands map.png: http://en.wikipedia.org/wiki/File:Aeolian_Islands_map.png (accessed January, 2012).

Ellam, R., and Harmon, R., 1990, Oxygen isotope constraints on the crustal contribution to the subduction-related magmatism of the Aeolian Islands, southern Italy: Journal of Volcanology and Geothermal Research, v. 44, p. 105-122.

Ellam, R., Menzies, M., Hawkesworth, C., Leeman, W., Rosi, M., and Serri, G., 1988, The transition from calc-alkaline to potassic orogenic in the Aeolian Islands, Southern Italy: Bulletin of Volcanology, v. 50, p. 386-398.

Falsaperia, S., Lanzafame, G., Longo, V., and Spamoinato, S., 1999, Regional stress field in the area of Stromboli (Italy): insights into structural data and crustal tectonic earthquakes: Journal of Volcanology and Geothermal Research, v. 88, p.147-166.

Fowler, S., Bohrson, W., and Spera, F., 2004, Magmatic Evolution of the Skye Igneous Centre, Western Scotland: Modeling of Assimilation, Recharge and Fractional Crystallization: Journal of Petrology, v. 45, p. 2481-2505.

Fowler, S., Spera, F., Bohrson, W., Belkin, H., and De Vivo, B., 2007, Phase Equilibria Constraints on the chimical and physical evolution of the Campanian Ignimbrite: Journal of Petrology, v. 48, p. 459-493.

Francalanci, L. and Manetti, P., 1994, Geodynamic models of the Southern Tyrrhenian Region: constraints from the petrology and geochemistry of the Aeolian volcanic rocks: Bullettino di Geofisica Tearica ed Applicata, v. 36, p. 283-292.

Furman, T., Frey, F., and Meyer, P., 1992, Petrogenesis of evolved basalts and rhyolites at Austurhorn, southeastern Iceland; the role of fractional crystallization: Journal of Petrology, v. 33, p. 1405-1445.

Gertisser, R. and Keller, J., 2000, From basalt to dacite: origin and evolution of the calc-alkaline series of Salina, Aeolian Arc, Italy: Contributions to Mineralogy Petrology, v. 139, p. 607-626.

Ghiorso, M., and Sack, R., 1995, Chemical mass transfer in magmatic processes IV. A revised and internally consistent thermodynamic model for the interpolation and extrapolation of liquid-solid equilibria in magmatic systems at elevated temperatures and pressures: Contributions to Mineralology and Petrology, v. 119, p. 197-212.

Ginibre, C., Worner, G., and Kronz, A., 2002, Minor- and trace-element zoning in plagioclase: implications for magma chamber processes at Parinacota volcano, northern Chile: Contributions to Mineralogy and Petrology, v. 143, p. 300-315.

Ginibre, C., Worner, G., and Kronz, A., 2007, Crystal zoning as an archive for magma evolution: Elements, v. 3, p. 261-266.

Govindaraju, K., 1994, 1994 compilation of working values and sample description for 383 geostandards: Geostandards Newsletter, v. 18, p. 158.

Harris, M., 2012, personal communication.

Hessel, P., 2007, Magma Dynamics of the phonolitic Diego Hernandez Formation, Tenerife, Canary Islands [PhD Thesis]: Washington State University.

Humphreys, M., Blundy, J., Stephen, R., and Sparks, J., 2006, Magma evolution and open-system processes at Shiveluch Volcano: Insights from phenocryst zoning: Journal of Petrology, v. 47, p. 2303-2334.

Jenner, G., Longerich, H., Jackson, S., and Fryer, B., 1990, ICP-MS – a powerful tool for high-precision trace-element analysis in Earth science: Evidence from analysis of selected USGS reference samples: Chemical Geology, v. 68, p. 133-148.

Francalanci, L., Avanzinelli, R., Tommasini, S., and Heuman, A., 2007, A west-east geochemical   and isotopic traverse along the volcanism of the Aeolian Island arc, southern Tyrrhenian Sea, Italy: Inferences on mantle source processes: The Geological Society of America, special paper 418, p. 235-263.

Francalanci, L., Taylor, S., McCullock, M.T., and Woodhead, J.D., 1993, Geochemical and isotopic variations in the calc-alkaline rocks of Aeolian arc, Tyrrhenian Sea, Italy: constraints on magma genesis: Contributions to Mineralogy and Petrology, v. 113, p. 300-313.

Hildreth, W. and Moorebath, S., 1988, Crustal contributions to arc magmatism in the Andes of Central Chile: Contributions to Mineralogy and Petrology, v. 98, p. 455-489.

Humphreys, M., Blundy, J., and Sparks, S., 2006, Magma evolution and open-system processes at Shiveluch Volcano: Insights from phenocryst zoning: Journal of Petrology, v. 47, p. 2303-2334.

Johnson, D., Hooper, P., and Conrey, R., 1999, XRF analysis of rocks and minerals for major and trace elements on a single low dilution Li-tetraborate fused bead: Advances in X-ray Analysis, v. 41, p. 843-867.

Kremser, D., 2006, Advanced Topics in probe for windows: Probe for Windows NT/2000/XP (32 bit), v. 6.41, p. 1-168.

Lucchi, F., Tranne, C., and Rossi, P., 2008, New chronostratigraphic constraints for the eruptive history of Alicudi volcano (Aeolian archipelago, Italy): Geo Acta, v. 7, p. 115-131.

Mayfield, M., 2012, personal communication.

Nazzareni, S., Molin, G., Peccerillo, A., and Zanazzi, P., 2001, Volcanological implications of crystal-chemical variations in clinopyroxene from the Aeolian Arc, Southern Tyrrhenian Sea (Italy): Bulletin of Volcanology, v. March, p. 738-82.

Pallister, J., Hoblitt R., Meeker G., Knight R., and Siems D., 1996, Magma mixing at Pinatubo: Petrographic and chemical evidence for the 1991 deposits. In: Fire and mud: eruptions and lahars of Mount Pinatubo, Philippine. Newhall CG, Punongbayan RS (eds) PHIVOLCS, Quezon City, Philippines and University of Washington Press, p 687-731.

Peccerillo, A., Dallai, L., Frezzotti, M., and Kempton P., 2004, Sr-Nd-Pb-O isotopic evidence for decreasing crustal contamination with ongoing magma evolution at

Alicudi volcano (Aeolian arc, Italy): implications for style of magma-crust interaction and from mantle source compositions: Lithos, v. 78,, p. 217-233.

Peccerillo, A., Wu, T.W., 1992, Evolution of calc-alkaline magmas in continental arc volcanoes: evidence from Alicudi, Aeolian arc (Southern Tyrrhenian Sea Italy): Journal of Petrology, v. 33, p. 1295-1315.

Ramos, F.C., Reid, M.R., 2005, Distinguishing melting of heterogeneous mantle sources from crustal contamination: insights from Sr isotopes at the phenocryst scale, Pisgah Crater, California: Journal of Petrology, v. 46, p. 999-1012.

Ramos, F.C., Wolff, J.A., Tollstrup, D.L., 2004, Measuring ^{87}Sr/^{86}Sr variations in minerals and groundmass from basalts using LA-MC-ISPMS: Chemical Geology, v. 211, p. 135-158.

Salisbury M., Bohrson, W., Clynne, M., Ramos, F., Hoskin, P., 2008, Origin of the 1915 Lassen Peak eruption by magma mixing: Evidence for formation of chemically distinct plagioclase populations from crystal size distribution and in situ chemical data: Journal Of Petrology, v.49, p.1755-1778.

Spadini, G. and Padladchikov, Y., 1996, Spacing of consecutive normal faulting in the lithosphere: a dynamic model for rift axis jumping (Tyrrhenian Sea): Earth and Planetary Science Letters, v. 144, p. 21-34.

Spera, F., and Bohrson, W., 2004, Open-system magma chamber evolution: and energy-constrained geochemical model incorporating the effects of concurrent eruption, recharge, variable assimilation and fractional crystallization (EC-ERAFC): Journal of Petrology, v. 45, p. 2459-2480.

Streck, M., 2008, Mineral Textures and zoning as evidence for open system processes: Reviews in Mineralogy and Geochemistry, v. 69, p. 595-622.

Streck, M., Dung, M., Bussy, F., and Malavassi, E., 2005, Mineral inventory of continuously erupting basaltic andesites at Arenal volcano, Costa Rica: implications for interpreting monotonous, crystal-rich, mafic arc stratigraphies: Journal of   Volcanology and Geothermal Research, v. 140, p. 133-155.

Tepley, F., Davidson, J., and Clynne, M., 1999, Magmatic interactions as recorded in plagioclase phenocyrsts of Chaos Crags, Lassen Volcanic Center, California: Journal of Petrology, v. 40, p. 787-806.

Viccaro, M., Giacomoni, P., Ferlito, C., and Cristofolini, R., 2010, Dynamics of magma supply at Mt. Etna volcano (Southern Italy as revealed by textural and compositional features of plagioclase phenocrysts: Lithos (in press).

Wolff, J., Rowe, M., Teasdale, R., Gardner, J., Ramos, F., and Heikoop, C., 2005, Petrogenesis of Pre-caldera Mafic Lavas, Jemez Mountains Volcanic Field (New Mexico, USA): Journal of Petrology, v. 46, p. 407-439.